iScience

CellPress

Article

Hierarchical Uniform Supramolecular Conjugated Spherulites with Suppression of Defect Emission

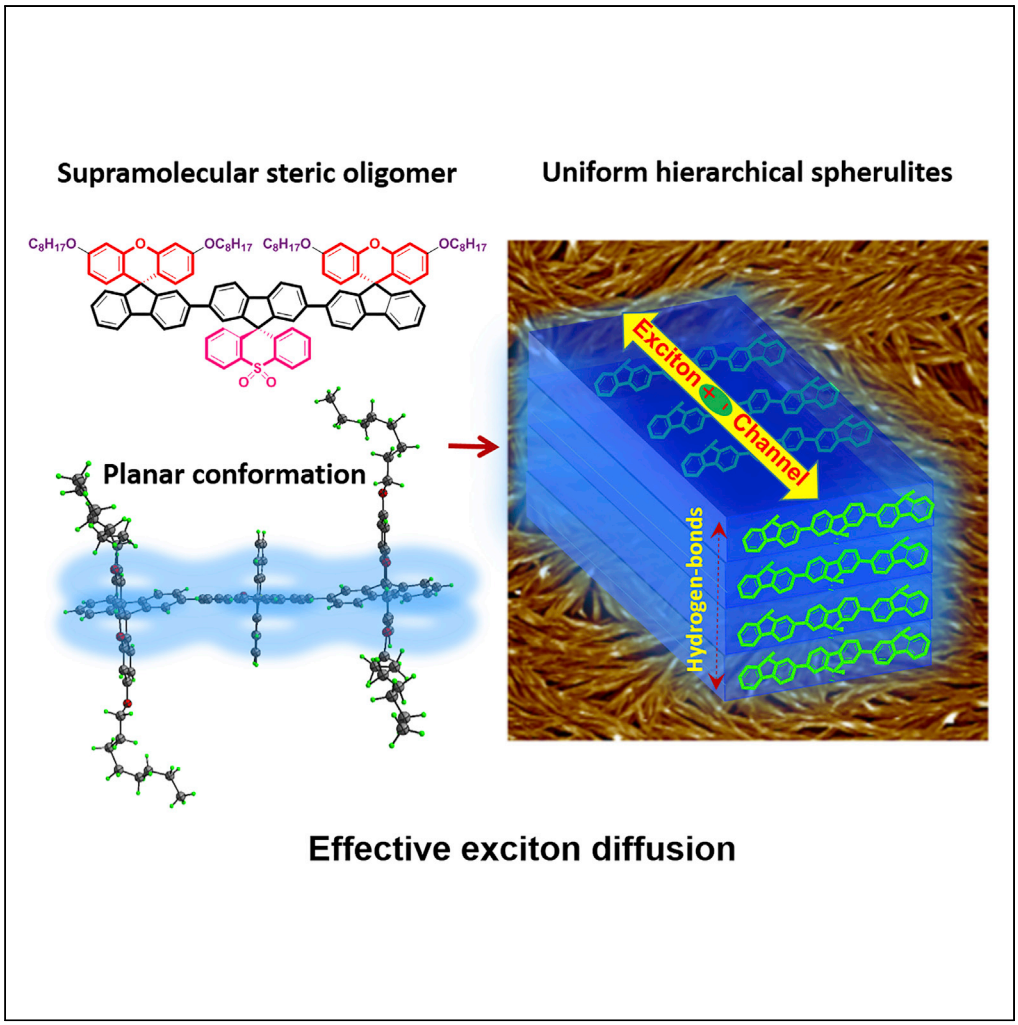

Changjin Ou, Nathan J. Cheetham, Jiena Weng, ..., Yamin Han, Donal D.C. Bradley, Wei Huang

iamjylin@njtech.edu.cn (J.L.)
iamlhxie@njupt.edu.cn (L.X.)
wei-huang@njtech.edu.cn (W.H.)

HIGHLIGHTS

Coplanar molecular conformation is stabilized in supramolecular crystalline frameworks

Spiro-terfluorene can self-assemble into hierarchical well-defined spherulites

Ordered and uniform condensed structures suppress defect emission

Ou et al., iScience *16*, 399–409
June 28, 2019
https://doi.org/10.1016/j.isci.2019.06.002

iScience

CellPress

Article

Hierarchical Uniform Supramolecular Conjugated Spherulites with Suppression of Defect Emission

Changjin Ou,[1,2] Nathan J. Cheetham,[3] Jiena Weng,[1,4] Mengna Yu,[2] Jinyi Lin,[1,4,6,*] Xuhua Wang,[3] Chen Sun,[5] Juan Cabanillas-Gonzalez,[5] Linghai Xie,[2,4,*] Lubing Bai,[1] Yamin Han,[1] Donal D.C. Bradley,[6] and Wei Huang[1,2,4,7,*]

SUMMARY

Easily processed, well-defined, and hierarchical uniform artificial architectures with intrinsic strong crystalline emission properties are necessary for a range of light-emitting optoelectronic devices. Herein, we designed and prepared ordered supramolecular spherulites, comprising planar conformational molecules as primary structures and multiple hydrogen bonds as physical cross-links. Compared with serious aggregation-induced fluorescence quenching (up to 70%), these highly ordered architectures exhibited unique and robust crystalline emission with a high PLQY of 55%, which was much higher than those of other terfluorenes. The primary reasons for the high PLQY are the uniform exciton energetic landscape created in the planar conformation and the highly ordered molecular packing in spherulite. Meanwhile, minimal residual defect (green-band) emissions are effectively suppressed in our oriented crystalline framework, whereas the strong and stable blue light radiations are promoted. These findings may confirm that supramolecular ordered artificial architectures may offer higher control and tunability for optoelectronic applications.

INTRODUCTION

Construction of ordered organic artificial architectures is fundamental to the exploration of novel material systems in the disruptive technology area, and some have shown promising applications as functional and active units in electronic, smart, and biosystems, owing to their unprecedented properties and intriguing functions (Hoeben et al., 2005; Liu et al., 2015; Sanchez et al., 2005; van de Burgt et al., 2017; Zhang et al., 2016). Natural systems provide numerous examples of precise and efficient self-assembly processes, such as DNA functions of replication and transcription in biological systems and polypeptide structures as highly ordered, multilevel, condensed, complex macromolecules capable of highly specific functionalities (Costa et al., 2013; Wang et al., 2016). Fundamentally, the dynamic and reversible nature of orthogonal hydrogen-bonding interactions is an intrinsic, original, and basic factor enabling these organized macromolecules to self-assemble into advanced supramolecular functional systems (Aida et al., 2012; Hoeben et al., 2005; Lehn, 2010; Sengupta and Würthner, 2013). Compared with the conventional superstructure with a range of common smart and mechanical properties, supramolecular conjugated solid states display a wide variety of complicated, photophysical mechanisms for electron delocalization, hybridization, and coupling (Heeger, 2010; Huang et al., 2019; Liu et al., 2017a, 2017b; Mikhnenko et al., 2015; Xie et al., 2012; Yang et al., 2018; Ye et al., 2018). Similar to the ordered, natural systems, the highly uniform and well-defined conjugated nanostructures that are receptive to processing can provide an effective and favorable electronic micro-environment that promotes exciton diffusion (Jin et al., 2018; Lin et al., 2010; Mikhnenko et al., 2015) and energy transport (Haedler et al., 2015; Kim et al., 2013; Vogelsang et al., 2011). An ideal environment for the photophysical processes without irregularities plays a key role to a range of functions for organic devices (Venkateshvaran et al., 2014; Yan et al., 2009).

In printed optoelectronics, the orderly condensed structure of a solution-processed π-conjugated semiconductor consistently optimized the fundamental photophysical processing of the active thin film, thereby enhancing the device performance (Eisele et al., 2014; Lunt et al., 2010; Mikhnenko et al., 2015; Peumans et al., 2003). For instance, ultralong exciton diffusion lengths (up to >200 nm) (Jin et al., 2018), energy transport lengths (>2 μm), and outstanding charge mobility (100 $cm^2 V^{-1} s^{-1}$) (Li et al., 2017; Yan et al., 2009) are obtained in well-defined supramolecular artificial architectures. To optimize this photophysical property, the chemical and physical defects should be avoided in solid states. Beyond chemical impurity and structural defects, intrinsic physical defects with an energetic disorder can constrain exciton combination or diffusion and block energy transfer or charge transport (Barford and Duffy, 2006; Noriega et al., 2013; Podzorov, 2013). Until now, uniform condensed structures are associated with tertiary structures, defined as

[1]School of Physical and Mathematical Sciences & Institute of Advanced Materials (IAM), Jiangsu National Synergetic Innovation Center for Advanced Materials (SICAM), Nanjing Tech University (NanjingTech), 30 South Puzhu Road, Nanjing 211816, China

[2]Center for Molecular Systems and Organic Devices (CMSOD), Key Laboratory for Organic Electronics and Information Displays & Institute of Advanced Materials (IAM), Jiangsu National Synergetic Innovation Center for Advanced Materials (SICAM), Nanjing University of Posts & Telecommunications, 9 Wenyuan Road, Nanjing 210023, China

[3]Department of Physics and Centre for Plastic Electronics, The Blackett Laboratory, Imperial College London, Prince Consort Road, London SW7 2AZ, UK

[4]Shaanxi Institute of Flexible Electronics (SIFE), Northwestern Polytechnical University (NPU), 127 West Youyi Road, Xi'an 710072, Shaanxi, China

[5]Madrid Institute for Advanced Studies (IMDEA Nanociencia), Ciudad Universitaria de Cantoblanco, Calle Faraday 9, Madrid 28049, Spain

[6]Departments of Engineering Science and Physics and Division of Mathematical, Physical and Life Sciences, University of Oxford, 9 Parks Road, Oxford OX1 3PD, UK

[7]Lead Contact

*Correspondence: iamjylin@njtech.edu.cn (J.L.), iamlhxie@njupt.edu.cn (L.X.), wei-huang@njtech.edu.cn (W.H.)

https://doi.org/10.1016/j.isci.2019.06.002

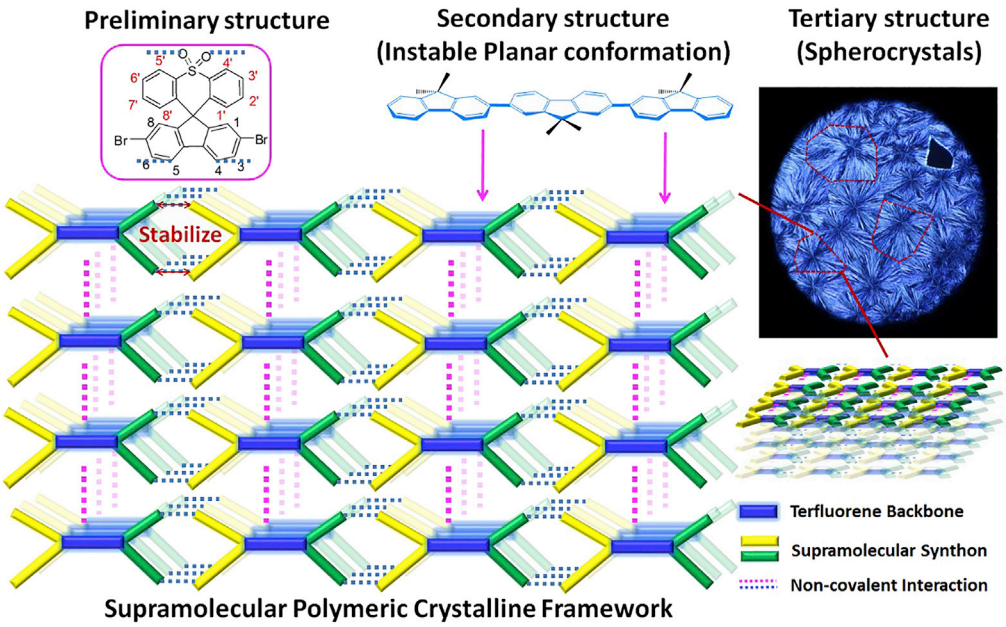

Scheme 1. Schematic Illustration of Hierarchical Highly Ordered Condensed Structures of Synthetic Organic Semiconductors: Steric Molecular Structures, Oriented Planar Conformation, and Uniform Supramolecular Spherulites

regular and periodic molecular packing and arrangement of conjugated molecules. Compared with stable amorphous states, the ordered, uniform superstructures with simultaneously oriented conformations at molecular levels are energetically unstable states. These can only be stabilized in noncovalent interactions, assisted by hierarchical architectures (Haedler et al., 2015; Liu et al., 2017a, 2017b). The rigid π-conjugated backbone structure with its highly molecular orientation and order presents the following challenges: first, it possesses complicated and variable conformations and high-energy features and second, it is polymorphous in solid state and characterized by several competitive weak intra- and intermolecular interactions (Kim et al., 2013). In addition, molecular conformation can be precisely controlled by noncovalent interactions to stabilize the intrinsic steric energy generated by the formation of ordered and oriented conformations and phases in higher-level superstructures (Kim et al., 2013; Liu et al., 2017a, 2017b). In fact, dynamic noncovalent bonds can easily maintain and release energy, providing the important feature of allowing energy dissipation under strain, and subsequently recovering to achieve high stretchability and auto-recovery properties (Chen et al., 2012; Oh et al., 2016; Wu et al., 2008; Yang and Urban, 2013). With this in mind, to simulate the natural, multilevel superstructure induced by the noncovalent interaction (Hoeben et al., 2005; Sengupta and Würthner, 2013), the incorporation of dynamic crosslinking noncovalent bonds into supramolecular architectures is an effective and simple method to obtain both oriented and ordered conformation, and higher-level condensed states (Scheme 1).

In this study, we established a molecular design principle of supramolecular conjugated macromolecules with orthogonal hydrogen-bonding interactions to enable a secondary planar conformation toward controlling and improving photonic behavior, defined as supramolecular plastic photonics (SPPs: photonic behavior of polymeric system can be significantly improved by supramolecular approach). This oriented planar conformation self-organizes into ordered tertiary microstructure supramolecular spherulites in accordance with the synergistically molecular attractor-repulsor theory (Scheme 1, Figures 1A and 1B) (Li et al., 2018; Wang et al., 2018; Xu et al., 2018). A hierarchical supramolecular artificial architecture with a series of multidimensional orthogonal hydrogen bonds in rigid crystalline framework is obtained from our bulky supramolecular spiro-terfluorene, 2,7-bis(3′,6′-bis(octyloxy)spiro[fluorene-9,9′-xanthen]-2-yl)spiro[fluorene-9,9′-thioxanthene]-10′,10′-dioxide (DOSFX-SFXSO). As a result of the confinement and stabilization of the rigid supramolecular framework, the molecules show an unusual unstable planar conformation in crystalline states. Interestingly, as expected, this planar conformation also enables molecules to self-assemble into higher-order condensed structures, namely, spherulites, rarely reported in organic electronics for optoelectronic devices. In contrast to conventional sulfur-containing conjugated molecules

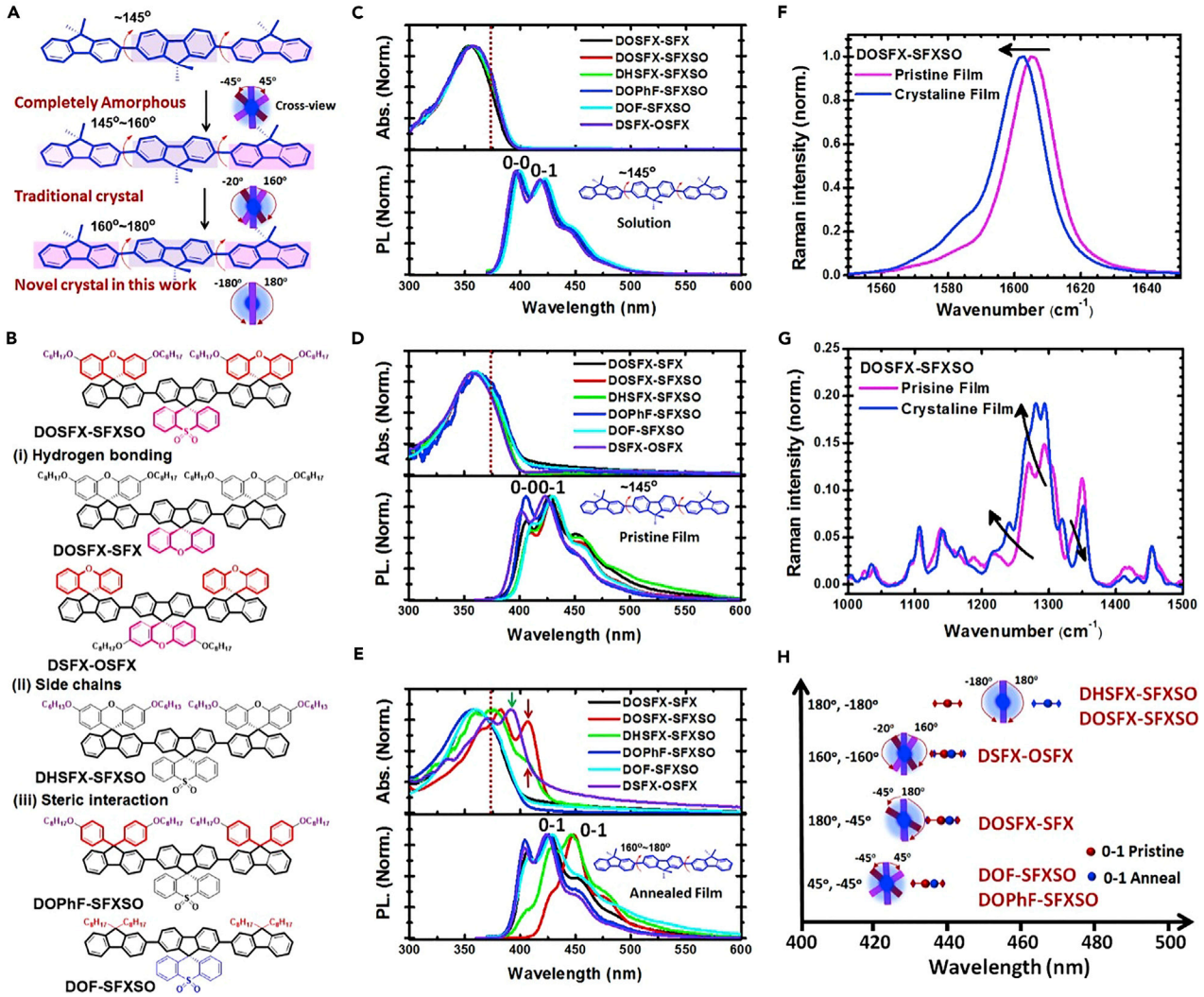

Figure 1. Molecular Structures, Photophysical Properties and Raman Spectra of Spiro-Terfluorenes

(A) Conformational transition and polymorphic behavior of fluorene-based semiconductors: completely amorphous state (∼-45°), crystalline domain with nonplanar conformation (145°∼160°), and crystalline domain with an oriented planar conformation (160°∼180°). A schematic illustration is also shown here to screen fluorene units from cross view (red, purple, and pink plates represent fluorene monomers along backbone structures).

(B) Chemical structures of terfluorene in this work.

(C) Absorption and emission spectra of spiro-functionalized terfluorenes in dilute dichloromethane solution (10^{-5} mol/mL).

(D) Absorption and emission spectra of pristine films of spiro-functionalized terfluorenes spin-coating from 10 mg/mL in toluene solution.

(E) Absorption and emission spectra of annealed films of spiro-functionalized terfluorenes. Both DOSFX-SFXSO and DHSFX-SFXSO were annealed at 160°C.

(F and G) Raman spectra of pristine spin-coated films and annealed films of DOSFX-SFXSO in the region of 1550∼1650 (F) and 900∼1500 (G) cm^{-1}, respectively.

(H) 0-1 Peaks of our fluorene-based six trimer molecule annealed films, together with their cross-sectional views of various conformations.

(Hoeben et al., 2005; Jin et al., 2018), our supramolecular terfluorene has an unusual suppression defect emission, which DOSFX-SFXSO can maintain at a high photoluminescent (PL) quantum efficiency of 55% under well-defined crystalline structures. Robust and stable excitonic behavior without any exciton trapped defect was observed for the supramolecular spherulites and explained this outstanding property.

RESULTS AND DISCUSSION

Rational Design of Steric Terfluorenes

As shown in Figure 1, six different terfluorenes sharing the same conjugated backbone were designed and synthesized. First, we show the three important design features on the chemical structure of DOSFX-SFXSO

in Figure 1B as follows: a centered spirofluorene unit SFXSO to induce the orthogonal hydrogen-bonding interaction, steric bulky units at 9-position of side fluorene to inhibit intermolecular stacking, and bulky side chains preventing side chain interdigitation. To date, as the most important component of bulky spiro-building blocks, the SFX unit is an effective steric group that suppresses intermolecular interactions. The difference between DOSFX-SFXSO and both 2′,7′-bis(9,9-bis(4-(octyloxy)phenyl)-9H-fluoren-2-yl)spiro [fluorene-9,9′-thioxanthene]-10′,10′-dioxide (DOPhF-SFXSO) and 2′,7′-bis(9,9-dioctyl-9H-fluoren-2-yl)spiro [fluorene-9,9′-thioxanthene]-10′,10′-dioxide (DOF-SFXSO) is the bulky steric unit on 9-position of the side fluorene units, which is necessary to investigate the steric interaction and the noncovalent interactions induced by the alkoxy chain. Frequently, noncovalent interactions among H, S, F, and O are useful to stabilize planar conformations and enhance crystallinity (Kim et al., 2013). According to our previous works, diverse and strong hydrogen-bonding interactions were observed in the SFXSO units (S=O···H-C), which could confer photophysical properties in aggregate state (Ou et al., 2017a, 2017b). Therefore, DOSFX-SFX was designed and prepared to determine the effect of this promising noncovalent interaction on conformation and crystalline properties. Furthermore, to explore the effect of the length of the substituted side chain, DHSFX-SFXSO with hexyl chains was prepared. The length of the alkoxy chain will precisely tune the molecular and chain packing in solid states (Liu et al., 2017a, 2017b). All materials were synthesized by Suzuki-type reaction with yield over 70%, and the detailed synthetic procedures and structure characterization are showed in Schemes S1 and S2 and Figures S28–S49. As showed in Figure S1 and Table S1, the on-set oxidation potential of terfluorene derivatives is around 0.86 to 0.98 V, so the highest occupied molecular orbital is around −5.62 to −5.72 eV. Similarly, the lowest unoccupied molecular orbital is around −2.54 to −2.69 eV and the bang gap is around 3.0 eV. The results indicate that nonconjugated electron-withdrawing sulfone groups have little influence on frontier orbitals. As expected, six terfluorenes have similar absorption and emission profiles, and only one absorption band with a maximum absorption peak of ∼355 and ∼360 nm, respectively, in both solution and pristine spin-coated films (Figures 1C and 1D), owing to a similar conjugated backbone structure. In addition, their emission spectra exhibit three well-resolved emission bands. The results indicate that the substitutions have a small influence on the electronic structures of terfluorene backbones. In contrast to the unchanged optical property of other controlled terfluorenes, DOSFX-SFXSO, DHSFX-SFXSO, and DSFX-OSFX show dramatic differences in the absorption and emission spectra of solid films after thermal treatment (Figure 1E). The well-structured absorption spectra of the annealed films of DOSFX-SFXSO and DHSFX-SFXSO have peaks at 382 and 379 nm, respectively, with the same shoulder absorption peak at approximately 406 nm (Figure 1E). Similarly, the maximum absorption peak of DSFX-OSFX is red-shifted from 357 to 390 nm. The above results indicate that molecular conformations are ordering and planarizing in the annealed film, resulting in a longer effective conjugation length (Bai et al., 2017; Ou et al., 2017a; Yu et al., 2018). Besides, the maximum emission peaks are bathochromic from 430 to 448 nm. In fact, the spectral changes are not complete in DHSFX-SFXSO. When the temperature was elevated from 160°C to 180°C, DOSFX-SFXSO and DHSFX-SFXSO displayed identical absorption and emission profiles (Figure S12). On the basis of our previous results about fluorene dimers and polymers, we can attribute these absorption and PL spectral shifts to conformational planarization of conjugated backbones.

Raman measurement is an effective tool to check the molecular conformational transition (Figures 1F and 1G) (Yu et al., 2018). Different aggregate states of DOSFX-SFXSO films were studied by Raman measurement to explain the molecular conformation and phase behavior. As indicated in Figures 1F–1H, the C=C stretching modes within spirofluorene units are bathochromic from 1,606 cm^{-1} of the amorphous phase to 1,602 cm^{-1} of the crystalline phase, which is attributable to the increased delocalized degree of π-electrons from a twisted conformation to a planar one. Compared with the amorphous state, the intensity ratio of the peaks 1,241, 1,266, 1,281, and 1,285 cm^{-1} to 1,602 cm^{-1} are increasing obviously in the crystalline phase. In addition, the vibrational frequency of the C-C stretching modes between spirofluorenes is hypochromatic from 1,349 cm^{-1} of the amorphous phase to 1,352 cm^{-1} of the crystalline phase. All the above Raman motions are similar to β-conformation in poly(9,9-dioctylfluoren-2,7-diyl) (PFO) and poly[4-(octyloxy)-9,9-diphenylfluoren-2,7-diyl]-co-[5-(octyloxy)-9,9-diphenylfluoren-2,7-diyl] (PODPF) (Liu et al., 2016, 2017a, 2017b; Yu et al., 2018). In this regard, we have further confirmed the formation of planar conformation in our DOSFX-SFXSO crystalline films.

To verify the assumption above, we tried to cultivate the single crystals of our six materials (Figures 2A and S2–S11, and Table S2). Interestingly, two types of DOSFX-SFXSO single crystals were obtained: flake and needle (Figure S2). Needle crystal of DOSFX-SFXSO displays two absorption peaks around 382 and 407 nm

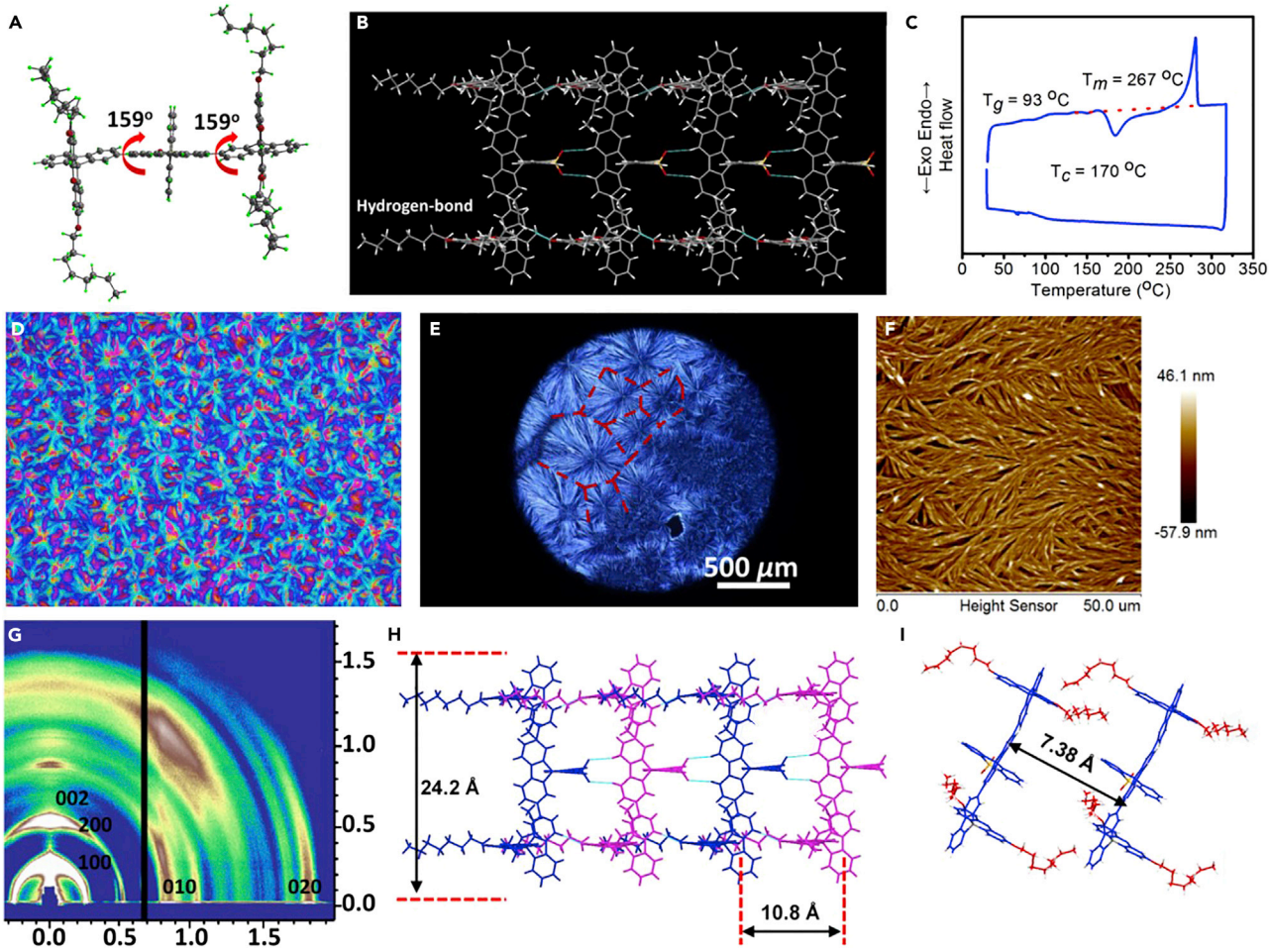

Figure 2. Crystal Structure and Packing Pattern, Thermal Behavior, Film Morphologies, and X-ray Diffraction of DOSFX-SFXSO

(A) Crystallographic structure of DOSFX-SFXSO.

(B) DOSFX-SFXSO-based hydrogen-bonded supramolecular polymer in crystalline framework.

(C) Differential scanning calorimetric curve of DOSFX-SFXSO.

(D and E) (D) Polarized optical and (E) cross-polarized optical micrographs of DOSFX-SFXSO annealed films.

(F) Atomic force microscopic image of DOSFX-SFXSO nanofiber in spherulites.

(G) Grazing-incident X-ray diffraction pattern image of DOSFX-SFXSO annealed films.

(H and I) Schematic representation of the molecular packing in DOSFX-SFXSO nanofibers. (H) The length of conjugated backbone and intermolecular distance. (I) The distance intermolecular π-π interaction.

and red-shifted emission (Figure S13), which is consistent with the results of annealing films, whereas the absorption spectra of flake crystals consist of peaks at 360 nm and 387 nm. As shown in Figure 2A, the DOSFX-SFXSO flake single crystal adopts a planar conformation with the same torsional angles of 159°. Owing to the large shift in absorption between the two crystals (~20 nm), the molecular conformation in needle crystals is more planar and torsional angles can be close to 180°. Furthermore, DHSFX-SFXSO also has two crystal polymorphs: needle and rod, and they display different PL profiles (Figure S14). The rod crystal presents a bent and *trans-cis* conformation with torsional angles of −29.0° and −146.1° (Figure S3). In addition, the quasi-planar conformation of DOSFX-SFXSO and the twisted conformation of DHSFX-SFXSO could also transform into fully coplanar conformations after thermal treatment at 160°C (Figures S15 and S16). As expected, DOF-SFXSO adopts a *trans-trans* conformation with large torsional angles of −138.3° and −142.0° (Figure S3). In a word, various absorption and PL spectra of our six materials also present different conformations and 0-1 emission peaks in annealed films (Figure 1H).

As displayed in Figures 2A and 2B, supramolecular hydrogen-bonding interactions between DOSFX-SFXSO molecules with characteristic distances of 2.639 Å (S=O···H-C between sulfone group, and

4,5-position hydrogen atoms of the centered fluorene unit) and 2.385 Å (C-O···H-C between O atom of octoxyl chains and 4,5-position hydrogen atoms of adjacent fluorene unit) suggest the formation of a DOSFX-SFXSO-based supramolecular polymeric framework in single crystal. The hydrogen bonds can restrict intramolecular rotation and trap coplanar conformations of DOSFX-SFXSO. In other words, the steric hindrance of SFX and SFXSO render DOSFX-SFXSO to separate from each other. In this way, the molecule may have a large space to freely rotate. Then, the conformation is locked by hydrogen bonding of SFXSO, and the van der Waals forces of alkyl chains also take part in this process (Figure 2B). The hydrogen bonds involved in 4,5-position hydrogen atoms of SFXSO and the fluorene group promote DOF-SFXSO to form dimers with π-π stacking (3.786 Å), which impede intramolecular rotation. As a result, DOF-SFXSO adopts a highly twisted conformation. Therefore, the orthogonal hydrogen bonds in our supramolecular framework can not only stabilize the planar conformation but also obtain higher self-organized crystalline structures in a condensed structure.

Upon combining the crystal data with the results of photophysics, we make three key observations. First, the small chemical modification in DOSFX-SFXSO with DOSFX-SFX leads to significant differences in conformational behavior, clearly indicating that the supramolecular steric hindrance (SSH) effect of SFXSO group plays a key role in conformational planarization. Second, replacing OSFX groups with 9,9-dioctylfluorenyl and 9,9-dioctoxyphenylfluorenyl groups demonstrates that the spiro-configuration is essential to conformational planarization. Finally, both hexoxyl and octoxyl substitutions can induce conformational planarization in crystals and annealed films, whereas hexoxyl substitution maintains a higher thermal annealing temperature, an indication that the length of alkyl chain also influences molecular conformation and packing.

Construction and Morphological Structure of Steric Terfluorenes-Based Supramolecular Spherulites

According to the differential scanning calorimetric curve in Figure 2C, a phase transformation (thermal-induced crystallization) of DOSFX-SFXSO occurs at 170°C and gives off a lot of latent heat ($\Delta Qc \approx -41.8$ kJ/mol), which is slightly less than the heat of fusion ($\Delta Hm \approx 49.6$ kJ/mol). Interestingly, if we kept a DOSFX-SFXSO pristine spin-coated film on a hot plate, we could see large supramolecular spherulites of several micrometers forming on the substrates (Figures 2D–2F and S17–S24). Besides, DSFX-OSFX crystalline structure could also be obtained after thermal annealing (Figure S25). Similar to conventional ones, our spherulites consisted of a centered crystal nucleus and a range of nanowires with an average width of ~100 nm and height of ~20 nm. As shown in Figures 2D and S17–S23, a large variation in spherulite semicrystalline was observed with domain size, from <10 up to 600 μm for edge-to-edge domain diameters. In fact, the domain size also decreases with increasing growth speed of crystal, indicating that slow crystallization promotes the molecular rearrangement and adjusts to the optimal packing position (Figure S23). Meanwhile, we also investigated the growth processing of spherulite at different thermal annealing temperatures ranging from 160°C to 186°C (Figure S22). First, no crystal was formed from 160°C to 168°C. Next, we obtained some small spherulites (~10 μm) at 172°C, but the growth rate was very slow. Finally, the growth rate was significantly enhanced when the temperature rose above 182°C. In this regard, the growth rate was significantly dependent on the annealing temperature with a critical threshold of 168°C. Different colors observed in Figure 2D indicate various molecular orientations in well-defined spherulites (Figures S20 and S21). We can postulate that the dark areas on the film surface might be located in lower areas or occupied relatively disordered amorphous regions. We can see very clearly the boundaries between different spherulite semicrystalline domains. To further uncover the molecular packing and arrangement in thermal annealed film, our spherulites were characterized by both grazing-incident X-ray diffraction and X-ray diffraction data (Figures 2G, S24, and S25). As presented in Figures 2G and S25, a broad diffraction ring with $Q \approx 1.50$ Å^{-1} along the out-of-plane and in-plane directions reveals the amorphous nature of DOSFX-SFXSO in the pristine spin-coated film. Interestingly, after thermal annealing, regular scattering patterns ($Q_z = 0.26$ Å^{-1} and 0.52 Å^{-1}, 100 and 200) are observed in the out-of-plane direction, indicating a lamella-like orientation in our spherulites. The interlayer distance (d = 24.20 Å) is comparable to the calculated conjugated backbone length (approximately 25.0 Å) of DOSFX-SFXSO, as illustrated in Figure 2H. Other slightly pattern plots at $Q_z = 0.58$ Å^{-1} (10.8 Å, 002) are also observed, attributed to the interchain distance and consistent with the calculated side chain distance (10.5Å) of DOSFX-SFXSO. Besides, we also attribute the stronger pattern plot at 0.85 Å^{-1} (d = 7.38 Å, 010 and 020) to the intermolecular π-π interaction (Figure 2I). Therefore, it is easy to conclude that the molecular packing model is similar to the single crystal of DOSFX-SFXSO, but the molecules may have a large torsional angle of >165° in supramolecular spherulites. In this regard, we assumed that molecules show oriented and ordered planar conformation with a periodic and dense arrangement, which further self-assembles into higher level well-defined spherulites. In turn,

we found out that our supramolecular framework is a key molecular design to induce planar conformation and obtain supramolecular spherulites.

Excitonic Behavior of Steric Terfluorene-Based Supramolecular Spherulites

In light-emitting conjugated solid system, defects resulting from both physical and chemical irregularities, can induce nonemissive interchain polaron pairs, and exciton-exciton annihilation, leading to low emission efficiency and unstable emission behavior (Haedler et al., 2015; Podzorov, 2013; Spano and Silva, 2014; Xie et al., 2012). Beyond possible structural defects, well-ordered condensed structures will provide an "excitonic landscape channel" to suppress physical defect emission and to ensure high light radiation (Haedler et al., 2015; Podzorov, 2013). Compared with the amorphous state, the β-conformation in polyfluorene is found to be an energetically favorable environment for excitons, including singlet and triplet exciton, associated with their oriented conformation and long effective conjugation length (Ariu et al., 2003; Hayer et al., 2005; Prins et al., 2006). As discussed in the first section, shoulder absorption peaks at 407 nm for DOSFX-SFXSO annealed films clearly reveal the formation of planar conformation. In addition, the red-shifted and well-resolved PL spectra with a more vibrational structure further confirmed this assumption. The peaks of DOSFX-SFXSO β-conformation in the room temperature (RT) PL spectra are located at 425, 445, 472, and 513 nm. At 425 nm, the PL peak has been assigned to the S1ssi (0-0) transition. The β-conformation 0-0 PL emission peak is thus red-shifted by 20 nm compared with the 0-0 peak detected from the amorphous ones, attributable to the smaller energy gap for the β-conformational molecules (Lin et al., 2014; Liu et al., 2016; Yu et al., 2016). The intensity ratio of 0-0 to 0-1 emission band are high in spin-coated amorphous films, indicating an enhancement of the Huang-Rhys parameter and resulting from a larger configuration and relaxation in the excited states (Eggimann et al., 2019).

As indicated in Figure 3A, the lifetime of pristine film and crystalline film are 380 and 530 ps, respectively, indicating that DOSFX-SFXSO β-conformation leads to the increase in PL lifetime, that crystalline phase is able to block defect emission. It can be seen that in the β-conformation PL spectra, emission peaks red-shift by 13 nm as the temperature is reduced from RT to 5 K (Figures 3B and S26), which might be the result of the reduced vibronic coupling of the fluorene units. The increase in the intensity of the 0-0 peak in PL spectra at low temperatures seems to suggest that the terfluorene chain is more planar, indicating that the contribution from increased π-electron delocalization plays a more significant role than assumed. The 0-1 vibronic PL peaks of crystalline-phase DOSFX-SFXSO do not split like PFO and PODPF β-conformation at lower temperatures. The reason we do not observe the vibrational fine structure is because the fraction of the material in the crystalline phase is much larger than that of PODPF/PFO in the β-conformation. This leads to an inhomogeneous broadening of the peaks. We see similar trends for PODPF β-conformation low-temperature PL spectra with a red-shift in emission, decreasing to 0-1 vibronic peak intensity, and increasing to 0-0/0-1 peak spacing with decreasing temperature.

According to previous work, serious fluorescence quenching usually occurs in a highly crystalline condensed structure of conjugated molecules, such as aggregation-induced quenching resulting to small radiative decay rate (k_r) and high trapping rate (Jin et al., 2018). For example, the PL quantum efficiencies of DOSFX-SFX annealed films are approximately 16%, which is a decrease of nearly 70% from those of pristine spin-coated films (48%) (Table 1). Notably, photoluminescent quantum yield (PLQY) is 58% and 55% for DOSFX-SFXSO pristine and annealed films, and 45% and 36% for DHSFX-SFXSO ones, respectively, which are significantly different from those of conventional light-emitting conjugated molecules (Table 1). Increased degrees of structural order can reasonably suppress physical defects and enable crystalline structures to show robust emission. Besides, this assumption is also effectively confirmed by the well-resolved vibronic structure and narrow spectral profiles in PL decay from planar conformation and amorphous spin-coated films at RT following ultrafast excitation at 365 nm (Figures 3C and 3D). Figures 3C, 3D, and S27 show the time-resolved PL spectra of DOSFX-SFXSO and DSFX-OSFX films at three different times following 365-nm excitation. The most striking observation is that for all observations between 0 and 4.5 ns, the emission spectra from the β-conformation film are significantly different from those observed in the amorphous ones. As expected, in amorphous DOSFX-SFXSO and DSFX-OSFX crystalline films, long-wavelength and broad green-band "defect" emissions at 500 nm are found in the PL spectra at 1.0–4.5 ns, originating from the nonradiative intermolecular aggregation-induced excimer (Cacialli et al., 2002; Eggimann et al., 2019). As we discussed above, DSFX-OSFX also shows excellent crystalline structure in annealed films, but it also had a residual strong defect emission at long-wavelength emission (520 nm) after a delay of 2.5 ns (Figure S27), indicating that residual physical defect "excimer" may not completely suppress in conventional crystalline structure without order and orientation at molecular level. Remarkably, the annealed

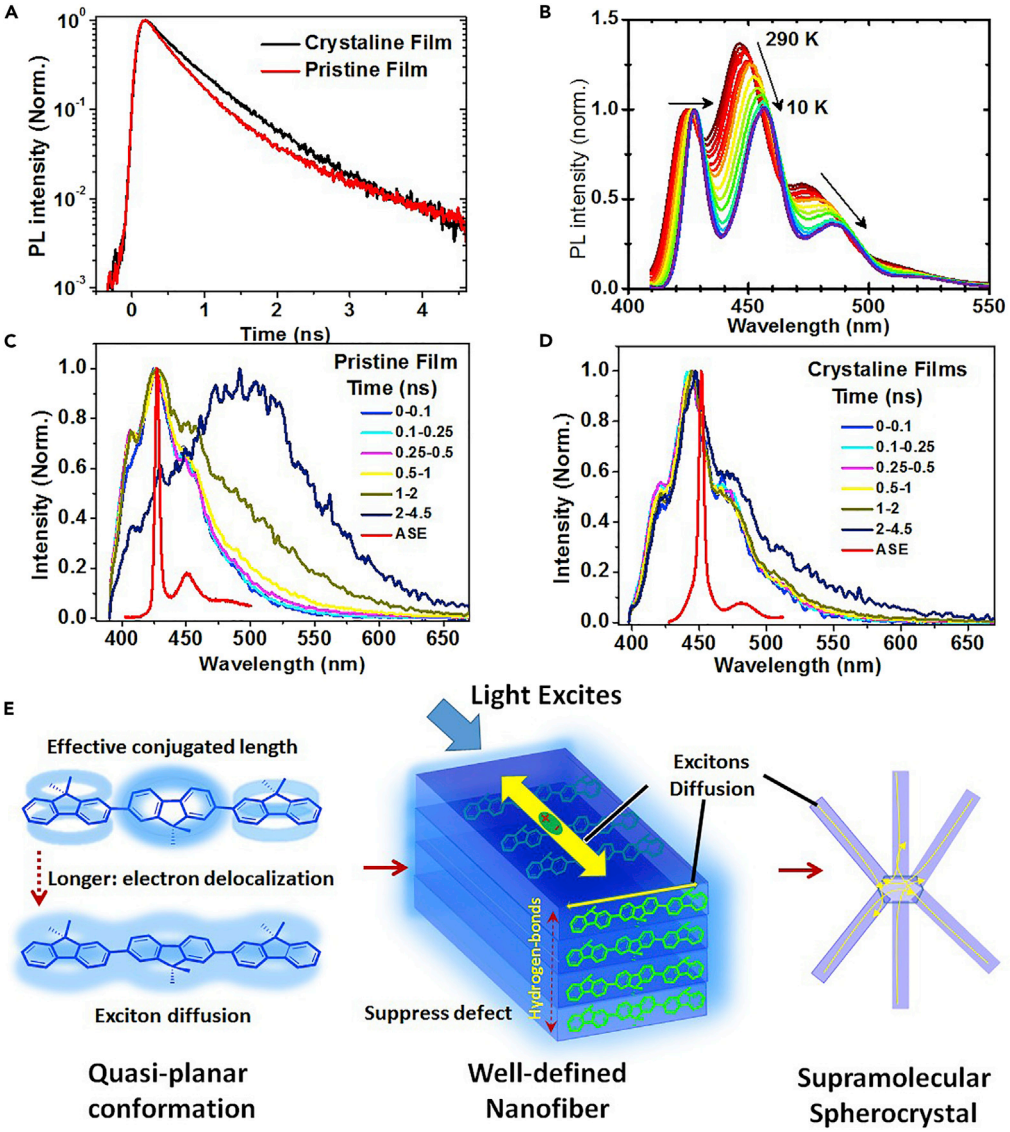

Figure 3. Transient Grating PL Spectra of DOSFX-SFXSO in Various States

(A) Normalized PL kinetics of DOSFX-SFXSO and DOSFX-SFX amorphous spun films and β-conformation annealed films. (B–D) (B) Temperature-dependent PL spectra of DOSFX-SFXSO β-conformation annealed films from 10 K to 290 K. The PL spectra of DOSFX-SFXSO amorphous (C) and β-conformation (D) films excited at 365 nm using a frequency-doubled, mode-locked Ti:sapphire laser and measured at 0–4.5 ns following excitation. The ASE spectra of two DOSFX-SFXSO films were excited by 355 nm laser.

(E) Schematic illustration of exciton diffusion in our well-defined condensed spherocrystals. Complete electron delocalization along p-orbit conjugated backbone structure enables quasi-planar conformational molecular structure to promote exciton diffusion.

DOSFX-SFXSO leads to slight increase in PL lifetime and reduction in the long-wavelength defect emission, indicating that the DOSFX-SFXSO crystalline phase is able to suppress the "defect" emission effectively (Figure 3E). This is possibly due to the low energy of the DOSFX-SFXSO crystalline phase, as seen in absorption and PL, similar to the β-conformational domain in PFO and PODPF. Well-defined condensed structures, consisting of oriented planar conformation and highly ordered molecular packing, will effectively suppress the defect emission in our crystalline nanostructure (Figure 3E). What's more, amplified spontaneous emission (ASE) peaks of DOSFX-SFXSO pristine and annealed films estimated at 426 and 452 nm, attributed to 0-1 band emission, also effectively confirmed the planarization of conjugated backbone structure in supramolecular spherulites (Figures 3C and 3D). Of course, there is also a low fraction of longer wavelength in our DHSFX-SFXSO

Entry	$\lambda_{Abs\ max}$ (nm)			$\lambda_{PL\ max}$ (nm)			η			
	Sol.	Film	Ann.	Sol.	Film	Ann.	Sol.	Film	Ann	Enh.
DOSFX-SFX	354	359	360	397, 420	406, 427	405, 423, 452	96%	48%	16%	−67%
DOSFX-SFXSO	356	360	363, 382, 407	399, 420	410, 430	427, 450, 476	90%	58%	55%	−5%
DOF-SFXSO	356	360	359	400, 422	410, 430	407, 429, 453	89%	36%	20%	−45%
DOPhF-SFXSO	357	359	358	398,421	405, 426	404, 427, 452	92%	40%	20%	−50%
DHSFX-SFXSO	355	359	360, 378, 404	399, 420	410, 430	406, 427, 447, 475	95%	45%	36%	−20%
DSFX-OSFX	357	357	369, 390	395, 418	401, 423	403, 423, 452	98%	62%	38%	−40%

Table 1. Photophsical Property of Selective Terfluorenes in Various States
Sol., diluted solution; Ann., annealed films; Enh., increased η ratio of film states after thermal annealing.

β-conformation films, attributing to the disordered domain in the film states. The strong electronic coupling in amorphous films, also called a physical defect, is detrimental to emission behavior in solid states (Cacialli et al., 2002). In the last several decades, green-band emission is a big obstacle to the induction of unstable and low emission efficiency, which is a key problem in the construction of a high-performance stable fluorene-based semiconductor. Our observation strongly confirms that the aggregation-caused excimer formation is an approach to induce this green emission as reported by Vacha et al. (Honmou et al., 2014; Nakamura et al., 2018).

In summary, we have designed and synthesized a range of terfluorenes with various side chain and substituted steric units. Interestingly, supramolecular DOSFX-SFXSO shows an unusually planar conformation (i-conformation) in the annealed film with perfect supramolecular spherulites resulting from the synergistic effects of hydrogen bonds and steric interaction. Strikingly, with regard to the crystalline-quenched emission in conventional light-emitting solid states, the strong luminance of our ordered and uniform artificial architectures is obtained with a high PLQY of 55%. In our assumption, this unique property is attributable to two factors: the β-conformation provides an energetically favorable environment for excitons. Meanwhile, the undesirable physical defects, such as aggregation-induced excimer, are effectively suppressed, as confirmed by the transient PL kinetics measurement. Long wavelength emission at 500 nm was observed in pristine films but absent in annealed films, which strongly supported the aggregation mechanism in fluorene green-band emission. In combination with the high molecular packing, such a crystalline-enhanced emission in our designed ordered artificial architectures could enable light-emitting optoelectronic devices that apply this well-defined structure as a photoelectric conversion antenna. These could contribute to the construction of high-performance organic light-emitting field transistors and electrical pumped organic lasers.

Limitations of the Study

In this study, the DOSFX-SFXSO with planar conformation in the annealed film can easily self-organize into perfect supramolecular spherulites via the synergistic effects of hydrogen bonds and steric interaction. However, accurate roles of hydrogen bondings and molecular packing behaviors in conformational planarization are not fully understood here, and electronic properties of spherulites and microcrystals need to be further investigated.

METHODS

All methods can be found in the accompanying Transparent Methods supplemental file.

SUPPLEMENTAL INFORMATION

Supplemental Information can be found online at https://doi.org/10.1016/j.isci.2019.06.002.

ACKNOWLEDGMENTS

The work was supported by the National Natural Science Foundation of China (61874053, 61805117), National Key Basic Research Program of China (973) (2015CB932200), Natural Science Funds of the Education Committee of Jiangsu Province (18KJA430009), Project funded by China Postdoctoral Science Foundation,

"High-Level Talents in Six Industries" of Jiangsu Province (XYDXX-019), Natural Science Foundation of Jiangsu Province (BK20171470, BK20160991), the open research fund from Key Laboratory for Organic Electronics and Information Displays and State Key Laboratory of Supramolecular Structure and Materials (sklssm2019017), and Postgraduate Research & Practice Innovation Program of Jiangsu Province (KYCX18-1121).

AUTHOR CONTRIBUTIONS

J.L., L.X., and W.H. performed the major study and wrote the manuscript. J.L., C.O., and L.B. were responsible for the preparation and structure characterization of polymers and supramolecular spherulites. N.J.C., C.O., and X.W. collected the optical data. C.S., Y.H., and J.C.-G. investigated the excitonic behavior and decay time analysis of DOSFX-SFXSO. C.O., J.W., and L.B. obtained a range of single crystals of our six materials and analyzed the data. D.D.C.B. revised the manuscript and provided some suggestions. All authors discussed the results and commented on the manuscript at all stages.

DECLARATION OF INTERESTS

The authors declare no competing interests.

Received: December 24, 2018
Revised: April 16, 2019
Accepted: June 3, 2019
Published: June 28, 2019

REFERENCES

Aida, T., Meijer, E.W., and Stupp, S.I. (2012). Functional supramolecular polymers. Science *335*, 813.

Ariu, M., Sims, M., Rahn, M.D., Hill, J., Fox, A.M., Lidzey, D.G., Oda, M., Cabanillasgonzalez, J., and Bradley, D.D.C. (2003). Exciton migration in β-phase poly(9,9-dioctylfluorene). Phys. Rev. B *67*, 683–684.

Bai, L.B., Liu, B., Han, Y.M., Yu, M.N., Wang, J., Zhang, X.W., Ou, C.J., Lin, J.Y., Zhu, W.S., and Xie, L. (2017). Steric-hindrance-functionalized polydiarylfluorenes: conformational behavior, stabilized blue electroluminescence, and efficient amplified spontaneous emission. ACS Appl. Mater. Interfaces *9*, 37856–37863.

Barford, W., and Duffy, C.D.P. (2006). Role of quantum coherence and energetic disorder in exciton transport in polymer films. Phys. Rev. B *74*, 2428–2435.

van de Burgt, Y., Lubberman, E., Fuller, E.J., Keene, S.T., Faria, G.C., Agarwal, S., Marinella, M.J., Alec Talin, A., and Salleo, A. (2017). A non-volatile organic electrochemical device as a low-voltage artificial synapse for neuromorphic computing. Nat. Mater. *16*, 414.

Cacialli, F., Wilson, J.S., Michels, J.J., Daniel, C., Silva, C., Friend, R.H., Severin, N., Samorì, P., Rabe, J.P., O'Connell, M.J., et al. (2002). Cyclodextrin-threaded conjugated polyrotaxanes as insulated molecular wires with reduced interstrand interactions. Nat. Mater. *1*, 160–164.

Chen, Y., Kushner, A.M., Williams, G.A., and Guan, Z. (2012). Multiphase design of autonomic self-healing thermoplastic elastomers. Nat. Chem. *4*, 467–472.

Costa, A., Hood, I.V., and Berger, J.M. (2013). Mechanisms for initiating cellular DNA replication. Annu. Rev. Biochem. *82*, 25.

Eggimann, H.J., Le Roux, F., and Herz, L.M. (2019). How β-phase content moderates chain conjugation and energy transfer in polyfluorene films. J. Phys. Chem. Lett. *10*, 1729–1736.

Eisele, D.M., Arias, D.H., Fu, X., Bloemsma, E.A., Steiner, C.P., Jensen, R.A., Rebentrost, P., Eisele, H., Tokmakoff, A., Lloyd, S., et al. (2014). Robust excitons inhabit soft supramolecular nanotubes. Proc. Nat. Acad. Sci. U S A *111*, E3367–E3375.

Haedler, A.T., Kreger, K., Issac, A., Wittmann, B., Kivala, M., Hammer, N., Köhler, J., Schmidt, H.-W., and Hildner, R. (2015). Long-range energy transport in single supramolecular nanofibres at room temperature. Nature *523*, 196.

Hayer, A., Khan, A.L.T., Friend, R.H., and Köhler, A. (2005). Morphology dependence of the triplet excited state formation and absorption in polyfluorene. Phys. Rev. B *71*, S3–S4.

Heeger, A.J. (2010). Semiconducting polymers: the third generation. Chem. Soc. Rev. *39*, 2354–2371.

Hoeben, F.J., Jonkheijm, P., Meijer, E.W., and Schenning, A.P. (2005). About supramolecular assemblies of pi-conjugated systems. Chem. Rev. *36*, 1491–1546.

Honmou, Y., Hirata, S., Komiyama, H., Hiyoshi, J., Kawauchi, S., Iyoda, T., and Vacha, M. (2014). Single-molecule electroluminescence and photoluminescence of polyfluorene unveils the photophysics behind the green emission band. Nat. Commun. *5*, 4666.

Huang, Y., Xing, J., Gong, Q., Chen, L.-C., Liu, G., Yao, C., Wang, Z., Zhang, H.-L., Chen, Z., and Zhang, Q. (2019). Reducing aggregation caused quenching effect through co-assembly of PAH chromophores and molecular barriers. Nat. Commun. *10*, 169.

Jin, X.-H., Price, M.B., Finnegan, J.R., Boott, C.E., Richter, J.M., Rao, A., Menke, S.M., Friend, R.H., Whittell, G.R., and Manners, I. (2018). Long-range exciton transport in conjugated polymer nanofibers prepared by seeded growth. Science *360*, 897–900.

Kim, B.G., Jeong, E.J., Chung, J.W., Seo, S., Koo, B., and Kim, J. (2013). A molecular design principle of lyotropic liquid-crystalline conjugated polymers with directed alignment capability for plastic electronics. Nat. Mater. *12*, 659–664.

Lehn, J.M. (2010). Toward self-organization and complex matter. Science *33*, 281.

Li, X., Wolanin, P.J., MacFarlane, L.R., Harniman, R.L., Qian, J., Gould, O.E.C., Dane, T.G., Rudin, J., Cryan, M.J., Schmaltz, T., et al. (2017). Uniform electroactive fibre-like micelle nanowires for organic electronics. Nat. Commun. *8*, 15909.

Li, Y.-X., Wang, S.-S., Yu, Y., Zhang, H., Wang, W.-Y., Yang, R.-Q., Xie, L.-H., Liu, F., Lin, Z.-Q., Shi, N.-E., et al. (2018). SMART design of a bulk-capped supramolecular segment for the assembly into organic interdigital lipid bilayer-like (ILB) nanosheets. Small *14*, 1703151.

Lin, H., Camacho, R., Tian, Y., Kaiser, T.E., Würthner, F., and Scheblykin, I.G. (2010). Collective fluorescence blinking in linear J-aggregates assisted by long-distance exciton migration. Nano Lett. *10*, 620–626.

Lin, J.Y., Zhu, W.S., Liu, F., Xie, L.H., Zhang, L., Xia, R., Xing, G.C., and Huang, W. (2014). A rational molecular design of β-phase polydiarylfluorenes: synthesis, morphology, and organic lasers. Macromolecules *47*, 1001–1007.

Liu, S., Tang, Z.-R., Sun, Y., Colmenares, J.C., and Xu, Y.-J. (2015). One-dimension-based spatially ordered architectures for solar energy conversion. Chem. Soc. Rev. *44*, 5053–5075.

Liu, B., Lin, J., Liu, F., Yu, M., Zhang, X., Xia, R., Yang, T., Fang, Y., Xie, L., and Huang, W. (2016). A highly crystalline and wide-bandgap polydiarylfluorene with β-phase conformation toward stable electroluminescence and dual amplified spontaneous emission. ACS Appl. Mater. Interfaces *8*, 21648–21655.

Liu, B., Lin, J., Yu, M., Li, B., Xie, L., Ou, C., Liu, F., Li, T., Lu, D., and Huang, W. (2017a). Hereditary character of alkyl-chain length effect on β-phase conformation from polydialkylfluorenes to bulky polydiarylfluorenes. J. Phys. Chem. C *121*, 19087–19096.

Liu, G., Liu, J., Ye, X., Nie, L., Gu, P., Tao, X., and Zhang, Q. (2017b). Self-healing behavior in a thermo-mechanically responsive cocrystal during a reversible phase transition. Angew. Chem. Int. Ed. *56*, 198–202.

Lunt, R.R., Benziger, J.B., and Forrest, S.R. (2010). Relationship between crystalline order and exciton diffusion length in molecular organic semiconductors. Adv. Mater. *22*, 1233–1236.

Mikhnenko, O.V., Blom, P.W.M., and Nguyen, T.-Q. (2015). Exciton diffusion in organic semiconductors. Energ. Environ. Sci. *8*, 1867–1888.

Nakamura, T., Sharma, D.K., Hirata, S., and Vacha, M. (2018). Intrachain aggregates as the origin of green emission in polyfluorene studied on ensemble and single-chain level. J. Phys. Chem. C *122*, 8137–8146.

Noriega, R., Rivnay, J., Vandewal, K., Koch, F.P., Stingelin, N., Smith, P., Toney, M.F., and Salleo, A. (2013). A general relationship between disorder, aggregation and charge transport in conjugated polymers. Nat. Mater. *12*, 1037–1043.

Oh, J.Y., Rondeau-Gagné, S., Chiu, Y.-C., Chortos, A., Lissel, F., Wang, G.-J.N., Schroeder, B.C., Kurosawa, T., Lopez, J., Katsumata, T., et al. (2016). X Intrinsically stretchable and healable semiconducting polymer for organic transistors. Nature *539*, 411–415.

Ou, C., Ding, X.H., Li, Y.X., Zhu, C., Yu, M.N., Xie, L., Lin, J.Y., Xu, C., and Huang, W. (2017a). Conformational effect of polymorphic terfluorene on photophysics, crystal morphologies and lasing behaviors. J. Phys. Chem. C *121*, 14803–14810.

Ou, C.J., Zhu, C., Ding, X.H., Yang, L., Lin, J.Y., Xie, L.H., Qian, Y., Xu, C.X., Zhao, J.F., and Huang, W. (2017b). Dimerization effect of fluorene-based semiconductors on conformational planarization for microcrystal lasing. J. Mater. Chem. C *5*, 5345–5355.

Peumans, P., Yakimov, A., and Forrest, S.R. (2003). Small molecular weight organic thin-film photodetectors and solar cells. J. Appl. Phys. *93*, 3693–3723.

Podzorov, V. (2013). Conjugated polymers: long and winding polymeric roads. Nat. Mater. *12*, 947–948.

Prins, P., Grozema, F.C., Nehls, B.S., Farrell, T., Scherf, U., and Siebbeles, L.D.A. (2006). Enhanced charge-carrier mobility in β-phase polyfluorene. Phys. Rev. B *74*, 113203.

Sanchez, C., Arribart, H., and Guille, M.M. (2005). Biomimetism and bioinspiration as tools for the design of innovative materials and systems. Nat. Mater. *4*, 277.

Sengupta, S., and Würthner, F. (2013). Chlorophyll j-aggregates: from bioinspired dye stacks to nanotubes, liquid crystals, and biosupramolecular electronics. Acc. Chem. Res. *46*, 2498–2512.

Spano, F.C., and Silva, C. (2014). H- and J-aggregate behavior in polymeric semiconductors. Annu. Rev. Phys. Chem. *65*, 477–500.

Venkateshvaran, D., Nikolka, M., Sadhanala, A., Lemaur, V., Zelazny, M., Kepa, M., Hurhangee, M., Kronemeijer, A.J., Pecunia, V., Nasrallah, I., et al. (2014). Approaching disorder-free transport in high-mobility conjugated polymers. Nature *515*, 384.

Vogelsang, J., Adachi, T., Brazard, J., Vanden Bout, D.A., and Barbara, P.F. (2011). Self-assembly of highly ordered conjugated polymer aggregates with long-range energy transfer. Nat. Mater. *10*, 942.

Wang, Z., Xu, W., Liu, L., and Zhu, T.F. (2016). A synthetic molecular system capable of mirror-image genetic replication and transcription. Nat. Chem. *8*, 698.

Wang, S.S., Rong, R., Jin, L.Z., Yang, S.S., Li, Y.X., Zhang, H., Xiong, Y.W., Sun, L.T., Cao, H.T., and Xie, L.H. (2018). Variable segment roles: modulation of the packing modes, nanocrystal morphologies and optical emissions. Nanoscale *10*, 13310–13314.

Wu, D.Y., Meure, S., and Solomon, D. (2008). Self-healing polymeric materials: a review of recent developments. Prog. Polym. Sci. *33*, 479–522.

Xie, L.H., Yin, C.R., Lai, W.Y., Fan, Q.L., and Huang, W. (2012). Polyfluorene-based semiconductors combined with various periodic table elements for organic electronics. Prog. Polym. Sci. *37*, 1192–1264.

Xu, M., Ou, C.-J., Gao, C., Lin, J.-Y., Xu, W., Yu, M.-N., Zhu, W.-S., Lin, Z.-Q., Bai, L.-B., Han, Y.-M., et al. (2018). Hydrogen-bonded-assisted supramolecular microwires for pure violet lasers: benefits of preventing intermolecular π–π stacking and aggregation in single crystals. Mater. Chem. Front. *2*, 2307–2312.

Yan, H., Chen, Z., Zheng, Y., Newman, C., Quinn, J.R., Dötz, F., Kastler, M., and Facchetti, A. (2009). A high-mobility electron-transporting polymer for printed transistors. Nature *457*, 679.

Yang, Y., and Urban, M.W. (2013). Self-healing polymeric materials. Chem. Soc. Rev. *42*, 7446–7467.

Yang, Y., Liu, G., Liu, J., Wei, M., Wang, Z., Hao, X., Maheswar Repaka, D.V., Ramanujan, R.V., Tao, X., Qin, W., and Zhang, Q. (2018). Anisotropic magnetoelectric coupling and cotton–mouton effects in the organic magnetic charge-transfer complex pyrene–F4TCNQ. ACS Appl. Mater. Interfaces *10*, 44654–44659.

Ye, H., Liu, G., Liu, S., Casanova, D., Ye, X., Tao, X., Zhang, Q., and Xiong, Q. (2018). Molecular-barrier-enhanced aromatic fluorophores in cocrystals with unity quantum efficiency. Angew. Chem. Int. Ed. *57*, 1928–1932.

Yu, M.N., Liu, B., Lin, J.Y., Li, T., Lu, D., Liu, F., and Zhu, W.S. (2016). Nondilute 1,2-dichloroethane solution of poly(9,9-dioctylfluorene-2,7-diyl): a study on the aggregation process. Chinese J. Polym. Sci. *34*, 1311–1318.

Yu, M.-N., Soleimaninejad, H., Lin, J.-Y., Zuo, Z.-Y., Liu, B., Bo, Y.-F., Bai, L.-B., Han, Y.-M., Smith, T.A., Xu, M., et al. (2018). Photophysical and fluorescence anisotropic behavior of polyfluorene β-conformation films. J. Phys. Chem. Lett. *9*, 364–372.

Zhang, Y., Gong, S., Zhang, Q., Ming, P., Wan, S., Peng, J., Jiang, L., and Cheng, Q. (2016). Graphene-based artificial nacre nanocomposites. Chem. Soc. Rev. *45*, 2378–2395.

ISCI, Volume *16*

Supplemental Information

Hierarchical Uniform Supramolecular Conjugated Spherulites with Suppression of Defect Emission

Changjin Ou, Nathan J. Cheetham, Jiena Weng, Mengna Yu, Jinyi Lin, Xuhua Wang, Chen Sun, Juan Cabanillas-Gonzalez, Linghai Xie, Lubing Bai, Yamin Han, Donal D.C. Bradley, and Wei Huang

Supplemental Information

Transparent Methods

Materials and reagents

All reagents were purchased from Sigma-Aldrich, Merck and Alfa Aesar, and used without further purification unless stated otherwise. Anhydrous THF was dried by sodium using benzophenone as indicator. The synthetic routes of spiro[fluorene-9,9'-thioxanthene] 10',10'-dioxide and 2-bromo-3',6'-bis(octyloxy)spiro[fluorene-9,9'-xanthene] were followed the literatures (Ou and Zhu, et al., 2017; Ou and Ding, et al., 2017; Zuo, et al., 2018).

Characterization

^{1}H and ^{13}C NMR spectrum was recorded on a Bruker 400 MHz spectrometer in $CDCl_3$ with tetramethylsilane (TMS) as the interval standard. Absorption spectra were measured with a Shimadzu UV-3600 spectrometer at 25 ^{o}C, and emission spectra were recorded on a Shimadzu RF-5301(PC) luminescence spectrometer. DSC measurement was acquired using a Shimadzu Instruments DSC-60A. DSC data were collected at a rate of 10 ^{o}C/min for both of the baseline and sample. Thermogravimetric analyses (TGA) were conducted by a Shimadzu DTG-60H under a heating rate of 10 ^{o}C/min and a nitrogen flow rate of 50 cm^3/min. Cyclic voltammetric (CV) studies were conducted using an CHI660C Electrochemical Work station in a typical three-electrode cell with a platinum sheet working electrode, a platinum wire counter electrode, and a silver/silver nitrate (Ag/Ag^+) reference electrode. All electrochemical experiments were carried out under a nitrogen

atmosphere at room temperature in an electrolyte solution of 0.1 M tetrabutylammonium hexafluorophosphate (n-Bu_4NPF_6) in CH_2Cl_2 at a sweeping rate of 0.1 V/s. According to the redox onset potentials of the CV measurements, the HOMO/LUMO energy levels of the materials are estimated based on the reference energy level of ferrocene (4.8 eV below the vacuum): HOMO/ LUMO = -[E_{onset} – $E_{(Fc/Fc+)}$+ 4.8] eV. For scanning electron microscopic (SEM) studies, a drop of 20 μL solutions were placed onto silicon substrates, and the solvent was left to evaporate. The samples were then examined with a field emission SEM (Hitachi, S-4800) at an accelerating voltage of 3 kV. The film morphologies of films were recorded with a Bruker's Dimension Icon AFM in tapping mode (Bruker's Sb/Si probe tip with a resonant frequency 320 kHz and the spring constant 42 Nm^{-1}). The Single crystal data collection was performed at 100 or 298 K on a Bruker 2000 CCD area detector using graphite-monochromated Mo Kα radiation (λ = 0.71073 Å). All structures were solved by direct methods using OLEX2 and refined against F^2 using SHELXL-2014. Hydrogen atoms were fixed geometrically and refined isotropically. To measure the fluorescence lifetime, the incident 390 nm, 150-fs laser pulses were generated from a Coherent TOPAS-C optical parametric amplifier; pumped by a 1 kHz Coherent Legend regenerative amplifier that is seeded by a Coherent Vitesse oscillator. These input laser pulses were focused by a lens (f = 20 cm) on the samples solution in a 1-mm-thick quartz cell (beam spot ~1 mm inside the cell). The emission from the samples was collected at a backscattering angle of 150° by a pair of lenses and directed to an Optronis Optoscope^{TM} streak camera system which has an ultimate

temporal resolution of 6 ps. CD spectra were collected using a JASCO J-820 spectropolarimeter (Tokyo, Japan) and CD measurements were from 300 to 450 nm, the data pitch was 0.5 nm, scan speed was 800 nm/min, response time was 0.5 s, and bandwidth was 1 nm. GIXD measurements were performed on Beamline 7.3.3 at the Advanced Light Source (ALS) at the Lawrence Berkeley National Laboratory. An X-ray beam impinged onto the sample at a grazing angle above and below the critical angle of the polymer film (αc = 0.16), but below the critical angle of the silicon substrate (αc = 0.22). The wavelength of X-rays was 1.240 Å, and the scattered intensity was detected by PILATUS 1M detector. The sample was loaded on silicon nitride substrate, and the beam energy used here is 284.4 eV which generally probes the carbon edge resonance.

ASE characterization

For ASE characterization, second harmonic generation (400 nm) of a re-generative amplifier (Spitfire, spectra Physics) was used as the optical pump source. The spot size of the pump laser beam focused on the samples was about 0.13 mm in diameter, which was perpendicular to the sample, and pump energy was controlled by an attenuator wheel and measured by laser power meter. The emission was detected by the optical fiber and then dispersed to a monochromator equipped with a charge coupled device detector (iDus, Andor).

Scheme S1. The synthetic route of 2,7-bis(4,4,5,5-tetramethyl-1,3,2-dioxaborolan-2-yl)spiro[fluorene-9,9'-thioxanthene] 10',10'-dioxide.

~~Synthesis procedures~~

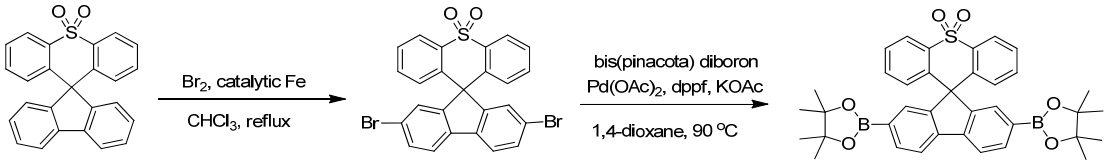

***Scheme* S2. The synthetic routes of bulk terfluorenes.**

~~**Scheme S1. The synthetic route of 2,7-bis(4,4,5,5-tetramethyl-1,3,2-dioxaborolan-2-yl)spiro[fluorene-9,9'-thioxanthene] 10',10'-dioxide.**~~

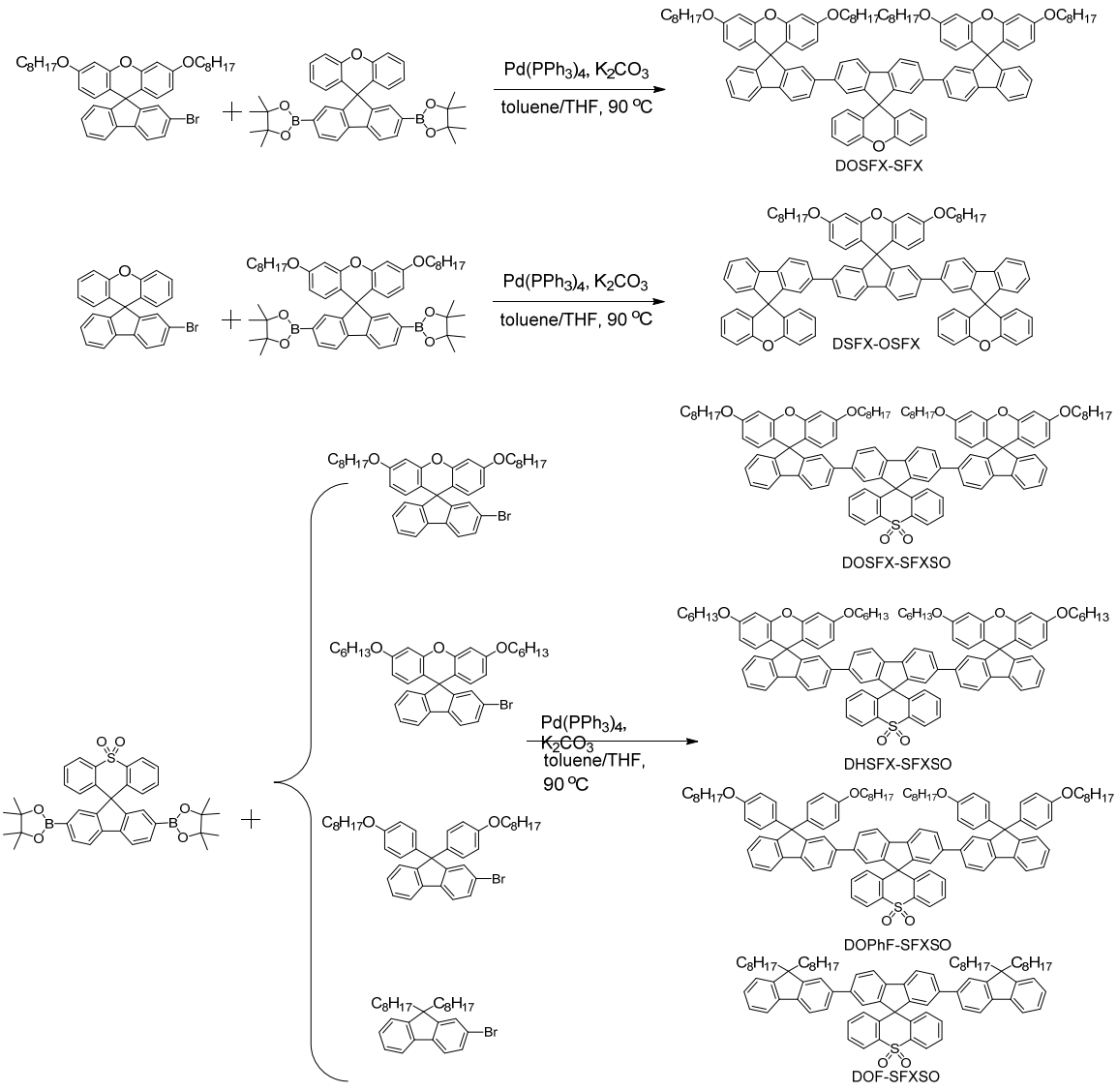

~~*Scheme* S2. The synthetic routes of bulk terfluorenes.~~

Synthesis of 2,7-dibromospiro[fluorene-9,9'-thioxanthene] 10',10'-dioxide

To a 2-kneck round flask, spiro[fluorene-9,9'-thioxanthene] 10',10'-dioxide (1.9 g, 5 mmol) and catalytic amount Fe powder was added, and then dissolved with chloroform (50 mL). Bromine (1.84 g, 11.5 mmol) was added, and then heated to reflux overnight. Sodium hydrogen sulfite aqueous solution was added to quench the excess of bromine, and then extracted with dichloromethane. The combined organic abstracted was dried over anhydrous $MgSO_4$ and filtered. The solution was evaporated under vacuum condition. The product was purified with silica gel column chromatography to afford a white solid (2.5 g, 92.6%). ^{1}H NMR(400 Mz, $CDCl_3$) δ 8.26 (dd, J = 8.0, 1.2 Hz, 2H), 7.69 (d, J = 8.0 Hz, 2H), 7.57 (dd, J = 8.0, 1.6 Hz, 2H), 7.52 (t, J = 7.6 Hz, 2H), 7.46 (d, J = 1.6 Hz, 2H), 7.32 (td, J = 8.8 Hz, 2H), 6.56 (d, J = 8.0 Hz, 2H). ^{13}C NMR(100 Mz, $CDCl_3$) δ 153.81, 138.42, 138.28, 136.79, 133.07, 132.20, 129.13, 128.91, 128.79, 123.71, 123.01, 121.79, 57.75.

Synthesis of 2,7-bis(4,4,5,5-tetramethyl-1,3,2-dioxaborolan-2-yl)spiro [fluorene-9,9'-thioxanthene] 10',10'-dioxide.

Under N_2 atmosphere, a mixture of 2,7-dibromospiro[fluorene-9,9'-thioxanthene] 10',10'-dioxide (2.69 g, 5 mmol), bis(pinacolato)diboron (3.04 g, 12 mmol), $Pd(OAc)_2$ (0.11 g, 0.5 mmol), dppf (0.55 g, 1 mmol), KOAc (1.47 g, 15 mmol) and 1.4-dioxahaxane (50 mL) was added into a 2-kneck round flask, then stirred and heated 90 ^{o}C for 6 hours. The reaction mixture was poured into water and extracted with ethyl acetate. The combined extracts were dried by anhydrous $MgSO_4$, and then the solvent was evaporated under vacuum condition. The crude product was purified by silica gel column chromatography to afford with solid (2.92 g) with 92.4% yield.

^{1}H NMR (400 Mz, $CDCl_3$) δ 8.22 (dd, J = 8.0, 1.2 Hz, 2H), 7.88 (s, 4H), 7.62 (s, 2H), 7.44 (t, J = 7.6 Hz, 2H), 7.21 (dt, J = 7.6, 1.6 Hz, 2H), 6.50 (d, J = 7.6Hz, 2H), 1.26 (s, 24H). ^{13}C NMR (100 Mz, $CDCl_3$) δ 152.83, 143.03, 139.21, 136.69, 135.23, 132.66, 131.78, 129.41, 128.20, 123.32, 120.07, 83.96, 57.61, 24.82.

Synthesis of DOSFX-SFX

Under N_2 atmosphere, a mixture of 2,7-di(1,3,2-dioxaborolan-2-yl) spiro[fluorene-9,9'-xanthene] (0.47 g，1.0 mmol), 2-bromo-3',6'-bis(octyloxy)spiro [fluorene-9,9'-xanthene] (1.77 g，2.2 mmol), $Pd(PPh_3)_4$ (0.115 g, 0.1 mmol), 2M K_2CO_3 solution (2.0 ml) and toluene/THF (20 ml, 1:1 v/v) was stirred and heated 90^{o}C for 24h. The mixture was abstracted with dichloromethane, and then the combined abstracts were dried by anhydrous $MgSO_4$. The solvent was evaporated under vacuum condition. The crude product was purified by silica gel column chromatography to afford white solid (0.98 g) with 65.1% yield. ^{1}H NMR(400 Mz, $CDCl_3$) δ 7.74-7.71(m, 6H), 7.47(dd, J = 8.0, 1.6 Hz, 2H), 7.43(dd, J = 8.0, 1.6 Hz, 2H), 7.31(t, J = 7.6 Hz, 2H), 7.29(d, J = 4.0 Hz, 4H), 7.23(dd, J = 8.0, 1.6 Hz, 2H), 7.19(dd, J = 7.6 Hz, 2H), 7.17-7.15(m, 2H), 7.09(d, J = 7.6 Hz, 2H), 6.76(dd, J = 7.6, 1.6 Hz, 2H), 6.71(d, J = 1.6 Hz, 4H), 6.44(dd, J = 8.0, 2.4 Hz, 2H), 6.33(dd, J = 8.4, 2.4 Hz, 4H), 6.27(d, J = 8.4 Hz, 4H), 3.91(t, J = 6.8 Hz, 8H), 1.78-1.71(m, 8H), 1.46-1.39(m, 8H), 1.34-1.27(m, 32H), 0.89(t, J = 2.8 Hz, 12H). ^{13}C NMR (100 MHz, $CDCl_3$) δ 158.95, 156.11, 156.06, 155.93, 152.03, 151.31, 141.25, 141.09, 139.14, 138.79, 138.44, 128.79, 128.30, 128.19, 128.11, 127.57, 127.20, 126.96, 125.52, 124.71, 123.10, 124.08, 123.41, 120.10, 119.97, 119.85, 116.82, 116.51, 111.02,

101.68, 68.12, 54.38, 53.48, 31.82, 29.34, 29.23, 29.21, 26.06, 22.66, 14.10.

Synthesis of DSFX-OSFX

Under N_2 atmosphere, a mixture of 2-bromospiro[fluorene-9,9'-xanthene] (1.23 g，3.0 mmol), 2,2'-(3',6'-bis(octyloxy)spiro[fluorene-9,9'-xanthene]-2,7-diyl)bis(4,4,5,5-tetramethyl-1,3,2-dioxaborolane) (0.84 g，1.0 mmol), $Pd(PPh_3)_4$ (0.115 g, 0.1 mmol), 2M K_2CO_3 solution (2.5 ml) and toluene/THF (30 ml, 1:1 v/v) was stirred and heated 90 ^oC for 18h. The mixture was abstracted with dichloromethane, and then the combined abstracts were dried by anhydrous $MgSO_4$. The solvent was evaporated under vacuum condition. The crude product was purified by silica gel column chromatography to afford white solid (0.93 g) with 74.4% yield. ^1H NMR (400 MHz, $CDCl_3$) δ 7.76 (d, J = 8.0 Hz, 2H), 7.74 (d, J = 8.0 Hz, 2H), 6.69 (d, J = 8.0 Hz, 2H), 7.47 (d, J = 8.0 Hz, 2H), 7.43 (d, J = 8.0 Hz, 2H), 7.33 (t, J = 7.6 Hz, 2H), 7.32 (s, 2H), 7.25 (s, 2H), 7.21 (d, J = 8.0 Hz, 4H), 7.19-7.12 (m, 8H), 6.76 (td, J = 7.6, 1.2 Hz, 2H), 6.70 (d, J = 2.0, 2H), 6.42 (d, J = 7.6, 4H), 6.32 (dd, J = 8.8, 2.0 Hz, 2H), 6.28 (d, J = 8.8 Hz, 2H), 3.91 (t, J = 6.8, 4H), 1.77-1.71 (m, 4H), 1.44-1.38 (m, 4H), 1.31-1.25 (m, 16H), 0.89 (t, J = 6.8 Hz, 6H). ^{13}C NMR (100 MHz, $CDCl_3$) δ 158.94, 156.55, 155.71, 155.31, 151.98, 151.35, 141.28, 141.08, 139.27, 138.81, 138.38, 128.92, 128.32, 128.08, 128.03, 127.76, 127.20, 126.96, 125.58, 124.81, 124.18, 124.00, 123.33, 120.04, 120.00, 119.95, 116.75, 116.38, 111.04, 101.71, 68.12, 54.31, 53.56, 31.81, 29.70, 29.33, 29.22, 26.05, 22.65, 14.09.

Synthesis of DOSFX-SFXSO

Under N_2 atmosphere, a mixture of 2-bromo-3',6'-bis(octyloxy)spiro[fluorene-9,9

'-xanthene] (1.34 g，2.0 mmol), 2,7-bis(4,4,5,5-tetramethyl-1,3,2-dioxaborolan-2-yl) spiro[fluorene-9,9'-thioxanthene] 10',10'-dioxide (0.59 g，0.93 mmol), $Pd(PPh_3)_4$ (0.107 g, 0.092 mmol), 2M K_2CO_3 solution (1.8 ml) and toluene/THF (20 ml, 1:1 v/v) was stirred and heated 90°C for 24h. The mixture was abstracted with dichloromethane, and then the combined abstracts were dried by anhydrous $MgSO_4$. The solvent was evaporated under vacuum condition. The crude product was purified by silica gel column chromatography to afford white solid (0.89 g) with 61.7% yield. ^{1}H NMR(400 Mz, $CDCl_3$) δ 8.25(dd, J = 8.0, 1.2 Hz, 2H), 7.74(t, J = 8.0 Hz, 4H), 7.72(d, J = 8.0 Hz, 2H), 7.56(s, 2H), 7.52(dd, J = 8.0, 1.6 Hz, 2H), 7.46(d, J = 8.0 Hz, 4H), 7.31(t, J = 7.6 Hz, 2H), 7.28(s, 2H), 7.24(td, J = 8.0, 1.2 Hz, 2H), 7.17(t, J = 7.6 Hz, 2H), 7.08(d, J = 7.6 Hz, 2H), 6.70(sd, J = 2.4 Hz, 4H), 6.62(d, J = 7.6 Hz, 2H), 6.33(d, J = 8.4, 2.4 Hz, 4H), 6.26(d, J = 8.4 Hz, 4H), 3.90(t, J = 6.4 Hz, 8H), 1.78-1.71(m, 8H), 1.45-1.38(m, 8H), 1.34-1.27(m, 32H), 0.88(t, J = 6.8 Hz, 12H). ^{13}C NMR(100 Mz, $CDCl_3$) δ 158.96, 156.07, 156.03, 153.08, 152.02, 141.62, 140.34, 139.96, 139.35, 139.16, 138.80, 136.78, 136.77, 132.98, 129.02, 128.83, 128.38, 127.64, 127.62, 126.80, 125.53, 124.06, 123.81, 123.45, 120.54, 120.28, 119.93, 116.45, 110.99, 101.66, 68.13, 58.18, 53.46, 31.82, 29.34, 29.23, 29.21, 26.06, 22.66, 14.11.

Synthesis of DHSFX-SFXSO

Under N_2 atmosphere, a mixture of 2-bromo-3',6'-bis(hexyloxy) spiro[fluorene-9,9'-xanthene] (1.22 g，2.0 mmol), 2,7-bis(4,4,5,5-tetramethyl-1,3,2 -dioxaborolan-2-yl)spiro[fluorene-9,9'-thioxanthene] 10',10'-dioxide (0.59 g，0.93

mmol), $Pd(PPh_3)_4$ (0.107 g, 0.092 mmol), 2M K_2CO_3 solution (1.9 ml) and toluene/THF (20 ml, 1:1 v/v) was stirred and heated 90ºC for 24h. The mixture was abstracted with dichloromethane, and then the combined abstracts were dried by anhydrous $MgSO_4$. The solvent was evaporated under vacuum condition. The crude product was purified by silica gel column chromatography to afford white solid (0.94 g) with 70.1 % yield. ^{1}H NMR(400 Mz, $CDCl_3$) δ 8.25 (dd, J = 8.0, 1.2 Hz, 2H), 7.74 (t, J = 8.0 Hz, 4H), 7.72 (d, J = 8.0 Hz, 2H), 7.57 (s, 2H), 7.52 (dd, J = 8.0, 1.6 Hz, 2H), 7.46 (t, J =7.6 Hz, 4H), 7.32 (t, J = 7.6 Hz, 2H), 7.29 (s, 2H), 7.24 (td, J = 8.0, 1.2 Hz, 2H), 7.17 (t, J = 7.6 Hz, 2H), 7.09 (d, J = 7.6 Hz, 2H), 6.70 (sd, J = 2.4 Hz, 4H), 6.63 (d, J = 8.1 Hz, 2H), 6.33 (dd, J = 8.4, 2.4 Hz, 4H), 6.27 (d, J = 8.4 Hz, 4H), 3.91 (t, J = 6.4 Hz, 8H), 1.78-1.71(m, 8H), 1.46-1.39 (m, 8H), 1.33-1.29 (m, 16H), 0.89 (t, J = 6.8 Hz, 12H). ^{13}C NMR(100 Mz, $CDCl_3$) δ 158.95, 156.07, 156.03, 153.07, 152.01, 141.62, 140.34, 139.96, 139.34, 139.16, 138.80, 136.75, 133.00, 129.02, 128.83, 128.39, 127.64, 127.62, 126.80, 125.53, 124.06, 123.82, 123.45, 120.55, 120.28, 119.94, 116.44, 110.98, 101.65, 68.12, 58.17, 53.44, 31.57, 29.18, 25.73, 22.61, 14.05.

Synthesis of DOF-SFXSO

Under N_2 atmosphere, a mixture of 2-bromo-9,9-dioctylfluorene (1.17 g，2.5 mmol), 2,7-bis(4,4,5,5-tetramethyl-1,3,2-dioxaborolan-2-yl)spiro[fluorene-9,9'-thioxanthene] (0.63 g，1.0 mmol), $Pd(PPh_3)_4$ (0.12 g, 0.1 mmol), 2M K_2CO_3 solution (1.8 ml) and toluene/THF (20 ml, 1:1 v/v) was stirred and heated 90ºC for 24h. The mixture was abstracted with dichloromethane, and then the combined abstracts were dried by

anhydrous $MgSO_4$. The solvent was evaporated under vacuum condition. The crude product was purified by silica gel column chromatography to afford white solid (0.95 g) with 82.1% yield. ^{1}H NMR(400 Mz, $CDCl_3$) δ 8.31(dd, J = 8.0, 0.8 Hz, 2H), 7.96 (d, J = 8.0 Hz, 2H), 7.81(dd, J = 8.0, 1.6 Hz, 2H), 7.77(s, 2H), 7.69-7.66 (m, 4H), 7.54-7.45 (m, 6H), 7.35-7.28 (m, 8H), 6.80 (d, J = 8.0 Hz, 2H), 1.96 (t, J = 8.0 Hz, 8H), 1.20-.1.13 (m, 8H), 1.12-1.02 (m, 32H), 0.80 (t, J = 6.8 Hz, 12H), 0.64-0.56 (m, 8H). ^{13}C NMR(100 Mz, $CDCl_3$) δ 153.22, 151.54, 151.02, 142.12, 140.81, 140.59, 140.16, 139.17, 138.75, 137.03, 132.95, 129.03, 128.47, 127.46, 127.09, 126.75, 125.75, 124.13, 123.59, 122.90, 120.91, 120.69, 120.00, 119.78, 58.36, 55.18, 40.31, 31.76, 29.99, 29.19, 23.76, 22.58, 14.07.

Synthesis of DOPhF-SFXSO.

Under N_2 atmosphere, a mixture of 2-(9,9-bis(4-(octyloxy)phenyl)fluoren-2-yl)-4,4,5,5-tetramethyl-1,3,2-dioxaboroane (1.75 g，2.5 mmol), 2,7-dibromospiro[fluorene-9,9-thiaxanthene]-S,S-dioxide (0.54 g，1.0 mmol), $Pd(PPh_3)_4$ (0.115 g, 0.1 mmol), 2M K_2CO_3 solution (2.0 ml) and toluene/THF (20 ml, 1:1 v/v) was stirred and heated 90^{o}C for 24h. The mixture was abstracted with dichloromethane, and then the combined abstracts were dried by anhydrous $MgSO_4$. The solvent was evaporated under vacuum condition. The crude product was purified by silica gel column chromatography to afford white solid (1.25 g) with 81.9% yield. ^{1}H NMR(400 Mz, $CDCl_3$) δ 8.27(d, J = 8.0 Hz, 2H), 7.85(d, J = 8.4 Hz, 2H), 7.71(t, J = 7.6 Hz, 4H), 7.65(d, J = 2.4 Hz, 4H), 7.56(s, 2H), 7.50-7.45(m, 4H), 7.35-7.23(m, 8H), 7.11(d, J = 8.8 Hz, 8H), 6.73(d, J = 8.8 Hz, 8H), 6.69(d, J =

8.4 Hz, 2H), 3.88(t, J = 6.8 Hz, 8H), 1.77-1.70(m, 8H), 1.45-1.38(m, 8H), 1.35-1.28(m, 32H), 0.88(t, J = 6.8 Hz, 12H). ^{13}C NMR (100 Mz, $CDCl_3$) δ 157.89, 153.16, 152.67, 152.24, 141.88, 140.04, 139.64, 139.58, 139.40, 139. 19, 137.69, 136.94, 132.91, 129.17, 129.04, 128.40, 127.73, 127.60, 127.33, 126.38, 126.06, 124.22, 124.18, 123.53, 120.61, 120.47, 120.24, 114.10, 67.88, 64.26, 58.28, 31.83, 29.37, 29.32, 29.25, 26.10, 22.67, 14.12.

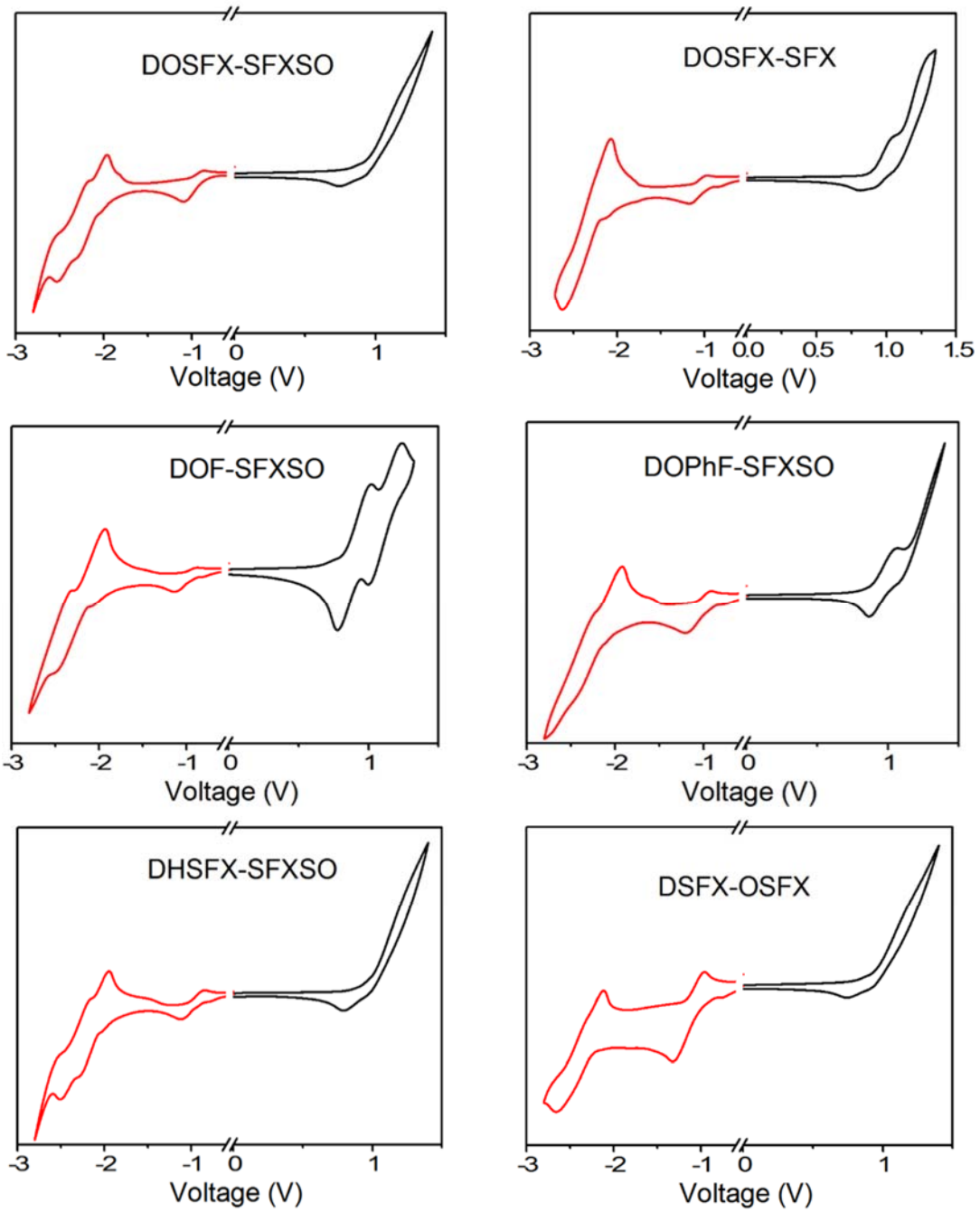

Figure S1. Cyclic voltammetry curves of terfluorene derivatives. The peak around -1.0 V is the reduction peak of water. Related to Figure 1.

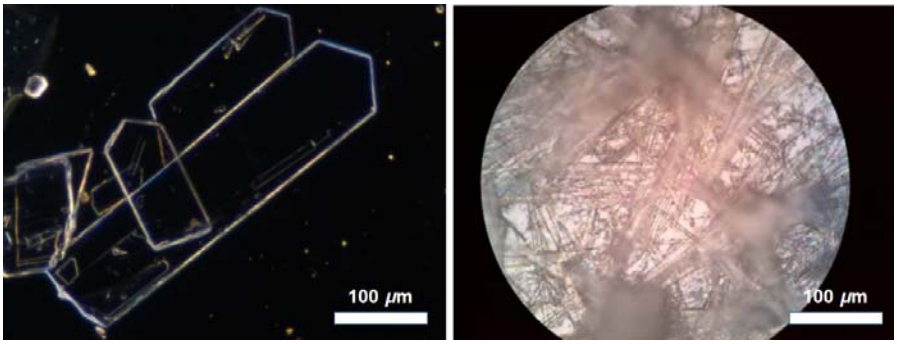

Figure S2. Optical microscope images of plate and needle crystals of DOSFX-SFXSO, the plate and needle crystals were obtained from ethanol-chloroform and methanol-dichloromethane solutions, respectively, the needle crystals were too tiny to perform single-crystal XRD. Related to Figure 2.

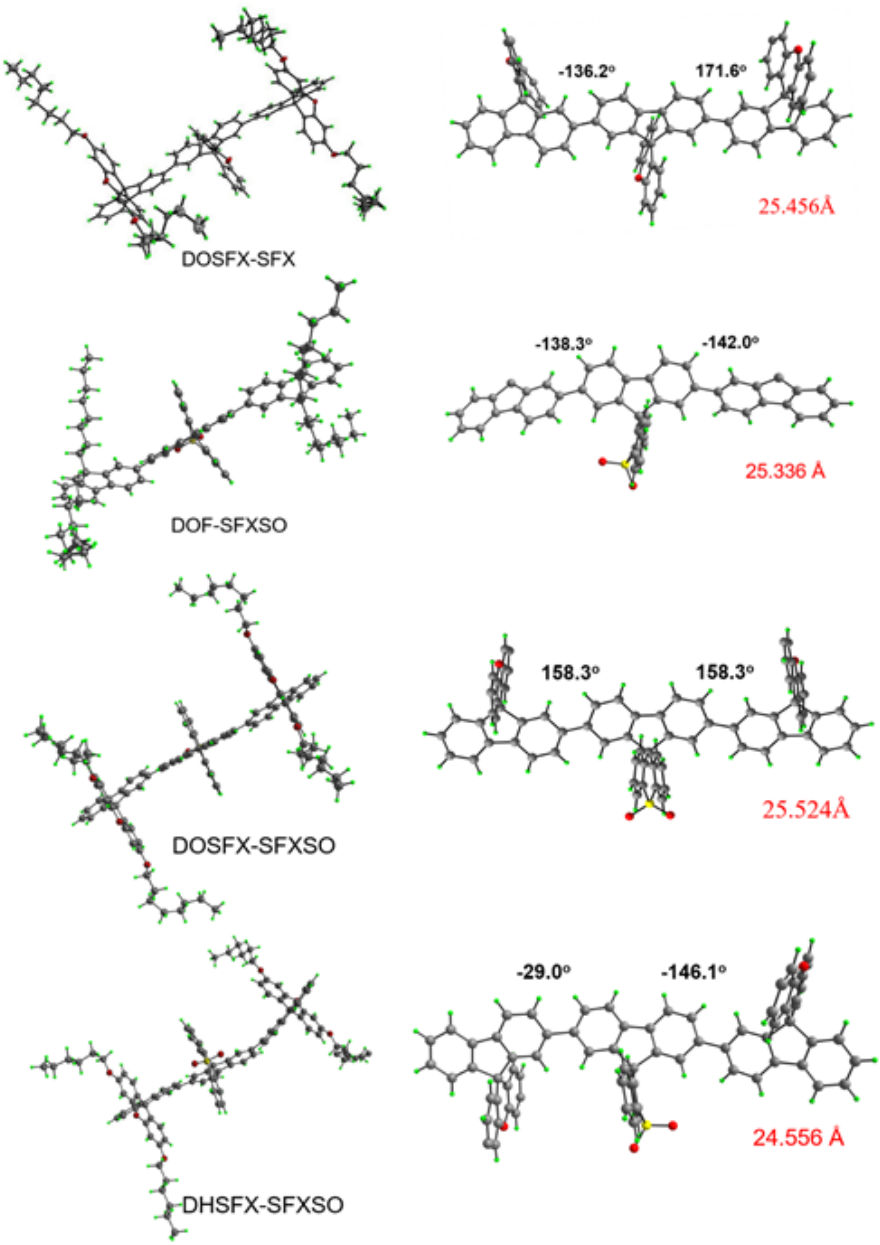

Figure S3. Crystal structures, torsional angles, and molecular length of conjugated backbone of spiro-terfluorenes. The alkyl or alkoxyl chains were omitted for clarity. Both DOSFX-SFX and DOF-SFXSO were crystallized from dichloromethane/ethanol solution, and the single crystals of DOSFX-SFXSO and DHSFX-SFXSO were obtained from chloroform/methanol solution, and contain chloroform and methanol molecules in lattice, respectively. In addition, both DOSFX-SFXSO and DHSFX-SFXSO can crystallize into needle crystals in dichloromethane/ethanol solution, while the crystals are too small to perform single X-ray diffraction. Related to Figure 2.

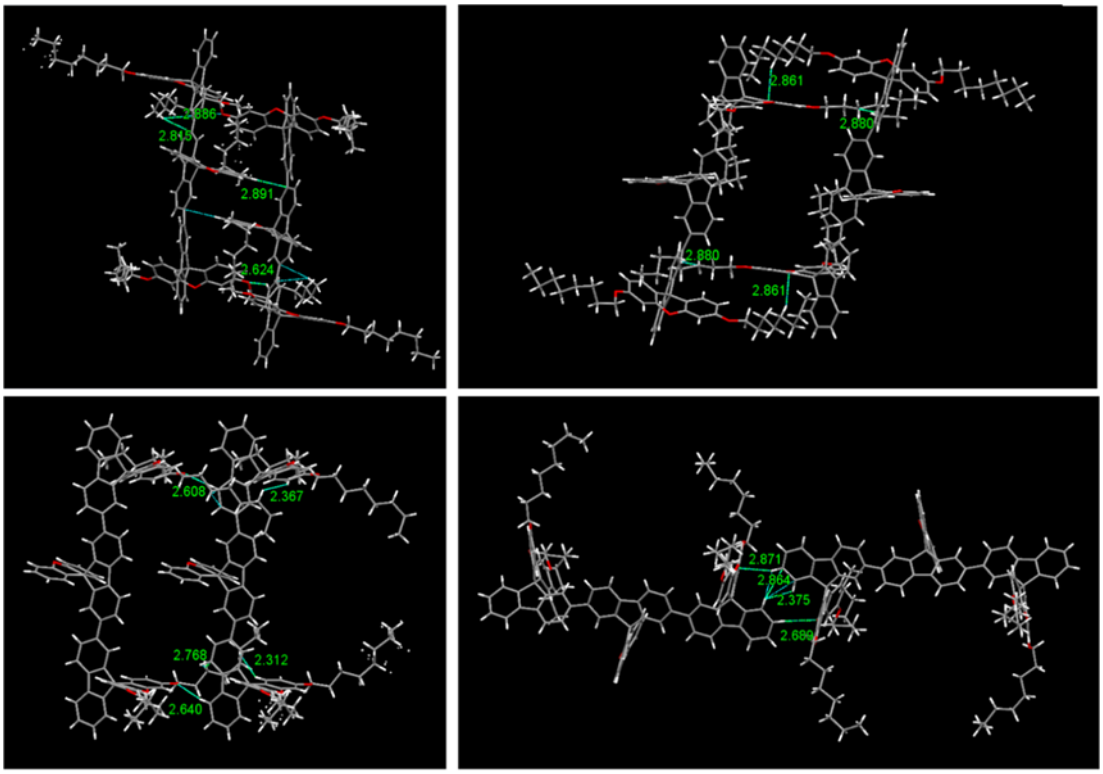

Figure S4. Intermolecular interactions between DOSFX-SFX dimers. Related to Figure 2.

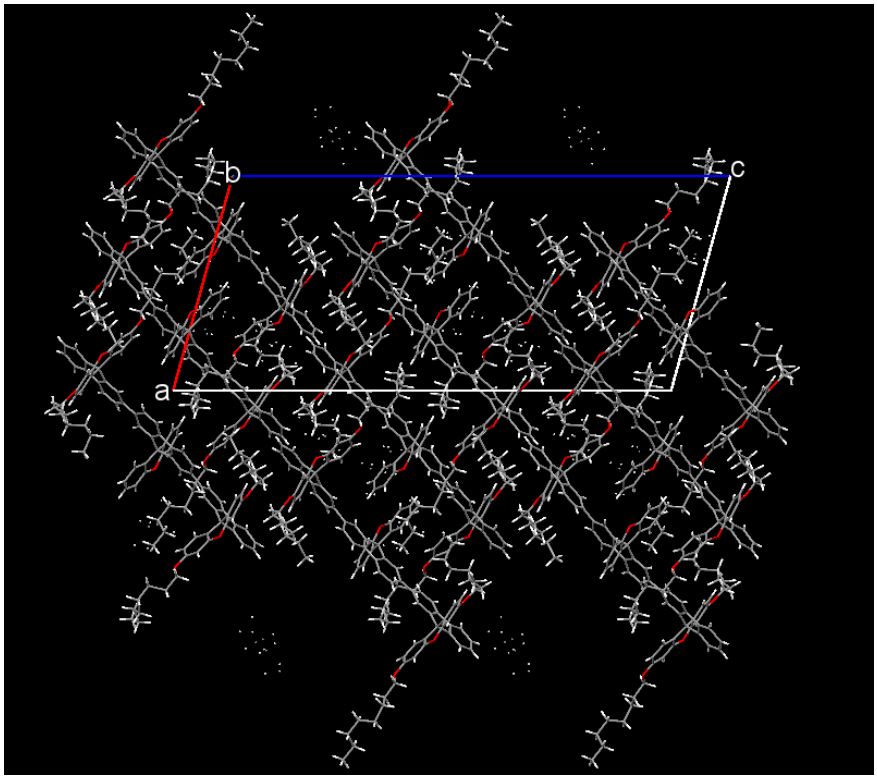

Figure S5. Packing motif of DOSFX-SFX, view from b-axis. Related to Figure 2.

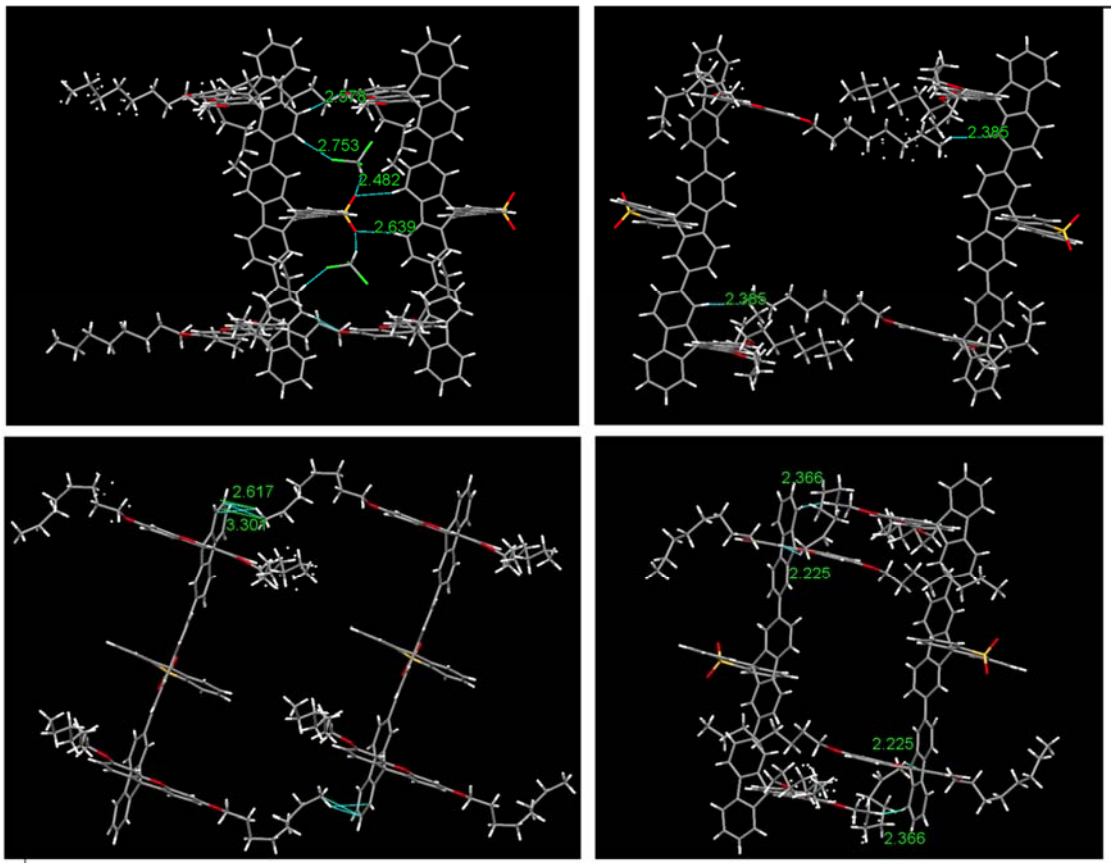

Figure S6. Intermolecular interactions in DOSFX-SFSO crystal. Related to Figure 2.

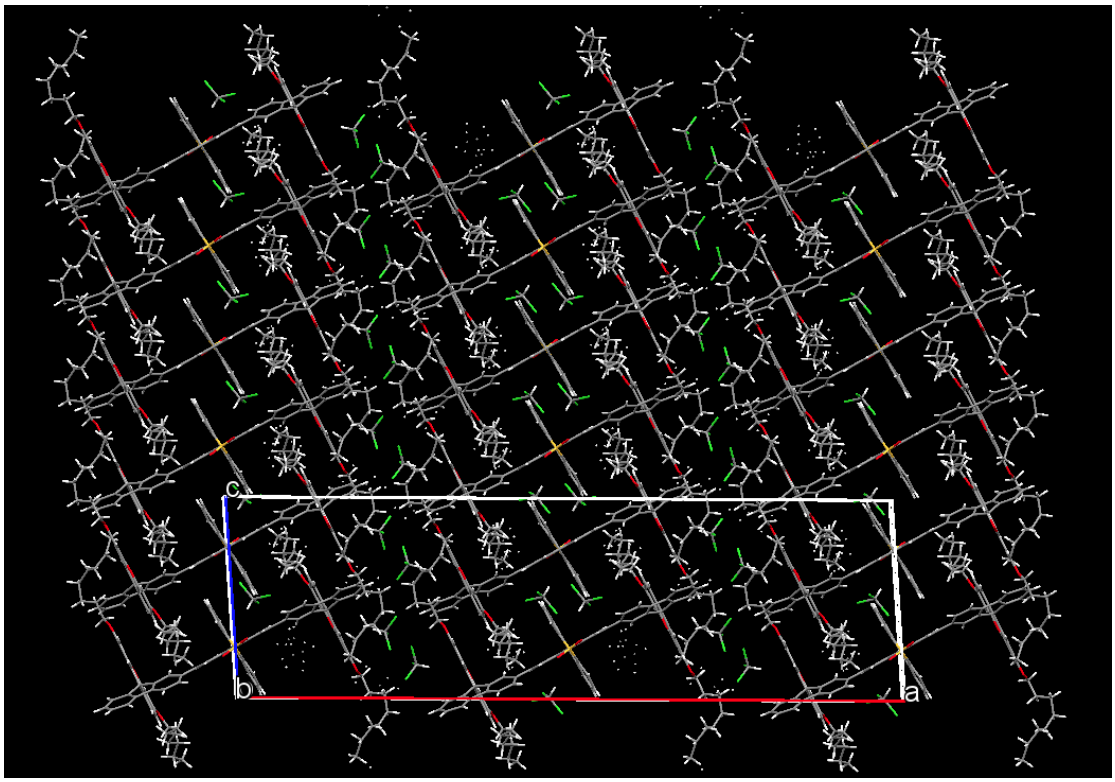

Figure S7. Packing mode of DOSFX-SFSO crystal. Related to Figure 2.

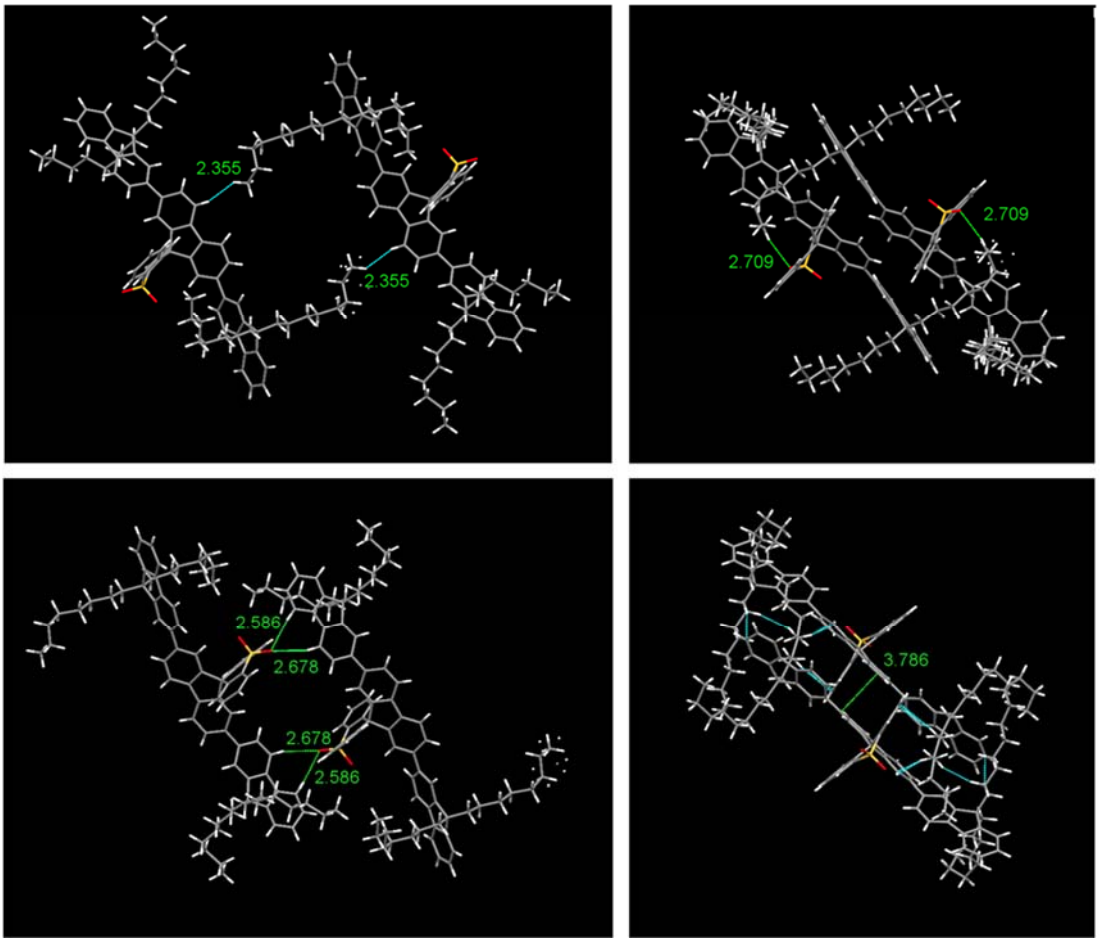

Figure S8. Intermolecular interactions in DOF-SFXSO crystal. Related to Figure 2.

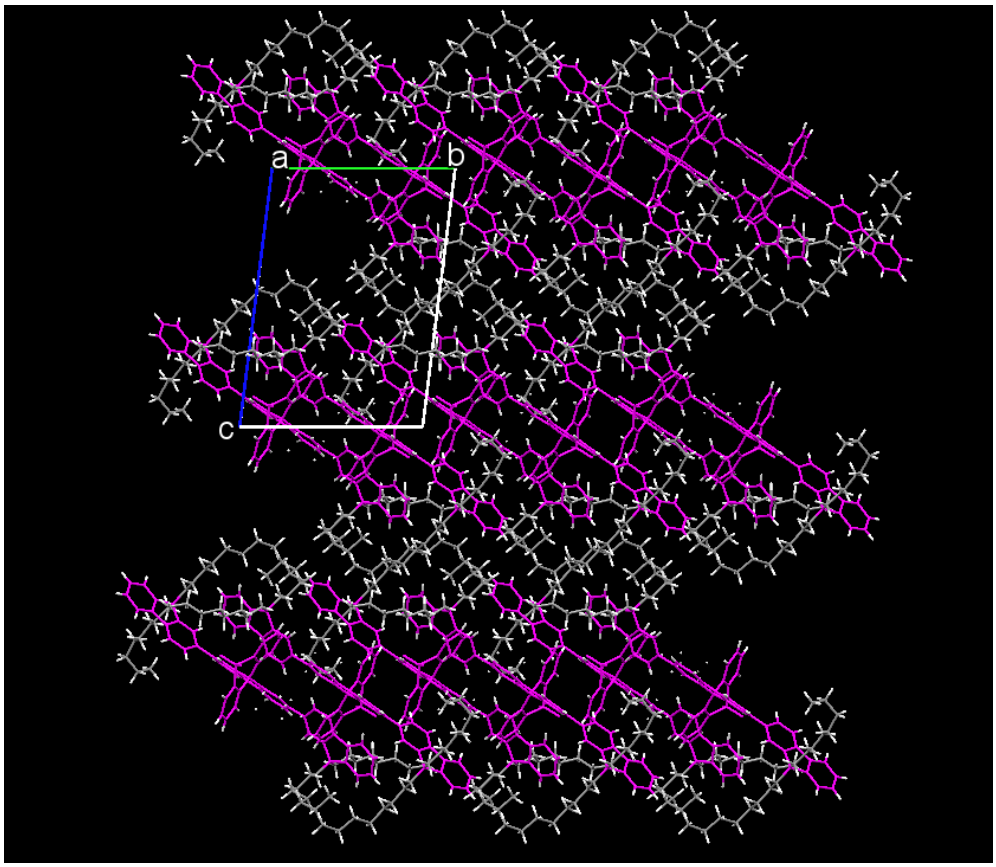

Figure S9. Packing mode of DOF-SFSO crystal view from a-axis. Related to Figure 2.

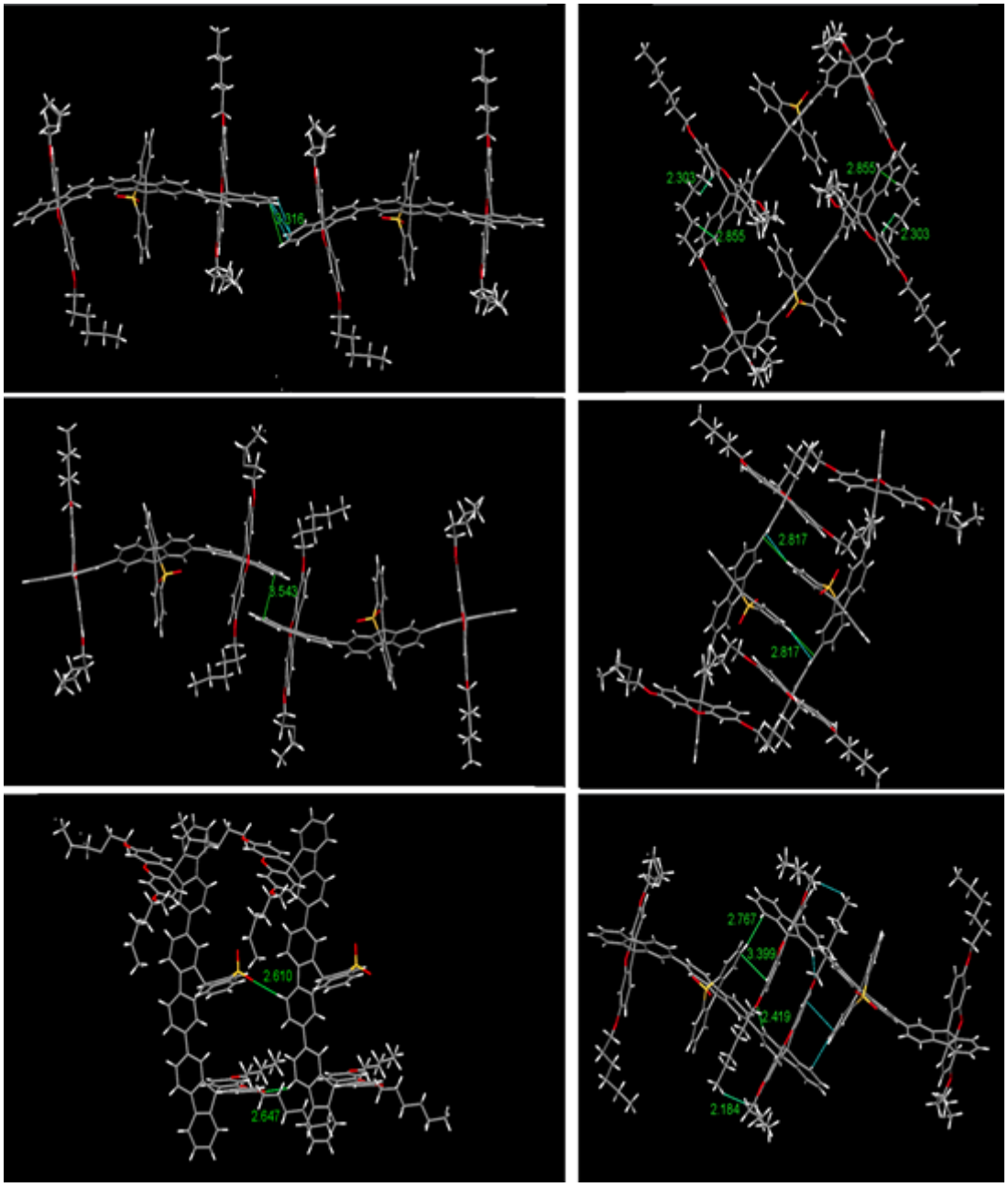

Figure S10. Intermolecular interactions between DHSFX-SFXSO dimers. Related to Figure 2.

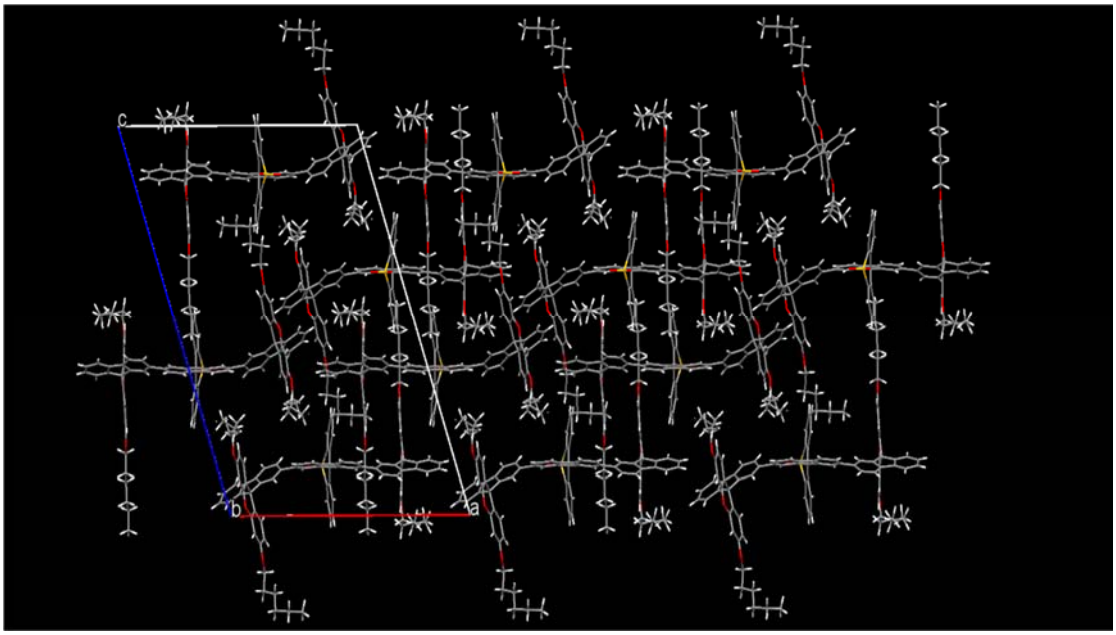

Figure S11. Packing mode of DHSFX-SFSO crystal. Related to Figure 2.

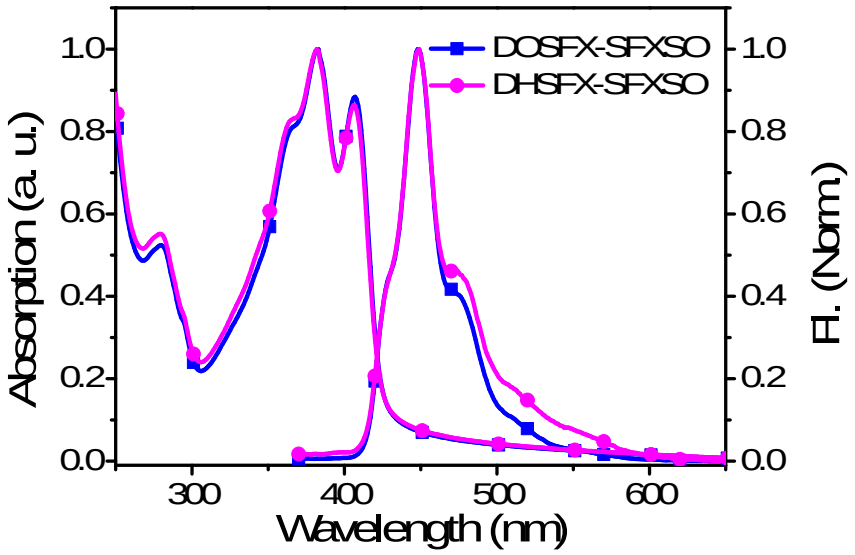

Figure S12. Absorption and PL spectra of DOSFX-SFXSO and DHSFX-SFXSO films after thermal annealing at 180 ºC. Related to Figure 1.

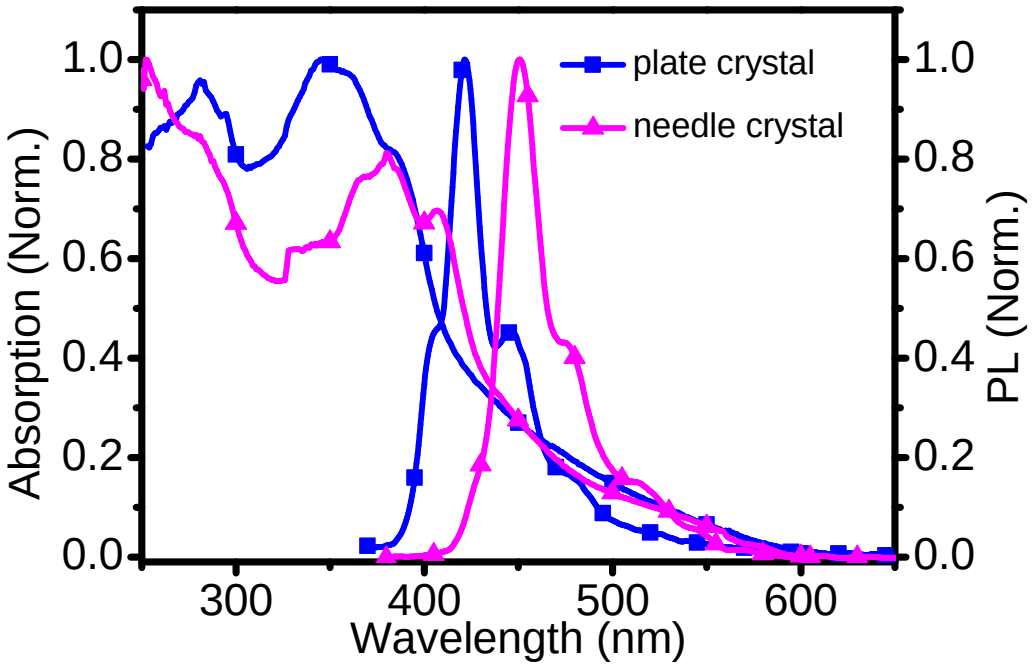

Figure S13. Absorption and PL spectra of two type single crystals of DOSFX-SFXSO. Related to Figure 2.

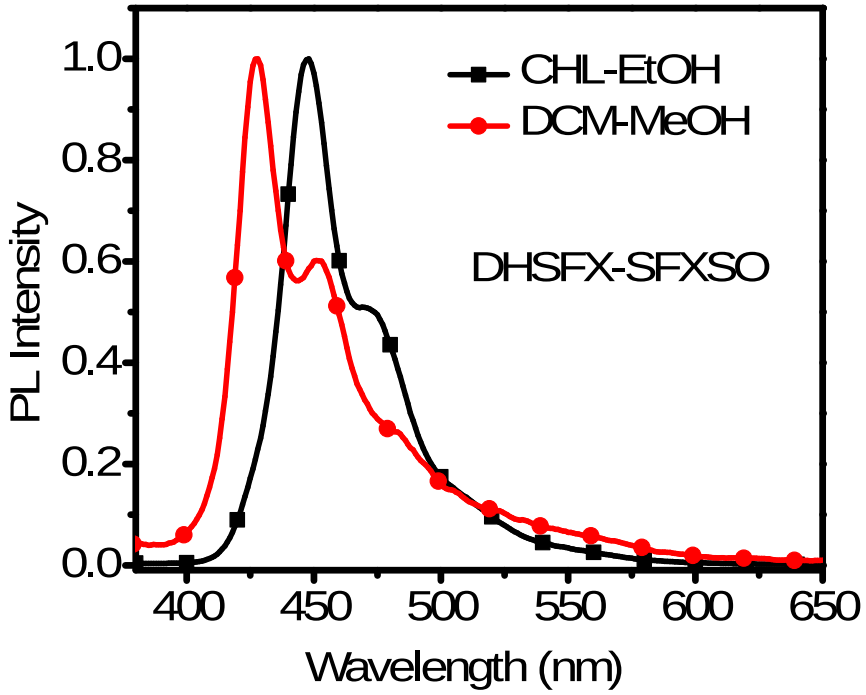

Figure S14. PL spectra of DHSFX-SFXSO microcrystals obtained from chloroform-ethanol and dichloromethane-methanol solutions, respectively. The maximum emission peaks are 427 and 447 nm, respectively. Related to Figure 2.

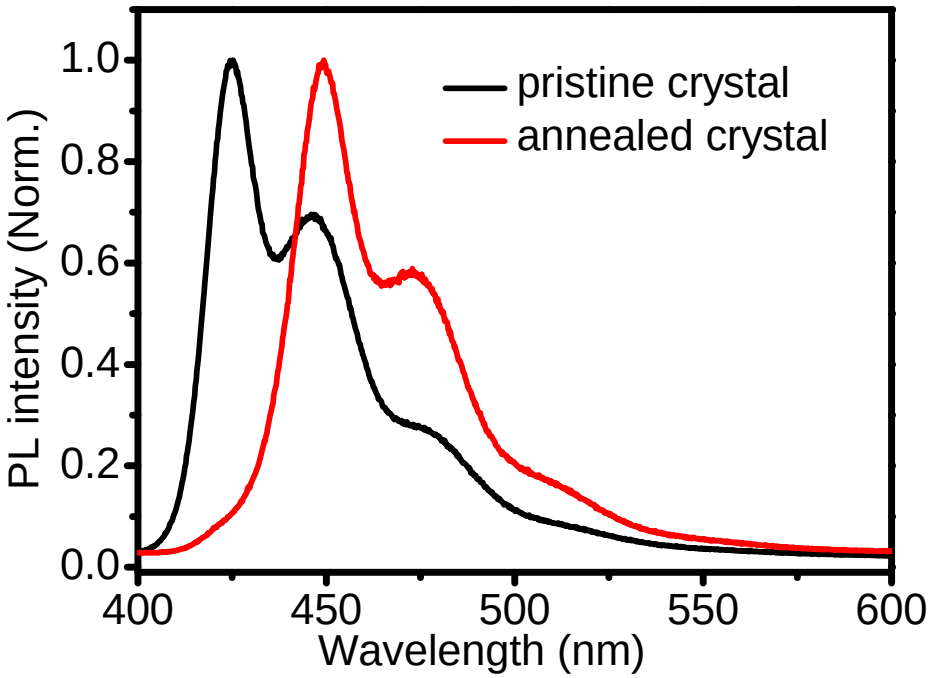

Figure S15. PL spectra of DOSFX-SFXSO pristine flake single crystal and after thermal annealing. Related to Figure 2.

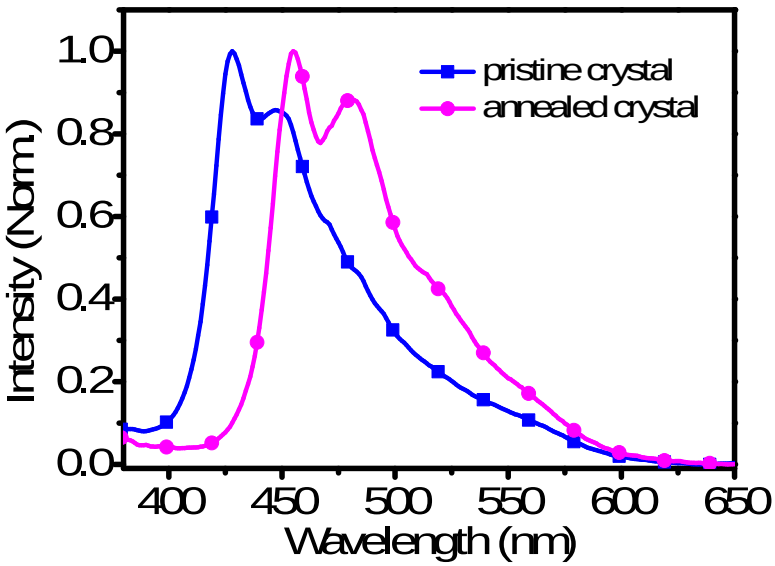

Figure S16. PL spectra of DOSFX-SFXSO pristine flake single crystal and after thermal annealing. Related to Figure 2.

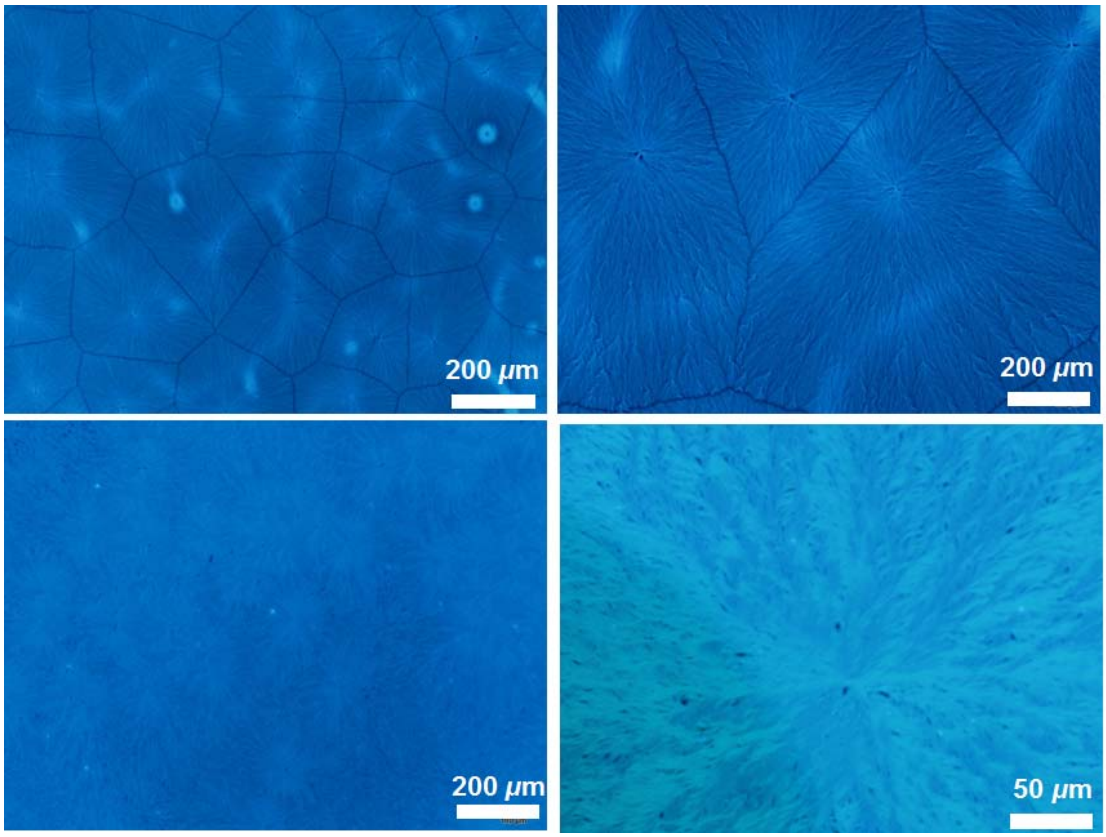

Figure S17. Fluorescence Microscope image of DOSFX-SFXSO spherulites. Related to Figure 2.

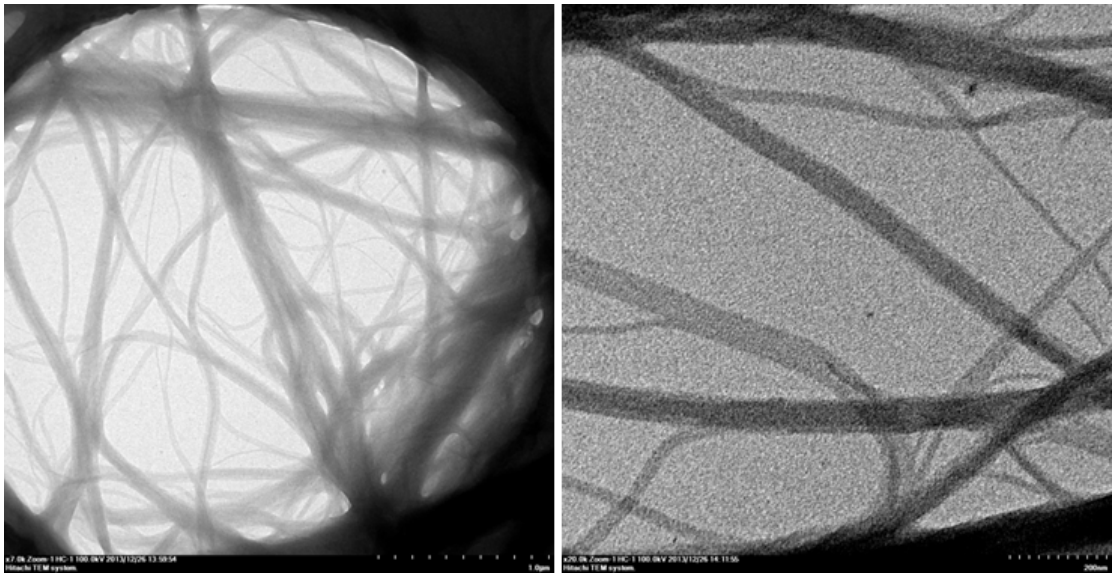

Figure S18. TEM images of DOSFX-SFXSO nanowires. Related to Figure 2.

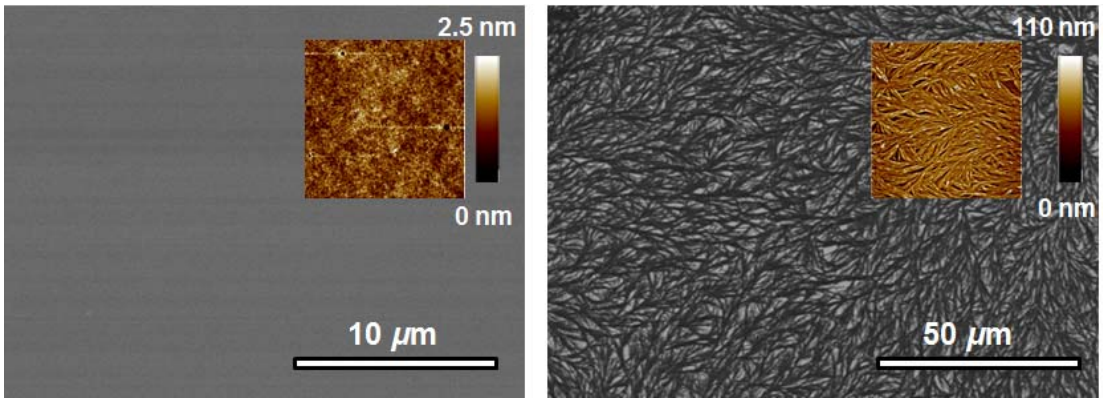

Figure S19. SEM images and its corresponding AFM images (Inset) of DOSFX-SFSO pristine films (Right) and annealed films (Left). Related to Figure 2.

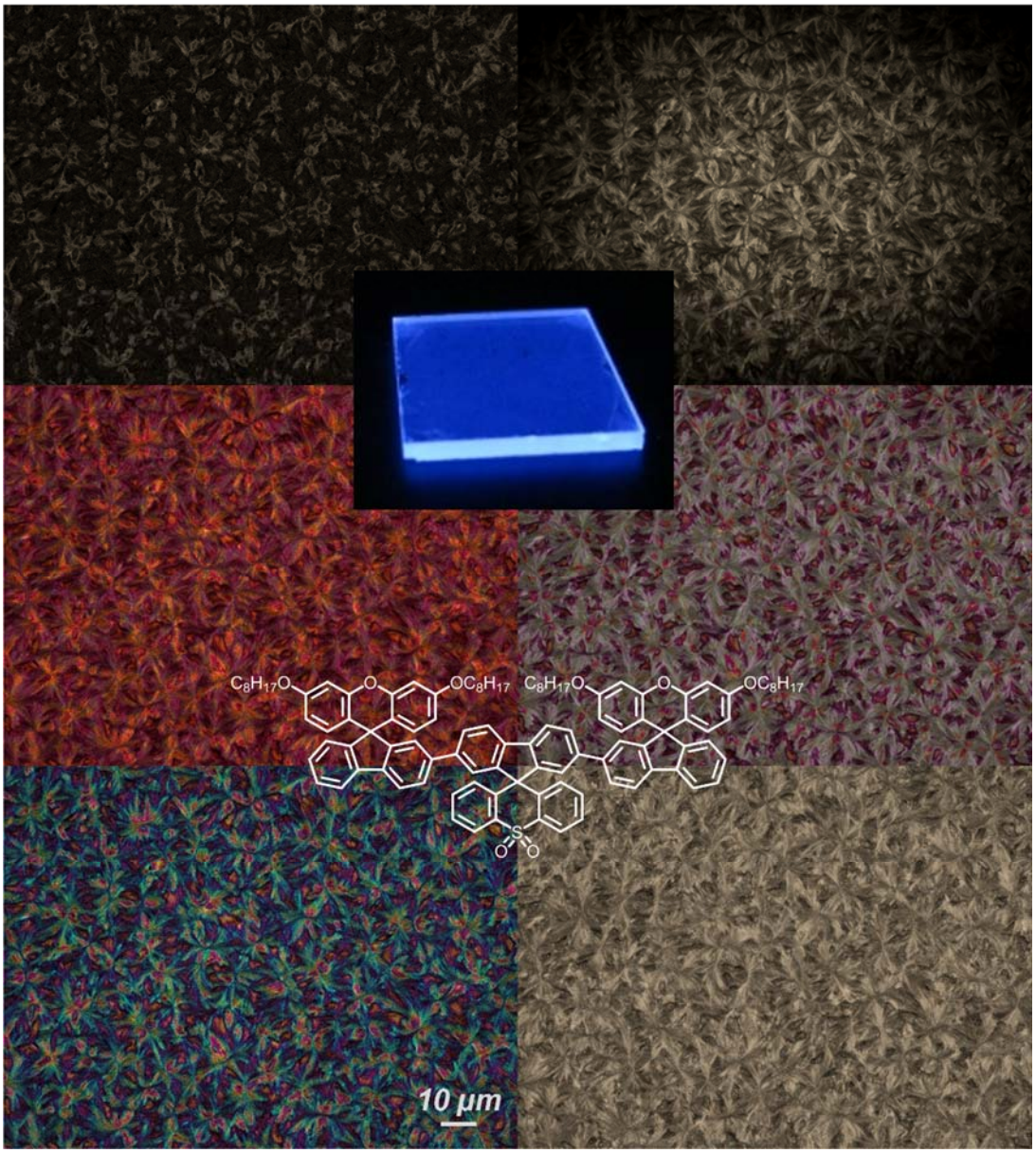

Figure S20. Polarised light images of DOSFX-SFSO annealed films. The same image but with different filters applied, revealing the texture and different regions within the crystal. Related to Figure 2.

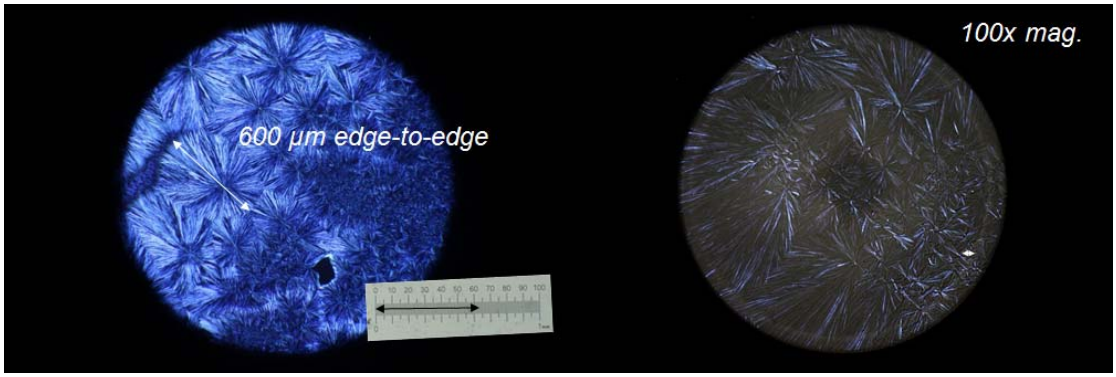

Figure S21. Cross-polarised light microscope image of DOSFX-SFX and DOSFX-SFSO annealed films. Related to Figure 2.

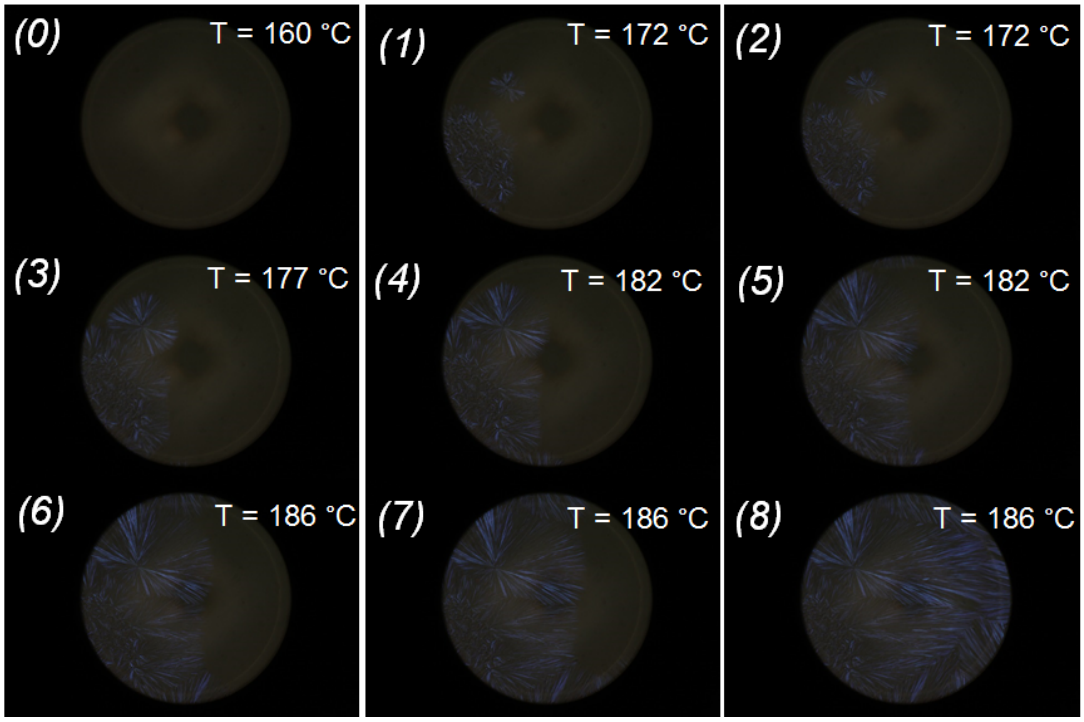

Figure S22. Polarised light microscope image of DOSFX-SFSO annealed films under thermal annealing at various temperatures. Related to Figure 2.

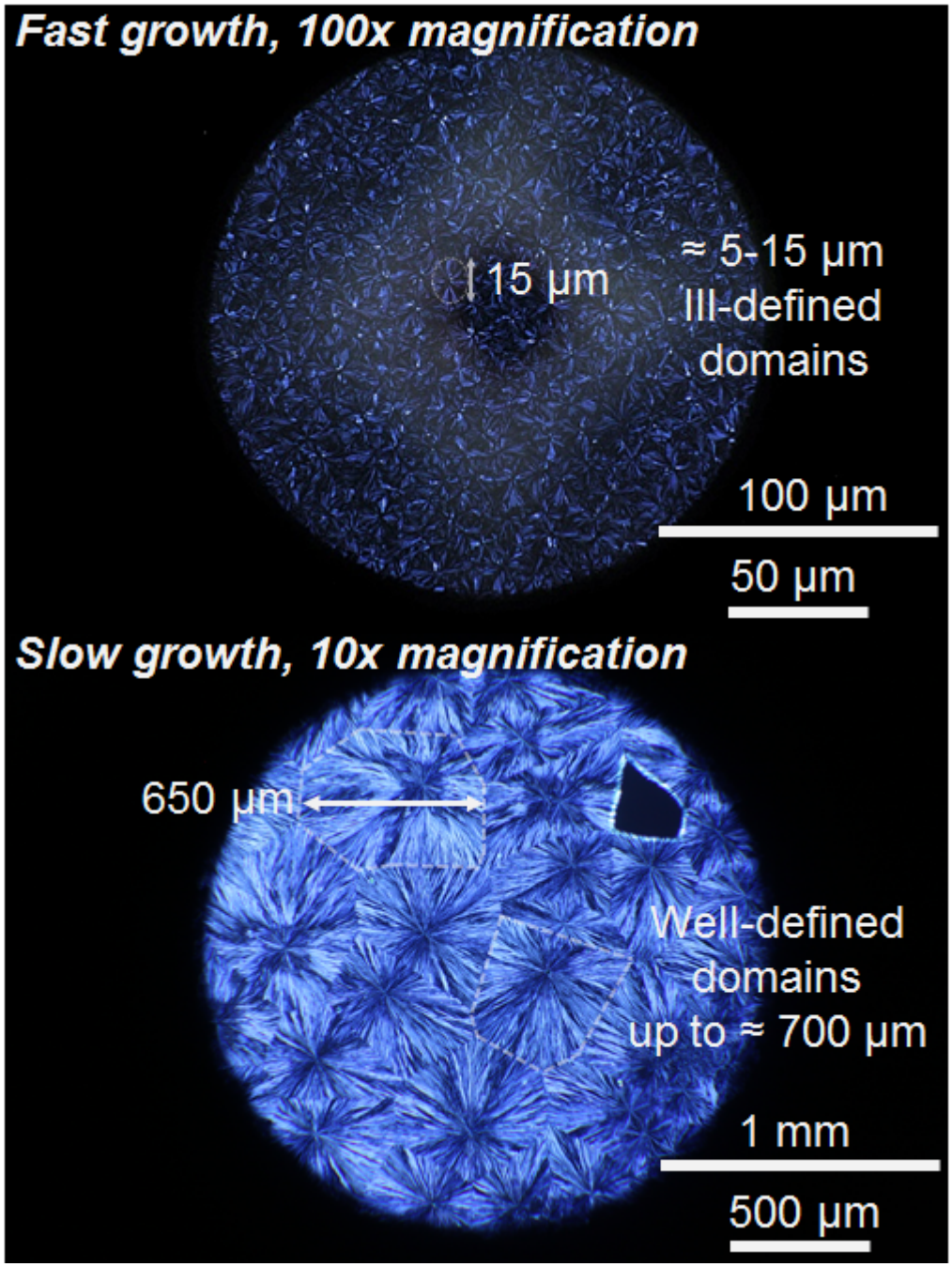

Figure S23. Polarised light microscope image of DOSFX-SFSO annealed films at different crystalline growth ratio. Related to Figure 2.

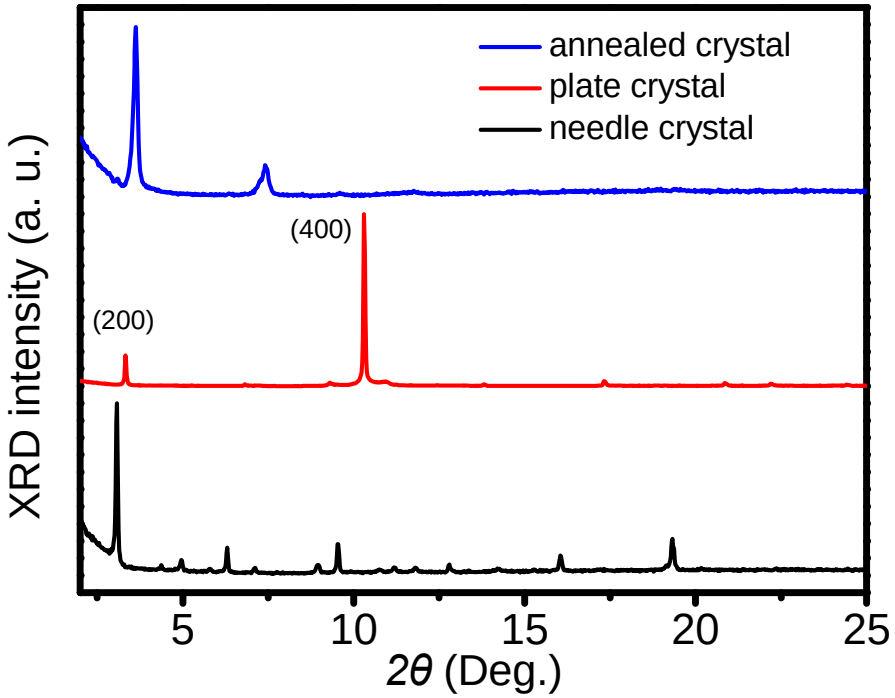

Figure S24. XRD data of DOSFX-SFSO annealed films, plate and needle single crystal. Related to Figure 2.

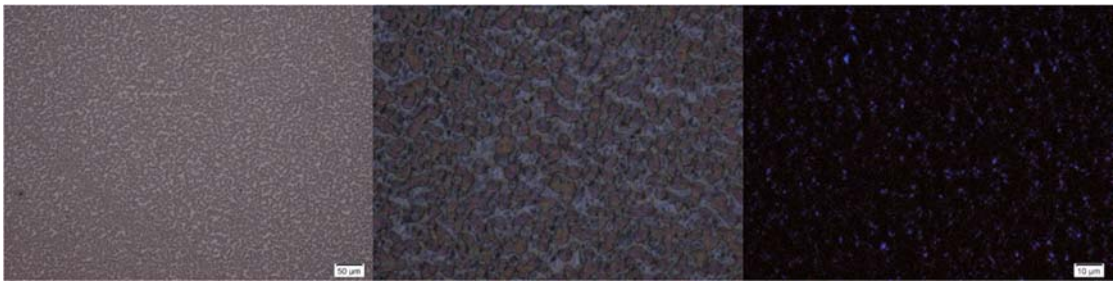

Figure S25. Microscope images of DSFX-OSFX annealed films under non-polarised light, polarized and cross-polarised light. Related to Figure 3.

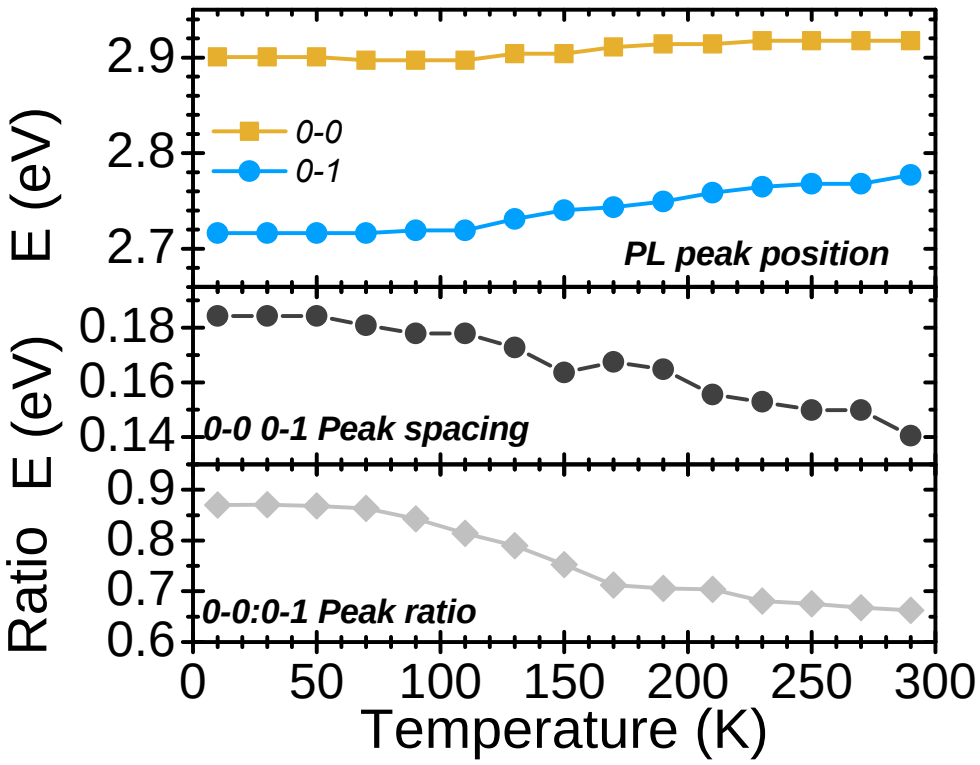

Figure S26. 0-0 - 0-1 peak intensity ratio of DOSFX-SFXSO annealed films upon decreasing temperature from 290 to 10 K. Related to Figure 3.

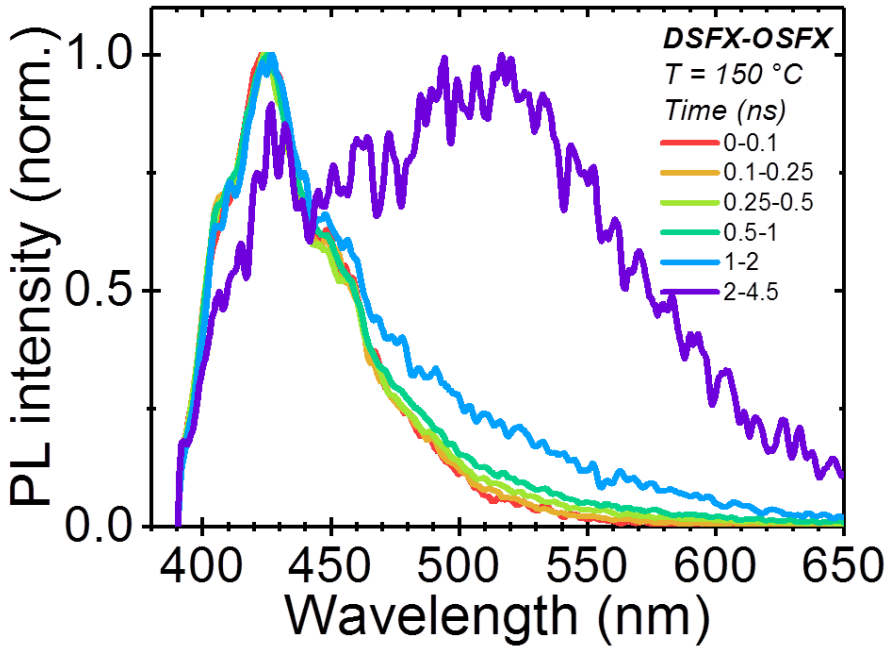

Figure S27. The PL spectra of DSFX-OSFX annealed (crystalline) film excited at 365 nm using a frequency-doubled, mode locked Ti:sapphire laser and measured at 0 ns~4.5 ns following excitation. Related to Figure 3.

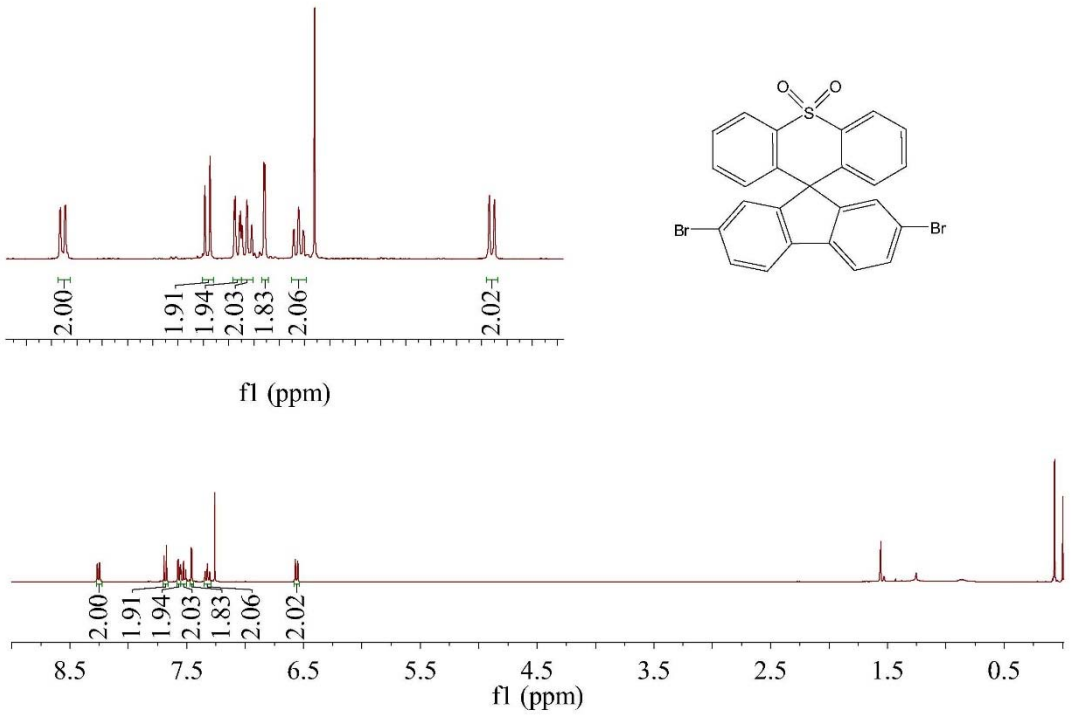

Figure S28. ^{1}H NMR spectrum of 2,7-dibromospiro[fluorene-9,9'-thioxanthene] 10',10'-dioxide. Related to Figure 1.

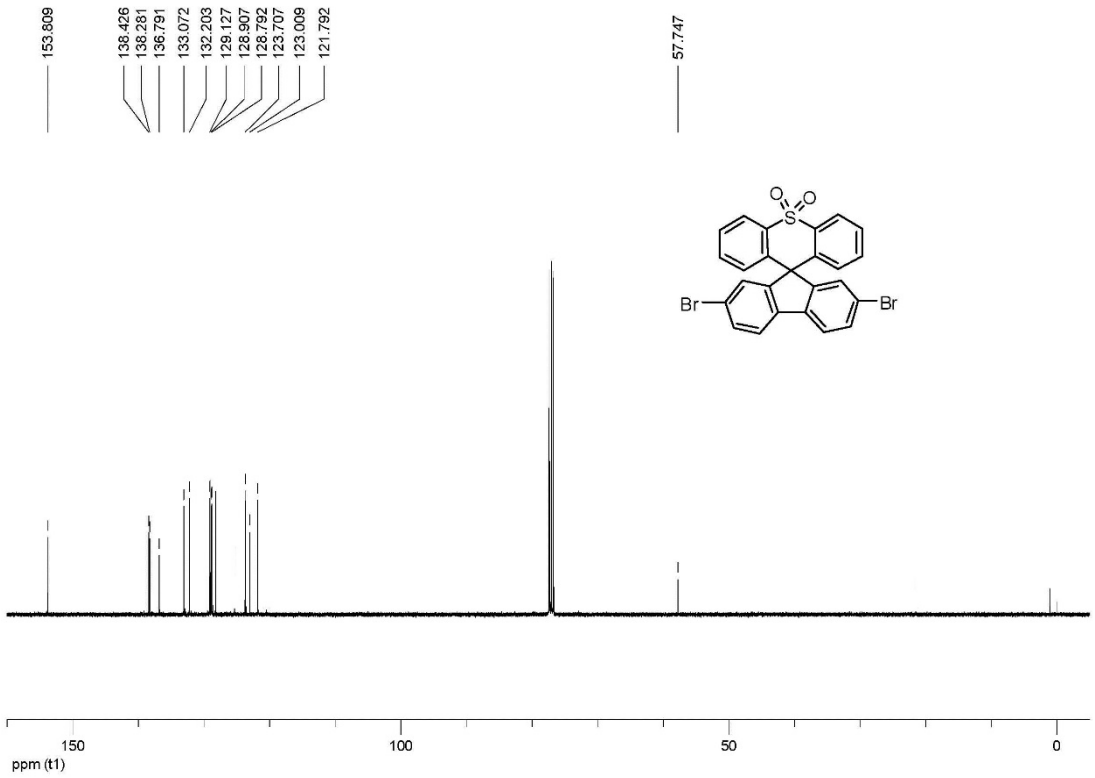

Figure S29. ^{13}C NMR spectrum of 2,7-dibromospiro[fluorene-9,9'-thioxanthene] 10',10'-dioxide. Related to Figure 1.

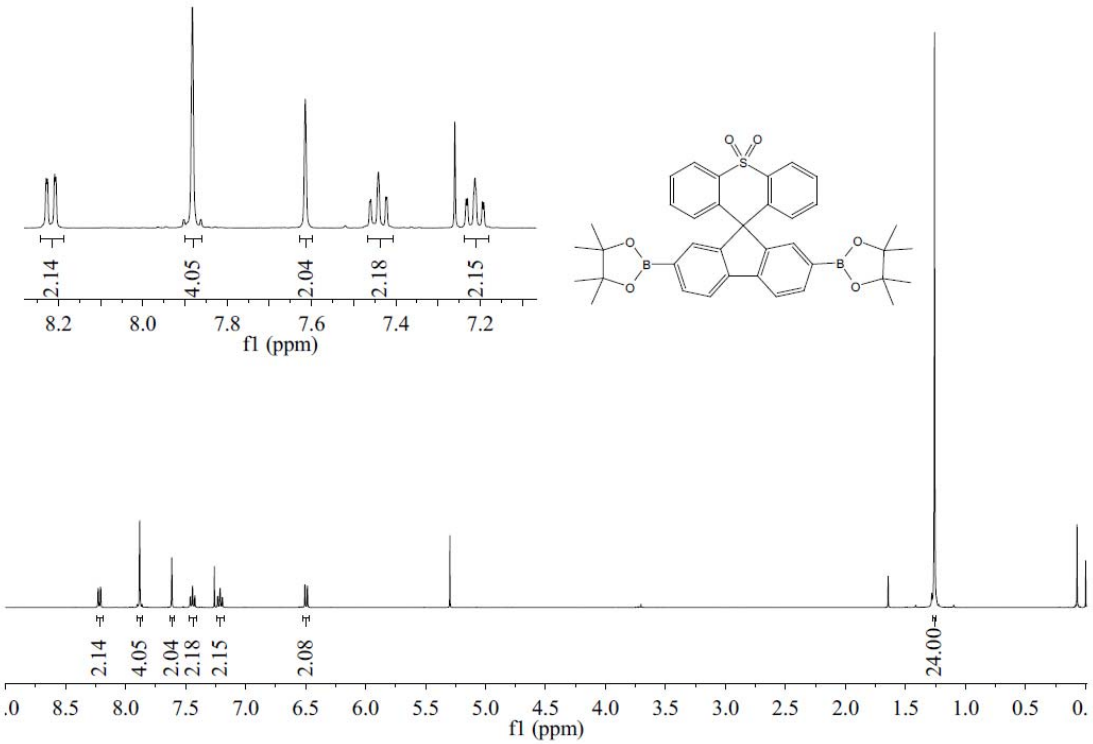

Figure S30. ^{1}H NMR spectrum of 2,7-bis(4,4,5,5-tetramethyl-1,3,2-dioxaborolan-2-yl)spiro[fluorene-9,9'-thioxanthene] 10',10'-dioxide. Related to Figure 1.

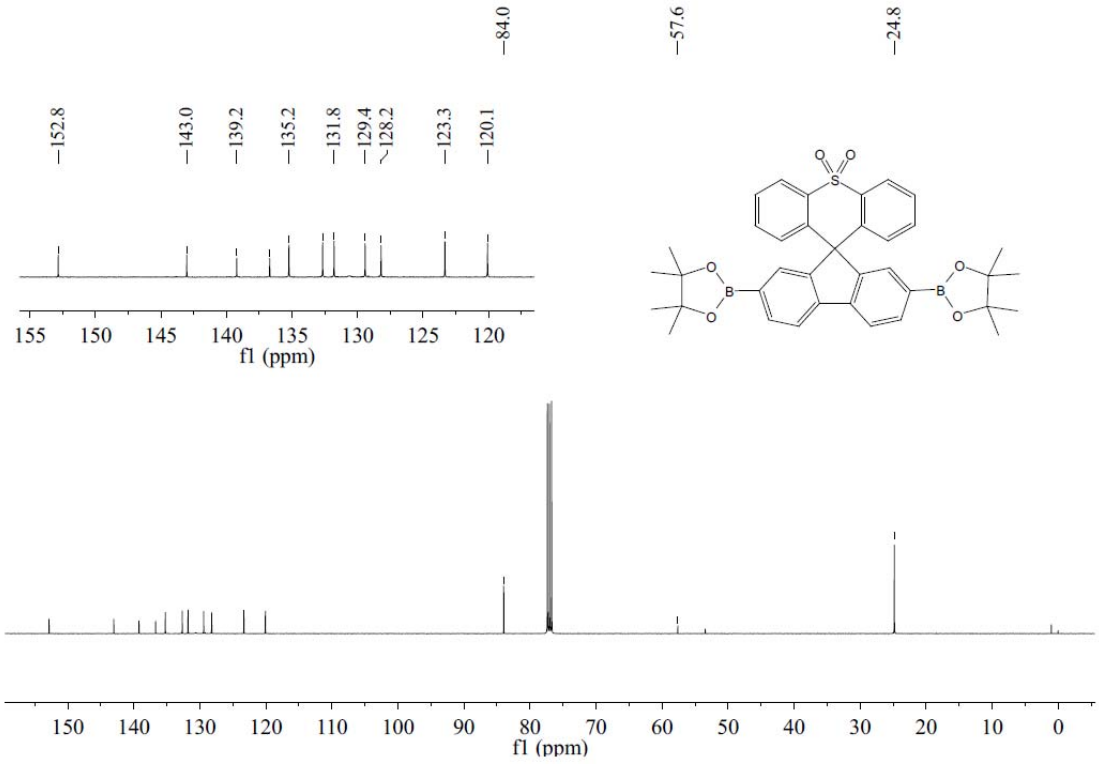

Figure S31. ^{13}C NMR spectrum of 2,7-bis(4,4,5,5-tetramethyl-1,3,2-dioxaborolan

-2-yl)spiro[fluorene-9,9'-thioxanthene] 10',10'-dioxide. Related to Figure 1.

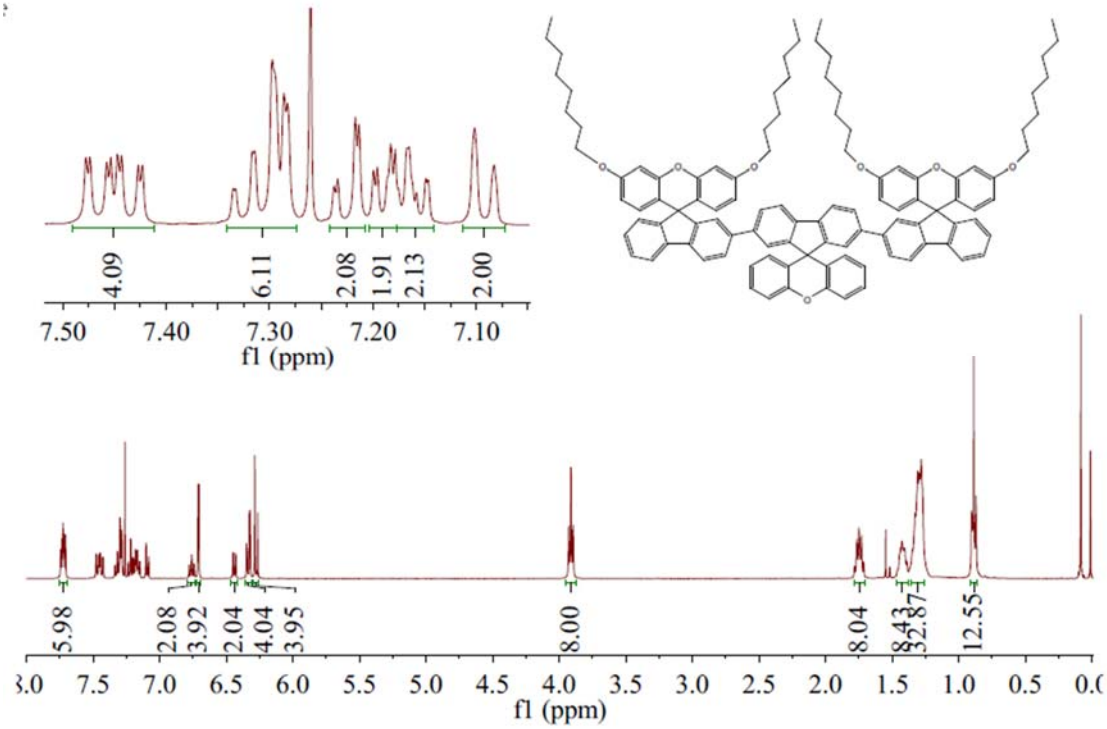

Figure S32. ^{1}H NMR spectrum of DOSFX-SFX. Related to Figure 1.

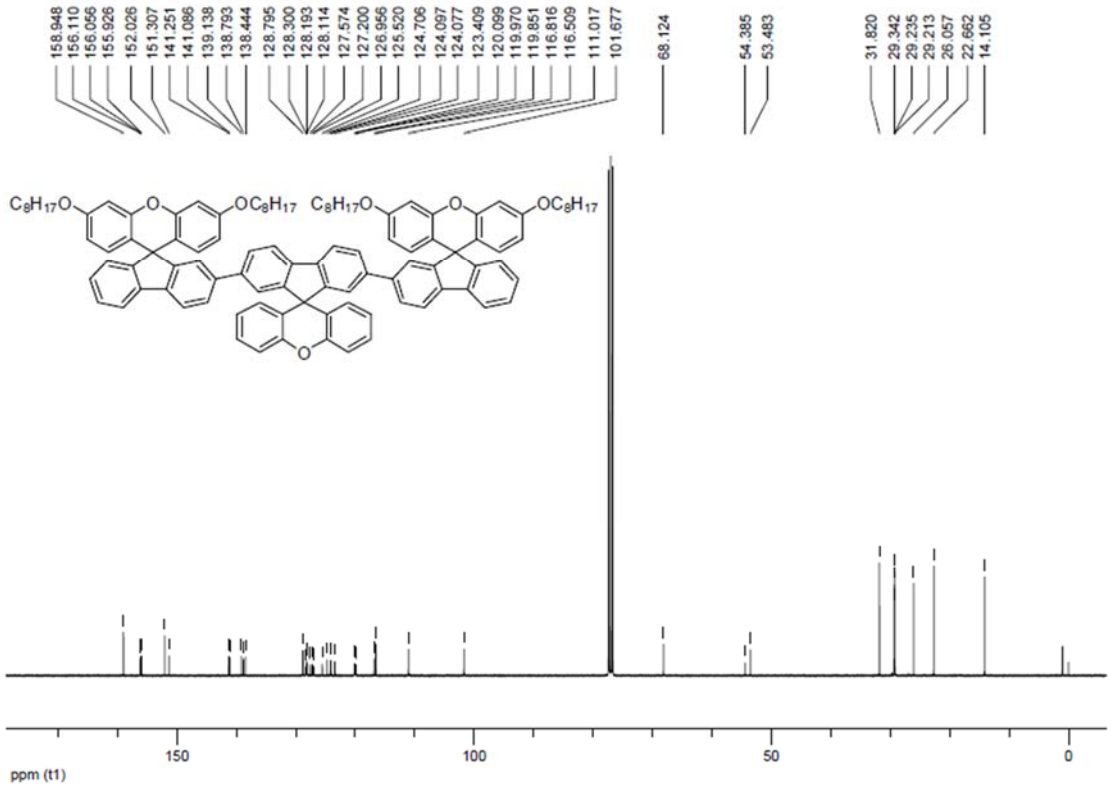

Figure S33. ^{13}C NMR spectrum of DOSFX-SFX. Related to Figure 1.

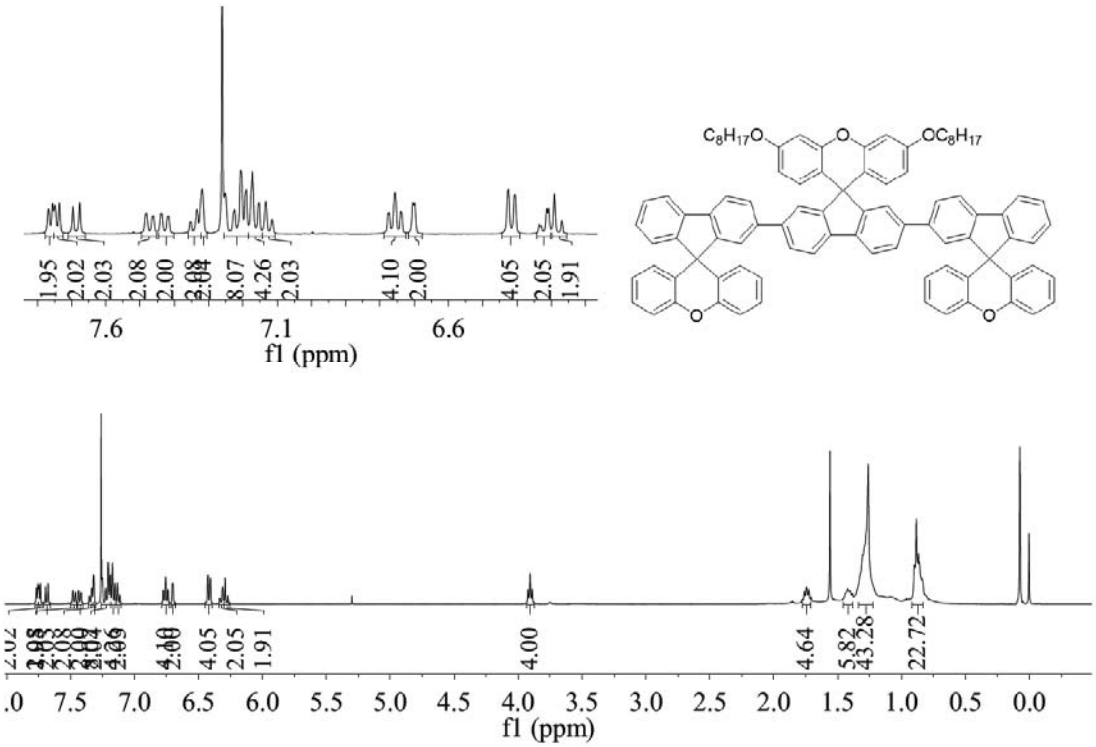

Figure S34. ^{1}H NMR spectrum of DSFX-OSFX. Related to Figure 1.

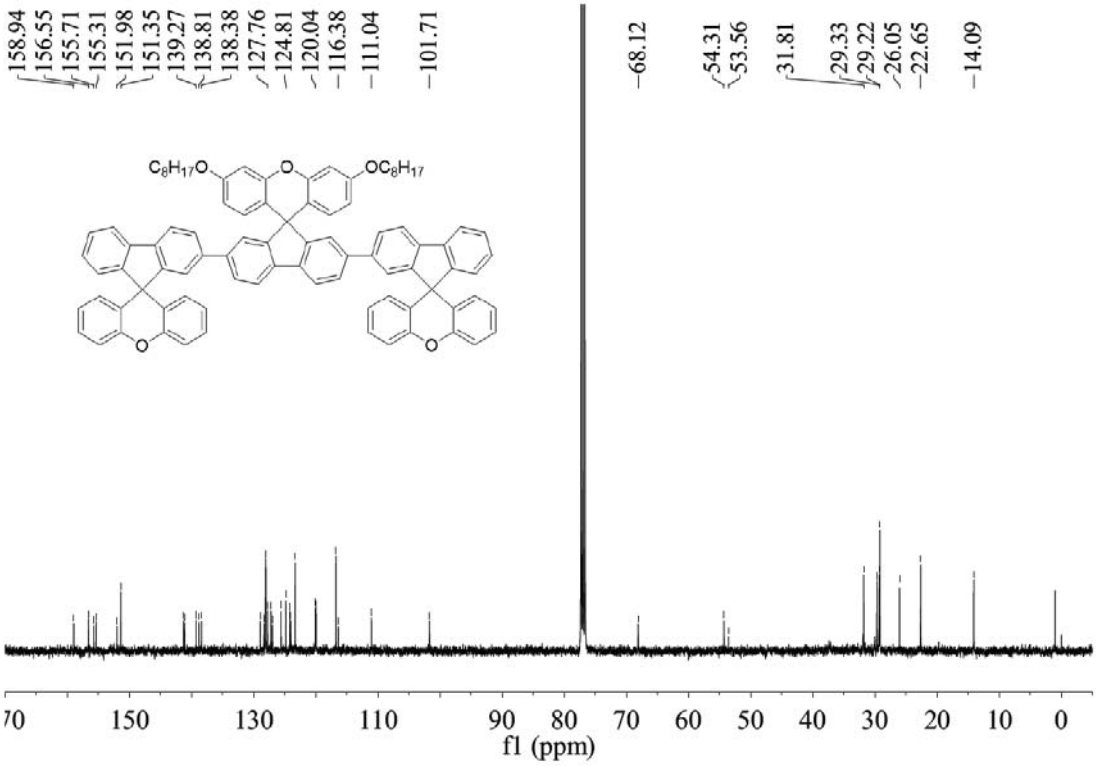

Figure S35. ^{13}C NMR spectrum of DSFX-OSFX. Related to Figure 1.

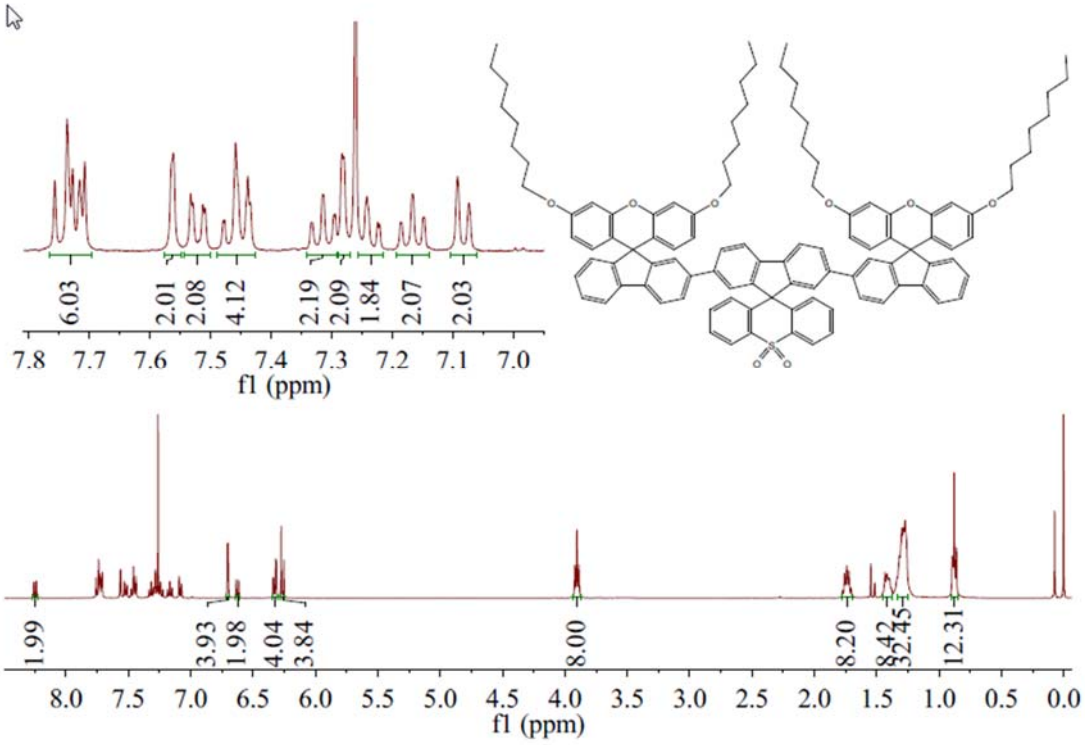

Figure S36. ^{1}H NMR spectrum of DOSFX-SFXSO. Related to Figure 1.

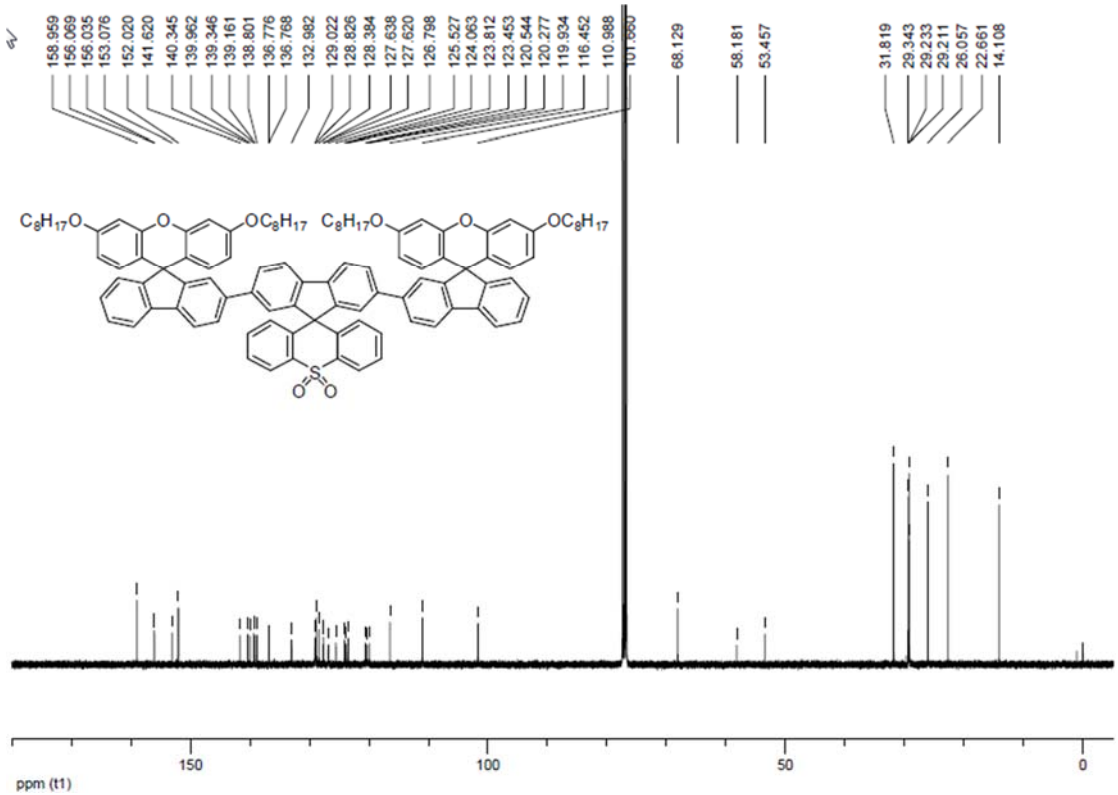

Figure S37. ^{13}C NMR spectrum of DOSFX-SFXSO. Related to Figure 1.

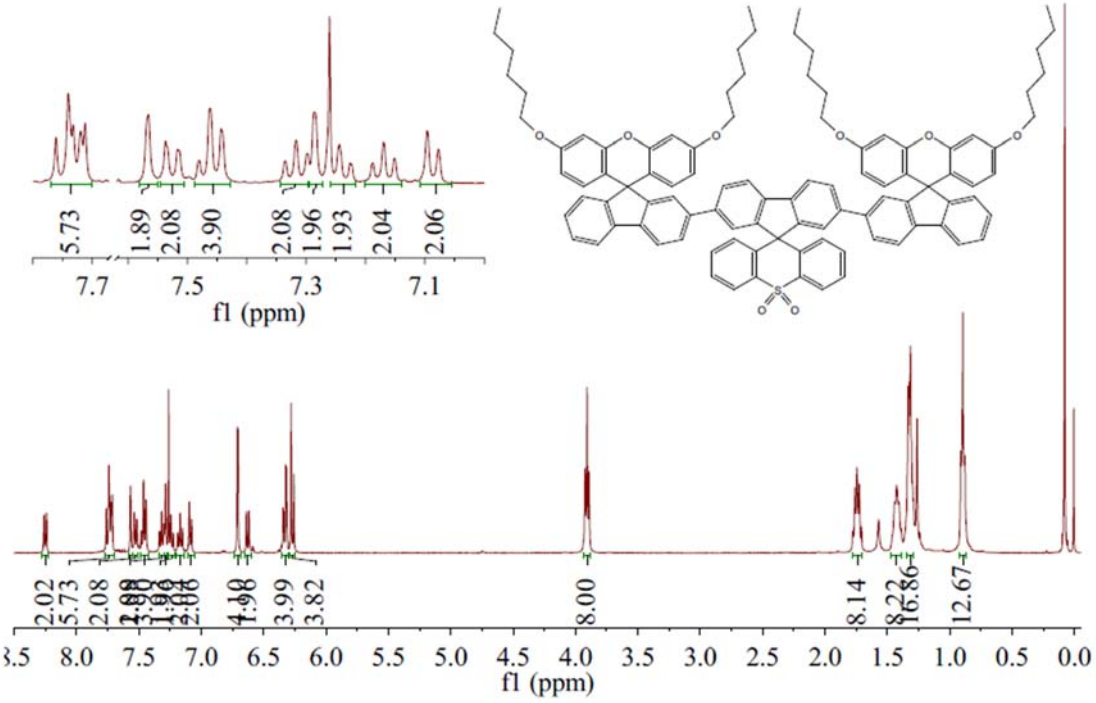

Figure S38. ^{1}H NMR spectrum of DHSFX-SFXSO. Related to Figure 1.

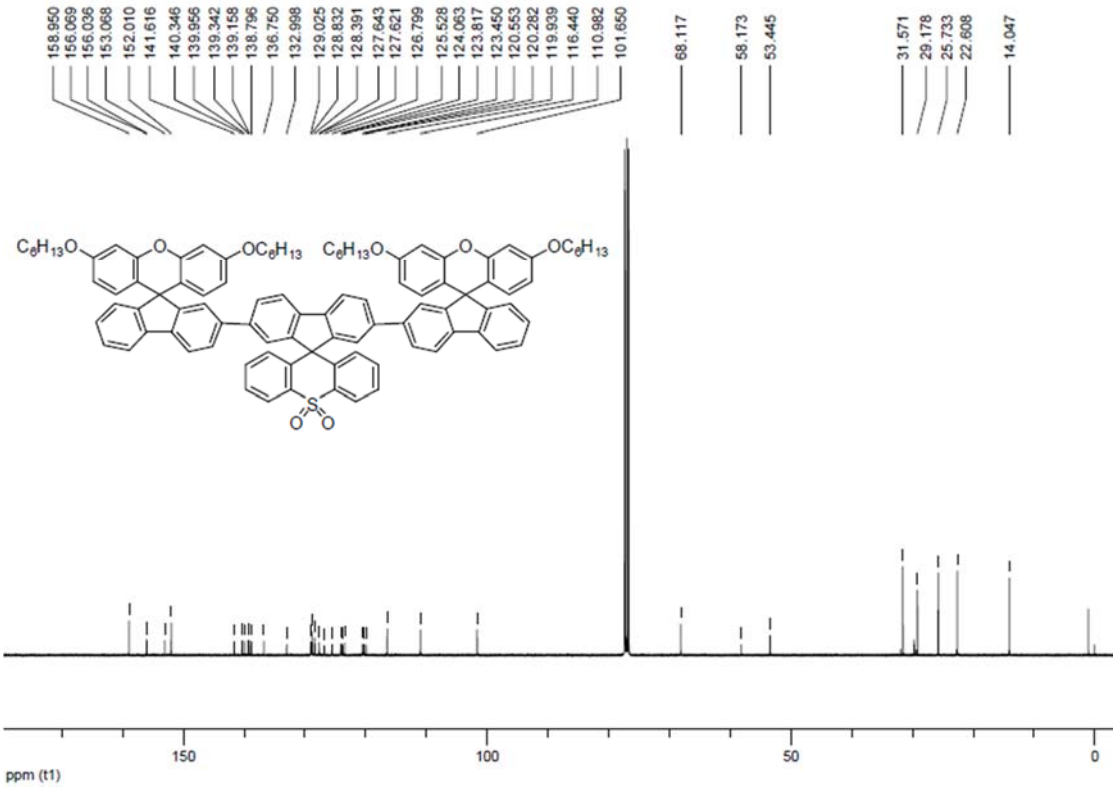

Figure S39. ^{13}C NMR spectrum of DHSFX-SFXSO. Related to Figure 1.

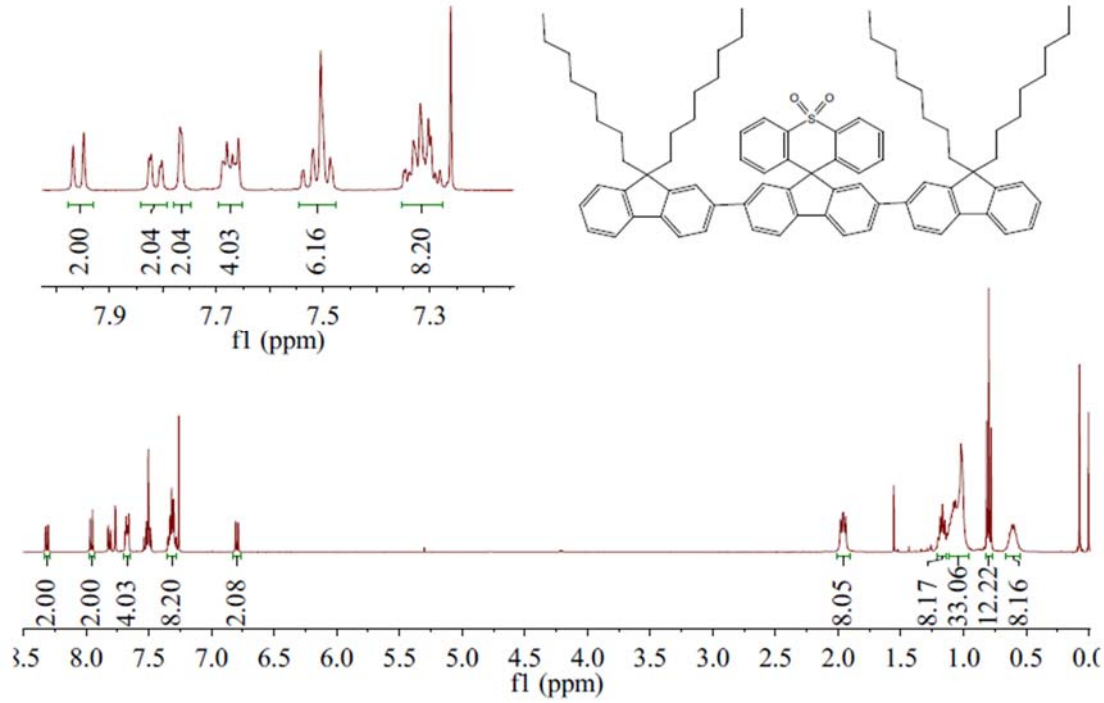

Figure S40. ^{1}H NMR spectrum of DOF-SFXSO. Related to Figure 1.

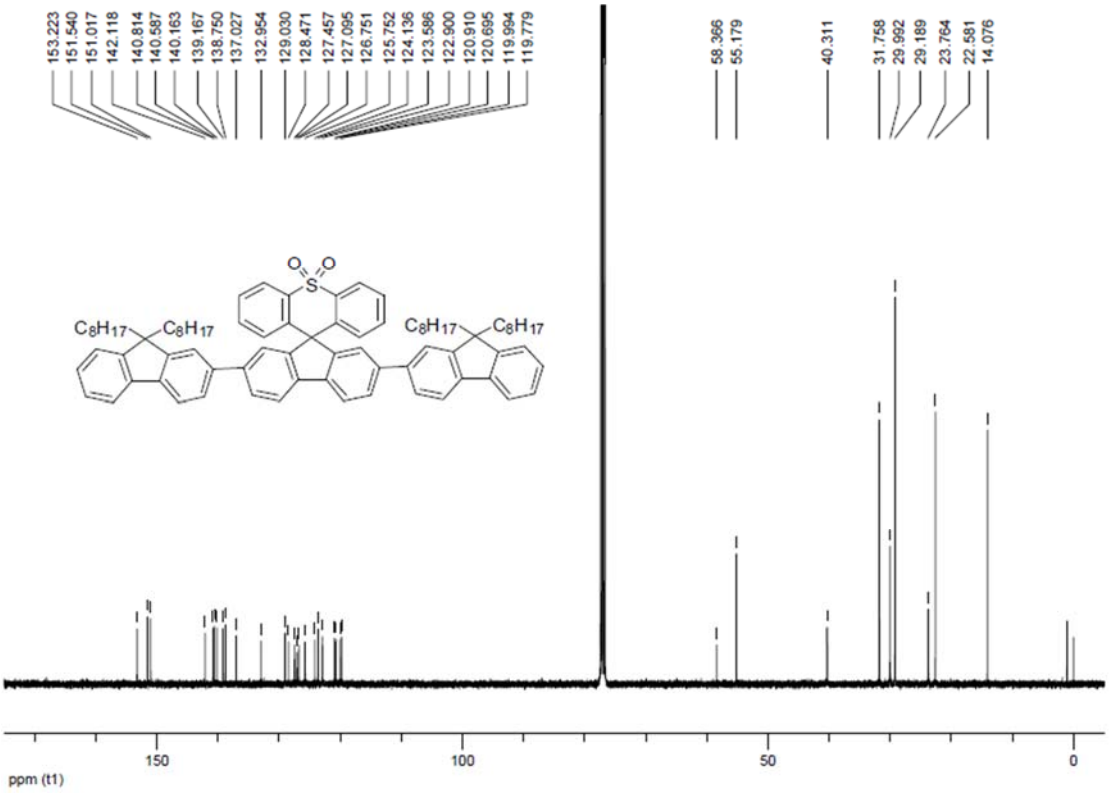

Figure S41. ^{13}C NMR spectrum of DOF-SFXSO. Related to Figure 1.

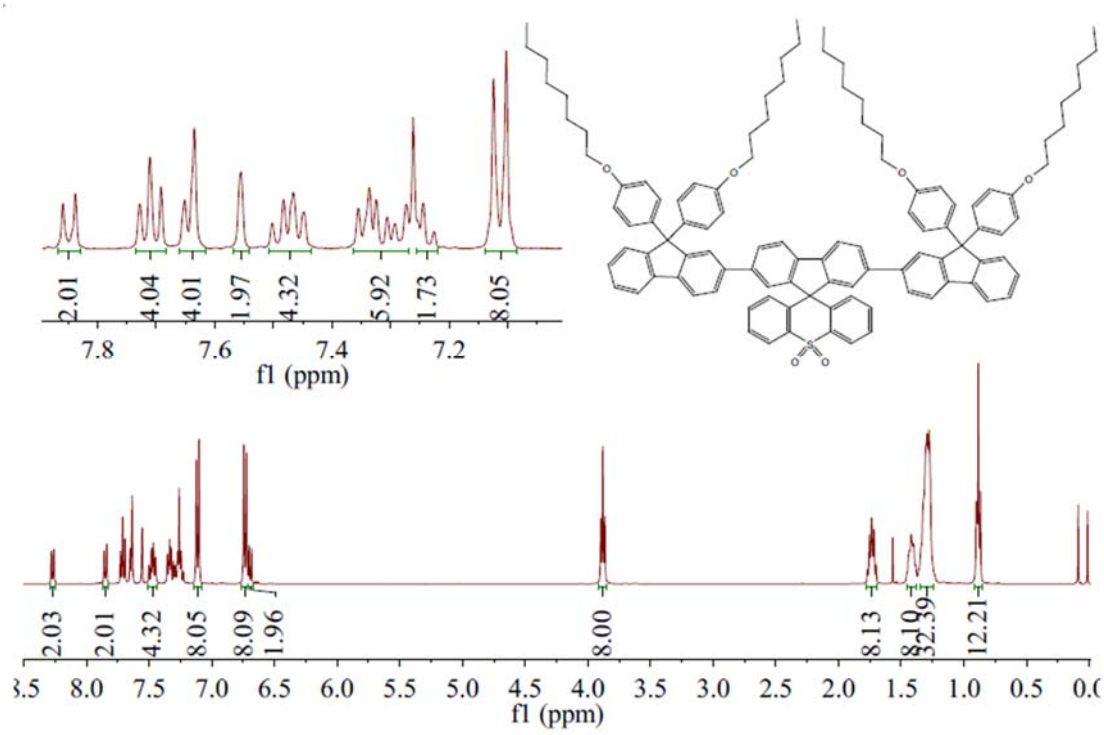

Figure S42. ^{1}H NMR spectrum of DOPhF-SFXSO. Related to Figure 1.

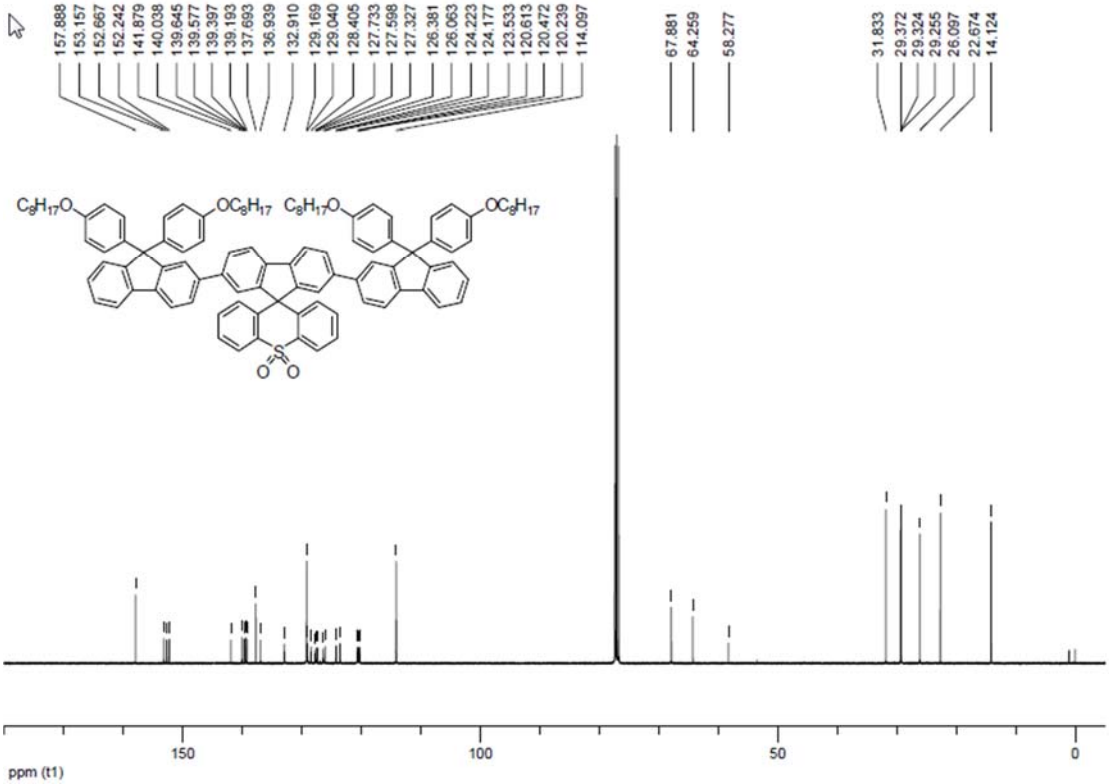

Figure S43. ^{13}C NMR spectrum of DOPhF-SFXSO. Related to Figure 1.

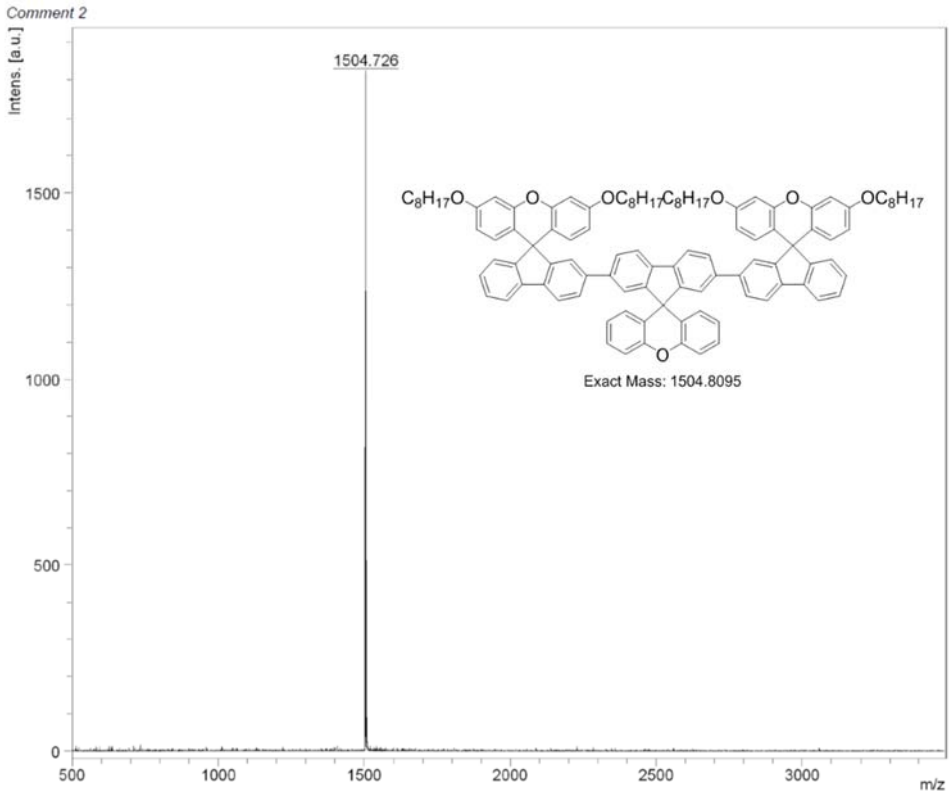

Figure S44. MALDI-TOF mass spectrum of DOSFX-SFX. Related to Figure 1.

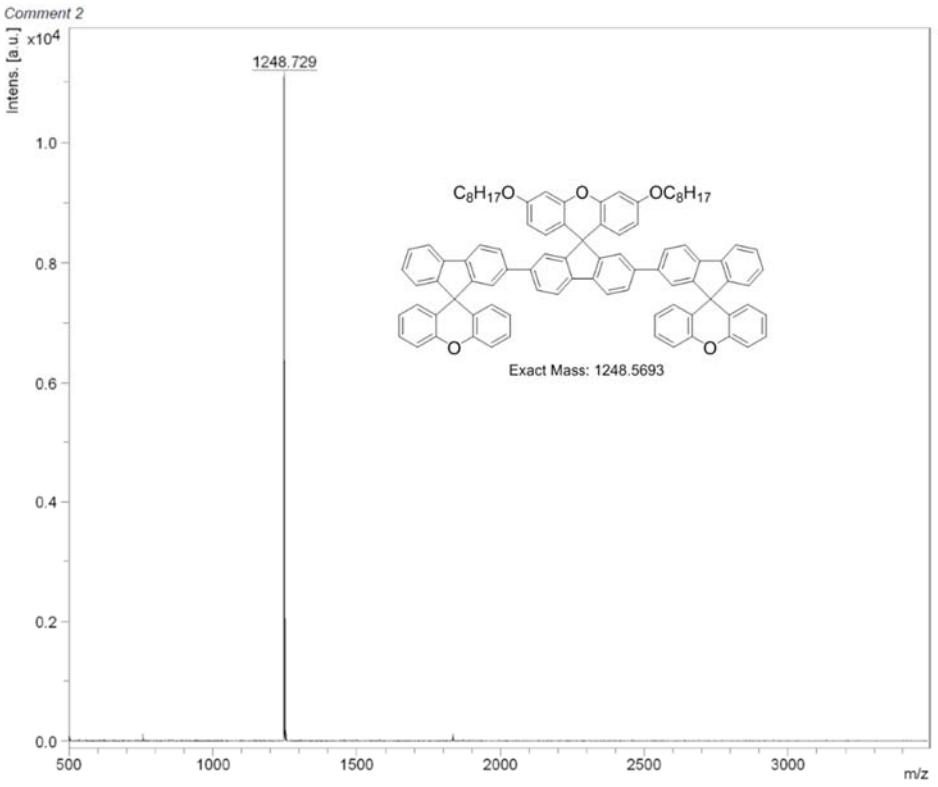

Figure S45. MALDI-TOF mass spectrum of DSFX-OSFX. Related to Figure 1.

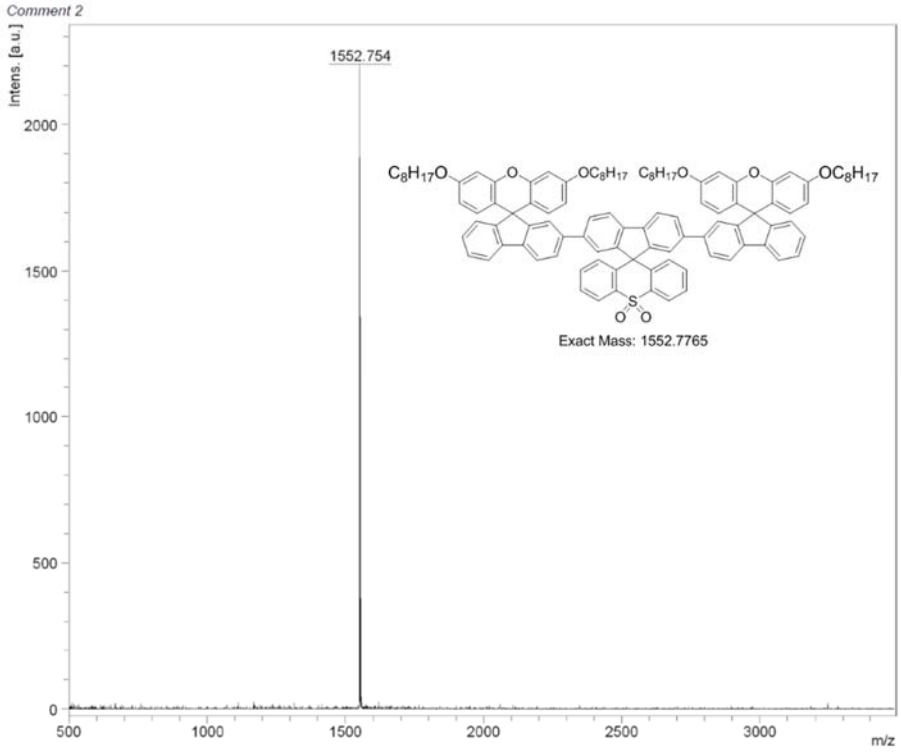

Figure S46. MALDI-TOF mass spectrum of DOSFX-SFXSO. Related to Figure 1.

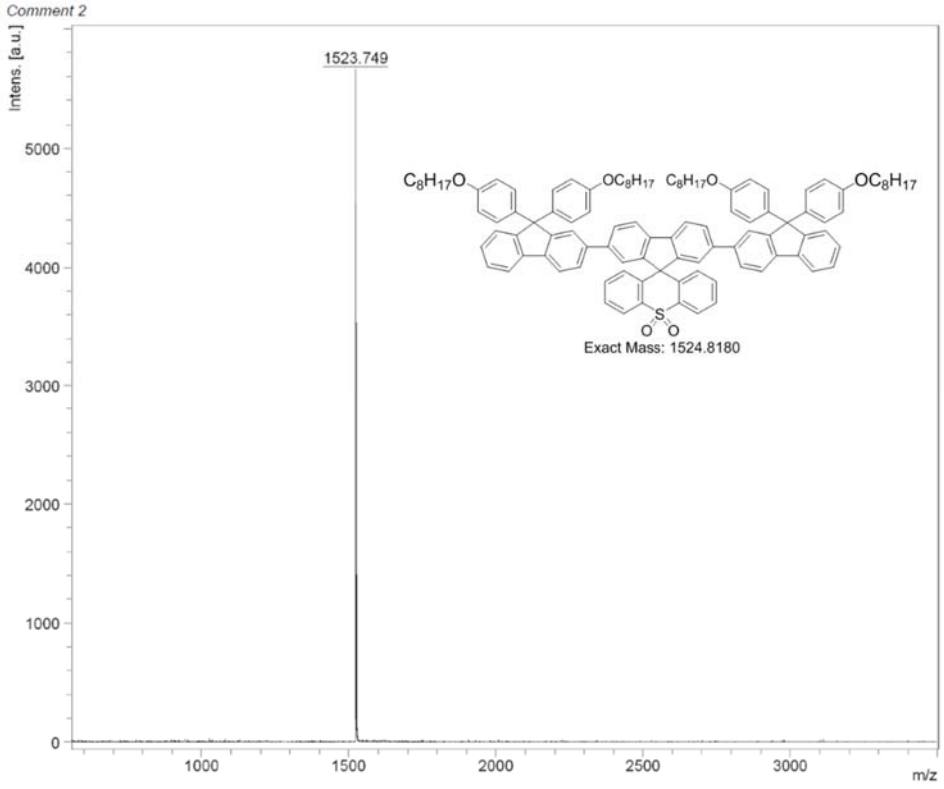

Figure S47. MALDI-TOF mass spectrum of DOPhF-SFXSO. Related to Figure 1.

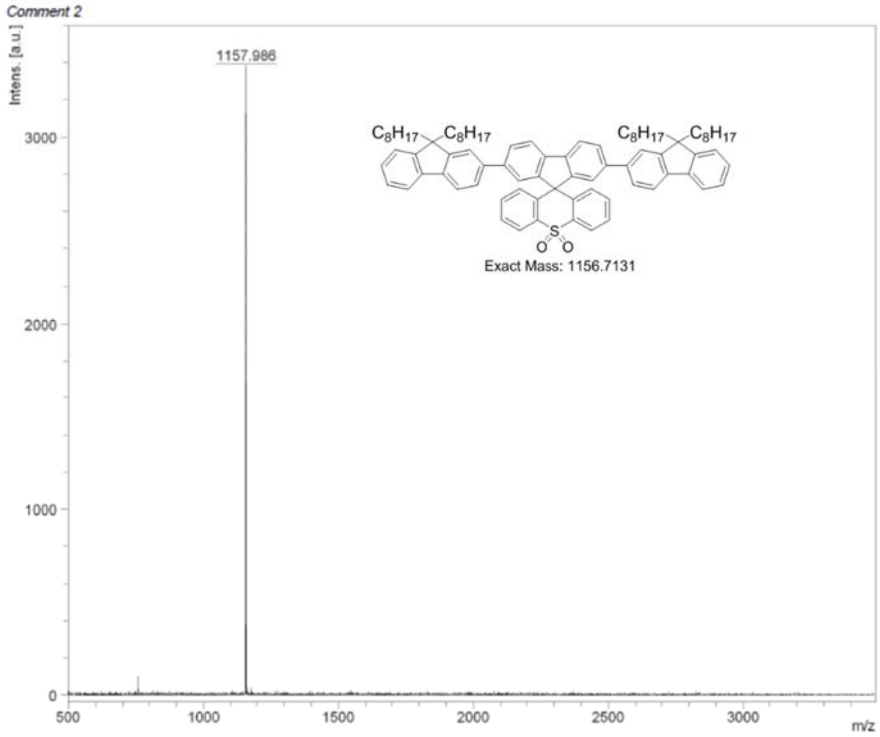

Figure S48. MALDI-TOF mass spectrum of DOF-SFXSO. Related to Figure 1.

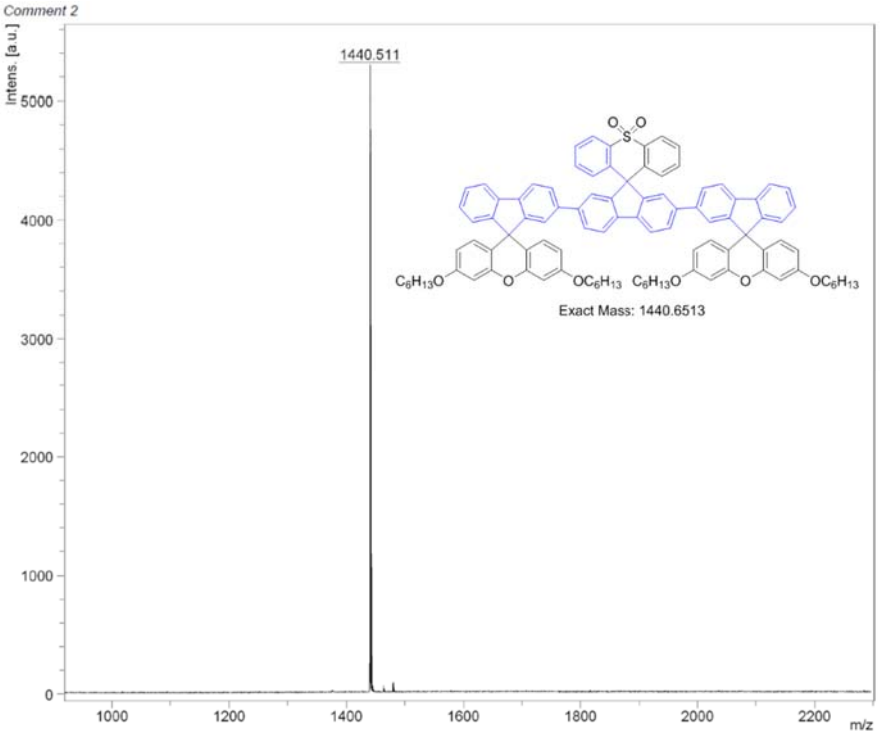

Figure S49. MALDI-TOF mass spectrum of DHSFX-SFXSO. Related to Figure 1.

Table S1. Electrochemical properties of terfluorenes. Related to Figure 1.

Entry	$E_{red,on}$[a] V	$E_{ox,on}$[b] V	LUMO[c] eV	HOMO[d] eV	E_{gap}[e] eV
DOSFX-SFXSO	-2.08	0.93	-2.66	-5.67	3.01
DOSFX-SFX	-2.20	0.89	-2.54	-5.63	3.09
DOF-SFXSO	-2.10	0.86	-2.64	-5.60	2.96
DOPhF-SFXSO	-2.13	0.88	-2.61	-5.62	3.01
DSFX-OSFX	-2.16	0.90	-2.58	-5.64	3.06
DHSFX-SFXSO	-2.05	0.98	-2.69	-5.72	3.03

[a]On-set reduction potential. [b]On-set oxidation potential. [c]LUMO = -($E_{red,on}$-E_{φ})-4.80 eV, where E_{φ} is potential of ferrocene. [d]HOMO = -($E_{ox,on}$-E_{φ})-4.80 eV. [e]E_{gap} = LUMO – HOMO.

Table S2. Crystal data of bulk terfluorenes. Related to Figure ~~1~~2.

name	DOSFX-SFX	DOF-SFXSO	DOSFX-SFXSO	DHSFX-SFXSO
CCDC No.	1448974	1860090	1887107	1887099
formula	$C_{107}H_{108}O_7$	$C_{83}H_{96}O_2S$	$C_{111}H_{112}C_{112}O_8S$	$C_{99}H_{92}O_8S$
fw[g/mol]	1505.93	1157.65	2031.46	1441.78
crystal color	colorless	colorless	colorless	colorless
size [mm]	0.23*0.20*0.15	0.31*0.12*0.07	0.30*0.15*0.05	0.14*0.11*0.06
T [K]	100	173	173	173
lattice type	monoclinic	triclinic	monoclinic	monoclinic
space group	$P2_1/c$	P-1	$C2/c$	$P2/n$
a [Å]	18.8804(15)	12.5322 (9)	55.433 (3)	24.7839 (15)
b [Å]	10.6661(9)	13.8332 (11)	10.9061 (5)	10.9378 (6)
c [Å]	42.297(3)	20.1569 (16)	16.7183 (8)	32.4523 (18)
α [°]	90	96.504 (5)	90	90
β [°]	105.485(3)	102.145 (4)	94.057 (4)	110.920 (3)
γ [°]	90	92.417 (4)	90	90
V [$Å^3$]	8208.59 (11)	3386.4 (5)	10081.8 (38)	8217.3 (8)
Z	4	2	4	4
F(000)	3224	1252	4248	3064
absorption coefficient [mm^{-1}]	0.074	0.774	3.663	0.755
measured	14456	9032	7083	9919
observed	11340	11545	8289	14355
θ range [°]	1.0-25.0	3.22-65.17	3.20-63.87	2.92-66.38
R1	0.0588	0.1033	0.1689	0.0868
ωR2	0.1364	0.2851	0.4260	0.2502
completeness	0.999	0.987	0.991	0.986
S	1.049	1.039	1.049	1.024

Supplemental References

C. J. Ou, C. Zhu, X. H. Ding, L. Yang, J. Y. Lin, L. Xie, Y. Qian, C. Xu, J. F. Zhao and W. Huang, (2017). Dimerization effect of fluorene-based semiconductors on conformational planarization for microcrystal lasing. J. Mater. Chem. C, 5, 5345-5355.

C. J. Ou, X. H. Ding, Y. X. Li, C. Zhu, M. N. Yu, L. Xie, J. Y. Lin, C. Xu and W. Huang, (2017). Conformational effect of polymorphic terfluorene on photophysics, crystal morphologies, and lasing behaviors. J. Phys. Chem. C, 121, 14803-14810.

Z. Zuo, C. Ou, Y. Ding, H. Zhang, S. Sun, L. Xie, R. Xia and W. Huang, (2018). Spiro-substitution effect of terfluorenes on amplified spontaneous emission and lasing behaviors. J. Mater. Chem. C, 2018, 6, 4501-4507.